

UNIVERSITY OF CALIFORNIA
SANTA CRUZ

**KERNEL REGRESSION FOR IMAGE PROCESSING AND
RECONSTRUCTION**

A thesis submitted in partial satisfaction of the
requirements for the degree of

MASTER OF SCIENCE

in

ELECTRICAL ENGINEERING

by

Hiroyuki Takeda

March 2006

The Thesis of Hiroyuki Takeda
is approved:

Professor Peyman Milanfar, Chair

Professor Ali Shakouri

Professor Michael Elad

Sina Farsiu, Ph.D.

Lisa C. Sloan
Vice Provost and Dean of Graduate Studies

Copyright © by

Hiroyuki Takeda

2006

Contents

List of Figures	v
List of Tables	viii
Abstract	ix
Dedication	x
Acknowledgments	xi
1 Introduction	1
1.1 Introduction to Image Processing and Reconstruction	1
1.2 Super Resolution	2
1.2.1 Motion Estimation	3
1.2.2 Frame Fusion	4
1.2.3 Deblurring	5
1.3 Previous Work	5
1.4 Summary	9
2 Kernel Regression	11
2.1 Introduction	11
2.2 Kernel Regression for Univariate Data	11
2.2.1 Related Regression Methods	17
2.3 Kernel Regression for Bivariate Data and its Properties	20
2.3.1 Kernel Regression Formulation	20
2.3.2 Equivalent Kernel	23
2.3.3 The Selection of Smoothing Matrices	26
2.4 Super-Resolution by Kernel Regression	29
2.5 Summary	31
3 Data-Adapted Kernel Regression	33
3.1 Introduction	33
3.2 Data-Adapted Kernel Regression	34
3.2.1 Bilateral Kernel Regression	35
3.2.2 Steering Kernel Regression	37

3.3	Iterative Steering Kernel Regression	45
3.3.1	Filtering Algorithm	45
3.3.2	Performance Analysis	46
3.4	Summary	47
4	Motion Estimation	53
4.1	Introduction	53
4.2	Accurate Motion Estimation	54
4.2.1	Motion Estimator Based on Optical Flow Equations	54
4.2.2	Multiscale Motion Estimation	57
4.3	Image Warping	59
4.4	Simulations	60
4.5	Summary	61
5	Demonstration and Conclusion	62
5.1	Introduction	62
5.2	Image Denoising	62
5.3	Image Interpolation	64
5.4	Super-Resolution	65
5.5	Conclusion	66
6	Super Resolution Toolbox	78
6.1	Introduction	78
6.2	Installation	78
6.3	The Kernel Regression Function	79
6.4	Examples	80
6.5	Troubleshooting	81
6.6	Summary	82
7	Future Work	83
7.1	Robust Kernel Regression	83
7.2	Segment Motion Estimation	86
7.2.1	Motivation	86
7.2.2	Image Segmentation	86
7.2.3	Motion Models	87
7.3	Example	88
7.4	Summary	88
A	Image Deblurring	92
B	Local Gradient Estimation	94
	Bibliography	96

List of Figures

1.1	(a) Interpolation of regularly sampled data. (b) Reconstruction from irregularly sampled data. (c) Denoising.	2
1.2	Image fusion yields us irregularly sampled data.	3
1.3	A general model for multi-frame super-resolution.	6
1.4	Tank sequence.	8
1.5	An example of the estimated image from Tank sequence.	9
2.1	Examples of local polynomial regression of an equally-spaced data set. The signals in the first and second rows are contaminated with the Gaussian noise of $\text{var}(\varepsilon_i) = 0.1$ and 0.5 , respectively. The dashed, solid lines, and dots represent the actual function, estimated function, and the noisy data, respectively. The columns from left to right show the constant, linear, and quadratic interpolation results. Corresponding RMSE's for the first row experiments are 0.0025 , 0.0025 , 0.0009 and for the second row are as 0.0172 , 0.0172 , 0.0201	18
2.2	A comparison of the position of knots in (a) Kernel regression and (b) classical B-Spline methods.	19
2.3	(a) A uniformly sampled data set. (b) A horizontal slice of the equivalent kernels of orders $N = 0, 1$, and 2 for the regularly sampled data in (a). The kernel $K_{\mathbf{H}}$ in (2.22) is modeled as a Gaussian, with the smoothing matrix $\mathbf{H} = \text{Diag}[10, 10]$	25
2.4	Equivalent kernels for an irregularly sampled data set are shown in (a). (b) is the second order ($N = 2$) equivalent kernel. The horizontal and vertical slices of the equivalent kernels of different orders ($N = 0, 1, 2$) are compared in (c) and (d), respectively. In this example, the kernel $K_{\mathbf{H}}$ in (2.22) was modeled as a Gaussian, with the smoothing matrix $\mathbf{H} = \text{Diag}[10, 10]$	27
2.5	Smoothing (kernel size) selection by sample density.	28
2.6	The block diagram of the super-resolution algorithm using kernel regression.	30
2.7	A super-resolution example on the tank sequence.	32
3.1	Kernel spread in a uniformly sampled data set. (a) Kernels in the classic method depend only on the sample density. (b) Data-adapted kernels elongate with respect to the edge.	34
3.2	Schematic representation of an example of clustering.	39
3.3	Schematic representation of typical linkage methods.	41

3.4	Schematic representation illustrating the effects of the steering matrix and its component ($\mathbf{C}_i = \gamma_i \mathbf{U}_{\theta_i} \mathbf{\Lambda}_{\sigma_i} \mathbf{U}_{\theta_i}^T$) on the size and shape of the regression kernel	42
3.5	Footprint examples of steering kernels with covariance matrices $\{\mathbf{C}_i\}$ given by the local orientation estimate (3.23) at a variety of image structures.	44
3.6	Block diagram representation of the iterative adaptive regression.	46
3.7	A denoising experiment by iterative steering kernel regression.	49
3.8	The analysis of mean square error, bias, and variance.	50
3.9	The best estimation in mean square error with two different global smoothing parameters.	50
3.10	Mean square error with different global smoothing parameters.	51
3.11	Bias with different global smoothing parameters.	51
3.12	Variance with different global smoothing parameters.	52
4.1	The forward and backward motion.	56
4.2	Multiscale motion estimation	58
4.3	The block diagram of accurate motion estimation on a scale.	59
4.4	A simulated sequence.	60
4.5	The performance analysis of motion estimations with different warping methods.	61
5.1	The performance of different denoising methods are compared in this experiment. The RMSE of the images (b)-(f) are 25, 8.91, 8.65, 6.64, and 6.66, respectively.	68
5.2	Figures 5.1(c)-(f) are enlarged to give (a),(b),(c), and (d), respectively.	69
5.3	The performance of different denoising methods are compared in this experiment on a compressed image by JPEG format with the quality of 10. The RMSE of the images (b)-(f) are 9.76, 9.05, 8.52, 8.80, and 8.48, respectively.	70
5.4	The performance of different denoising methods are compared in this experiment on a color image with real noise. Gaussian kernel was used for all experiments.	71
5.5	Upscaling experiment. The image of Lena is downsampled by the factor of 3 in (a). The factor of 3 up-sampled images of different methods are shown in (b)-(f). The RMSE values for images (b)-(f) are 7.92, 7.96, 8.07, 7.93, and 7.43 respectively.	72
5.6	Figures 5.5(a)-(f) are enlarged to give (a)-(f), respectively.	73
5.7	Irregularly sampled data interpolation experiment, where 85% of the pixels in the Lena image are omitted in (a). The interpolated images using different methods are shown in (b)-(f). RMSE values for (b)-(f) are 9.15, 9.69, 9.72, 8.91, and 8.21, respectively.	74
5.8	Figures 5.7(a)-(f) are enlarged to give (a)-(f), respectively.	75
5.9	Image fusion (Super-Resolution) experiment of a real data set consisting of 10 compressed grayscale images. One input image is shown in (a) which is up-scaled in (b) by the spline smoother interpolation. (c)-(d) show the multi-frame Shift-And-Add images after interpolation by the Delaunay-spline smoother and the steering kernel methods. The resolution enhancement factor in this experiment was 5 in each direction.	76

5.10	Image fusion (Super-Resolution) experiment of a real data set consisting of 10 compressed color frames. One input image is shown in (a). (b)-(d) show the multi-frame Shift-And-Add images after interpolating by the Delaunay-spline smoother, classical kernel, and steering kernel regression methods, respectively. The resolution enhancement factor in this experiment was 5 in each direction.	77
6.1	Setting path.	79
7.1	An example of the salt & pepper noise reduction. Corresponding RMSE for (b)-(h) are 63.84, 11.05, 22.47, 21.81, 21.06, 7.65, and 7.14.	84
7.2	Three large frames from a video sequence. The size of each frame is 350×600	89
7.3	The reconstructed image using the translational motion model.	90
7.4	The reconstructed image using the translational motion model with the block segmentation.	91

List of Tables

2.1	Popular choices for the kernel function.	15
3.1	The best estimation in mean square error by iterative steering kernel regression with different global smoothing parameters.	48
6.1	The parameter descriptions of “KernelReg” function.	80
7.1	Error norm functions and their derivatives [1].	85
A.1	Regularization functions and their first derivatives.	93

Abstract

Kernel Regression for Image Processing and Reconstruction

by

Hiroyuki Takeda

This thesis reintroduces and expands the *kernel regression* framework as an effective tool in image processing, and establishes its relation with popular existing denoising and interpolation techniques. The filters derived from the framework are locally adapted kernels which take into account both the local density of the available samples and the actual values of these samples. As such, they are automatically steered and adapted to both the given sampling *geometry* and the samples' *radiometry*. Furthermore, the framework does not rely upon any specific assumptions about signal and noise models; it is applicable to a wide class of problems: efficient image upscaling, high quality reconstruction of an image from as little as 15% of its (irregularly sampled) pixels, super-resolution from noisy and under-determined data sets, state of the art denoising of image corrupted by Gaussian and other noise, effective removal of compression artifacts, and more. Thus, the adapted kernel method is ideally suited for image processing and reconstruction. Experimental results on both simulated and real data sets are supplied, and demonstrating the presented algorithm and its strength.

Dedicated to my parents, Ren Jie Dong and Akemi Takeda,
my sisters, Tomoko Takeda and Asako Takeda,
and my grandmother, Kinu Takeda.

Acknowledgments

This work is the result of my spirit of challenge, supported and encouraged by many wonderful people. I would like to express my deep gratitude to all of them here.

First of all, I would like to thank my advisor, Professor Peyman Milanfar. Without his incredible guidance and support, I would have never done this work. His classes (Digital Signal Processing, Statistical Signal Processing, and Image Processing and Reconstruction) were also significant to helping me finish this thesis. I appreciate not only the excellent materials in his class and his straightforward explanations, but also his teaching me how to analyze problems and organize publications. His advice always cheered me up.

Dr. Sina Farsiu frequently suffered through correcting the draft versions of my poorly organized publications. His modifications of my drafts and his advice were greatly helpful in teaching me to organize content. I want to thank him for his incredible help.

The text of this thesis includes reprints of the following previously published material: *Image Denoising by Adaptive Kernel Regression* [2], *Kernel Regression for Image Processing and Reconstruction* [3], and *Robust Kernel Regression for Restoration and Reconstruction of Images from Sparse Noisy Data* [4]. The co-authors listed in these publications, Professor Peyman Milanfar and Dr. Sina Farsiu, directed and supervised the research which forms the basis for the thesis. Hence, I would like to thank both of them one more time here. The publications contain not only my ideas but also a lot of their ideas, suggestions, and advices.

I want to thank the thesis reading committee (Professor Peyman Milanfar, Professor Ali Shakouri, Professor Michael Elad, and Dr. Sina Farsiu) for reviewing this thesis and their valuable feedback.

I would also like to express my gratitude to one of my best friends, Shigeru Suzuki.

He is the first person I met in Santa Cruz. Since then, his unique advice has helped me to survive in graduate school. I am lucky to be his friend, and will never forget his support.

A lot of thanks to other supportive people: Professor John Vesecky (my first academic advisor at UC Santa Cruz), Dr. Morteza Shahram , Dr. Dirk Robinson, and the members in the Multi-Dimensional Signal Processing research group (Amy Poonawala, Davy Odom, and Mike Charest), and all of my other friends.

Finally, I want to express gratitude to my family, Ren Jie Dong, Akemi Takeda, Asako Takeda, Tomoko Takeda, and Kinu Takeda. I cannot find any other words for their sacrifice and consideration. I thank my family so much. This work is dedicated to my family.

Santa Cruz, California

March 21st, 2006

Hiroyuki Takeda

Chapter 1

Introduction

1.1 Introduction to Image Processing and Reconstruction

Ease of use and cost effectiveness have contributed to the growing popularity of digital imaging systems. However, inferior spatial resolution with respect to traditional film cameras is still a drawback. The apparent aliasing effects often seen in digital images are due to the limited number of CCD pixels used in commercial digital cameras. Using denser CCD arrays (with smaller pixels) not only increases the production cost but can also result in noisier images. As a cost efficient alternate, image processing methods have been exploited through the years to improve the quality of digital images. In this work, we focus on regression methods that attempt to recover the noiseless high-frequency information corrupted by the limitations of the imaging system, as well as degradation processes such as compression.

This thesis concentrates on the study of regression, as a tool not only for interpola-

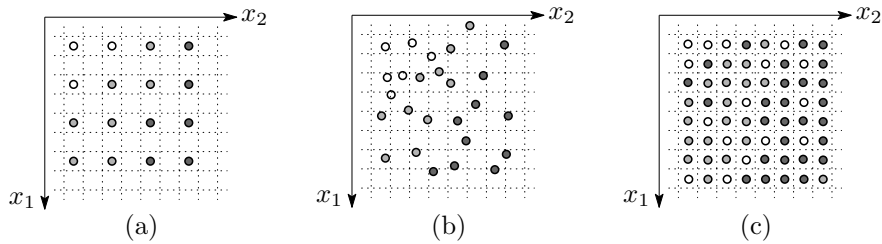


Figure 1.1: (a) Interpolation of regularly sampled data. (b) Reconstruction from irregularly sampled data. (c) Denoising.

tion of regularly sampled frames (up-sampling) but also for reconstruction and enhancement of noisy and possibly irregularly sampled images. Figure 1.1(a) illustrates an example of the former case, where we opt to upsample an image by a factor of two in each direction. Figure 1.1(b) illustrates an example of the latter case, where an irregularly sampled noisy image is to be interpolated onto a high resolution grid. Besides inpainting applications [5], interpolation of irregularly sampled image data is essential for applications such as multi-frame super-resolution, where several low-resolution images are fused (interlaced) onto a high-resolution grid [6]. Figure 1.2 presents a schematic representation of such *super-resolution* algorithms. We note that “denoising” is a special case of the regression problem where samples at all desired pixel locations are given (illustrated in Figure 1.1(c)), but these samples are corrupted and are to be restored. The following section gives us a brief review of the general idea of super-resolution.

1.2 Super Resolution

The super-resolution technique reconstructs a high quality (less noise and higher resolution) image from a noisy and low resolution video sequence. The key to super-resolution is that the frames of a video sequence have aliasing; in other words, they are

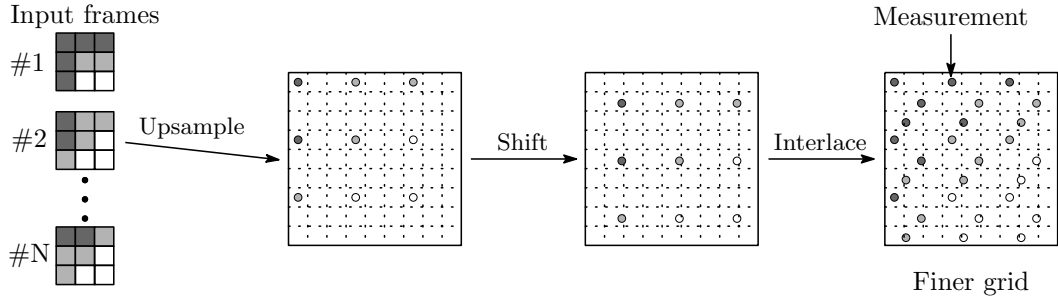


Figure 1.2: Image fusion yields us irregularly sampled data.

sampled at under the Nyquist rate, so that the details of a real scene are disrupted in each frame. Without aliasing, super-resolution becomes merely a denoising, upscaling, and deblurring process. There are mainly two approaches to reconstruct such a high quality image in the image processing community. One class of methods are those that operate in some transformed domain (e.g. the frequency domain and wavelet domain). The other approach processes the video frames/samples in the spatial domain directly. In this thesis we focus on the approach in the spatial domain, since it is more convenient to understand intuitively the relationships among neighboring data (measured pixels). The super-resolution technique in the spatial domain usually builds up with the three principle phases: *motion estimation*, *image (frame) fusion*, and *deblurring*.

1.2.1 Motion Estimation

As a first step, we have to know motion (relative spatial distance between every pair of frames) to within subpixel accuracy. Several motion models (such as translational, affine, and so on) have been considered and, in this thesis, we try to estimate motion based on *optical flow equations*¹. Black *et al.* [1] have proposed to estimate motion containing

¹A good review about the optical flow is in [7], and details can be found in [8].

occlusions with the *robust estimation* method with which they tried to eliminate outliers. Estimating motion to subpixel accuracy is extremely difficult; hence, Chapter 4 sums up our approach for such accurate motion estimation. Although the performance of the optical flow estimator is poor when the motion is large, the multiscale version of the algorithm uses the estimator many times properly and will give us a much more accurate estimate.

1.2.2 Frame Fusion

Once the motion between the set of frames is available, we upsample all the frames and register them to a finer grid, as illustrated in Figure 1.2. This process is often called *Shift-and-Add* method [9]. Since the estimated motion are usually fractional numbers, with the exception of the measurements from the reference frame, most pixels will not be located on the lattice points of the finer grid. The next step we have to take is to estimate all the high resolution pixel values from the nearby measurements, which is so-called *interpolation*. There are a variety of interpolation methods in the image processing literature. *Nearest neighbor*, *bilinear*, and *cubic spline interpolation* [10, 11, 12] are typical. However, they are not designed for irregularly sampled data sets. Furthermore, the measurements are noisy not only in their values, but also positions. The principal purpose of this thesis is to propose suitable interpolation techniques for such irregularly sampled data.

A famous interpolation technique is the *Nadaraya-Watson Estimator* (NWE) [13]. NWE estimates an appropriate pixel value by taking an adaptive weighted average of several nearby samples, and consequently its performance is totally dependent on the choice of weights. In Chapter 3, we propose a novel method of computing the weights taking into account not only the local density of the available samples but also the actual values of samples. As such, the weights are automatically steered and adapted to both the given

sampling *geometry*, and the samples' *radiometry*. Furthermore, due to the minimal assumptions made on given data sets, the method will be applicable to a wide class of problems: efficient image upscaling, high quality reconstruction of an image from as little as 15% of its (irregularly sampled) pixels, super-resolution from noisy and under-determined data sets, state of the art denoising of an image corrupted by Gaussian and other noise, effective removal of compression artifacts, demosaicing, and more.

1.2.3 Deblurring

The reconstructed images are often blurry due to the blurring effects of atmosphere and camera aperture. The purpose of this phase is to revive some high frequency components, which visually sharpens the images. One typical choice here is the *Wiener filter* [10]. This thesis will not be concerned with this phase in much depth. A simple deblurring method is described in Appendix A.

1.3 Previous Work

A super-resolution model, which can be found in [6, 9, 14, 15], is illustrated in Figure 1.3. In the figure, X is a continuous real scene to be estimated, B^{atm} and B^{cam} are the continuous point spread functions caused by atmospheric turbulence and camera aperture, respectively, F is the warp operator, D is the downsampling (or discretizing) effect, ε is measurement noise, and Y is a noisy, blurry, low resolution image (frame). Based on the model, we can mathematically express the frame at the position $[l, m]$ and the time n :

$$Y_n[l, m] = \left[B_n^{\text{cam}}(x_1, x_2) * * F_n \left\{ B_n^{\text{atm}}(x_1, x_2) * * X(x_1, x_2) \right\} \right] \Bigg|_{\downarrow} + \varepsilon_n[l, m], \quad (1.1)$$

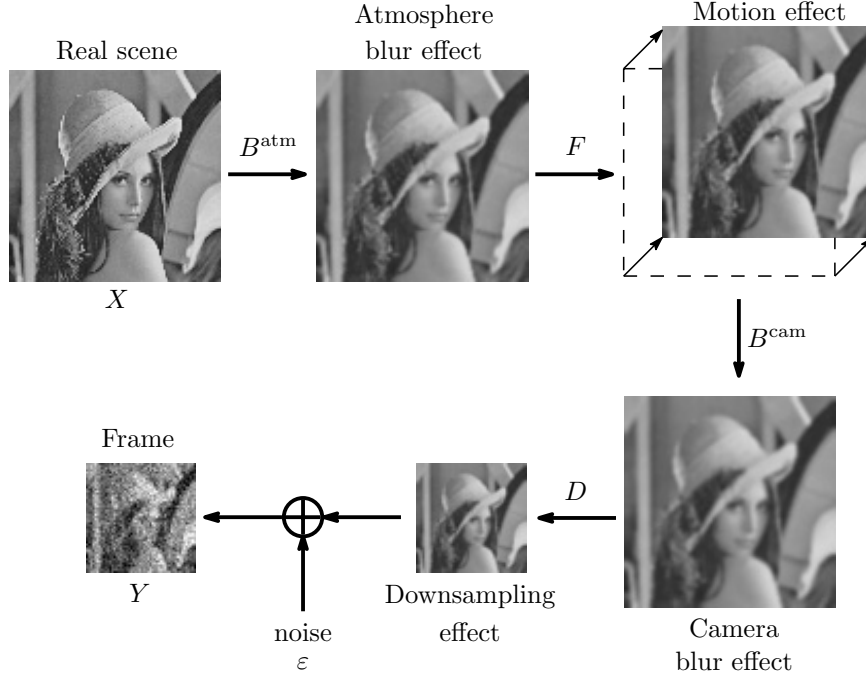


Figure 1.3: A general model for multi-frame super-resolution.

where $**$ is the two dimensional convolution operator and \downarrow is the discretizing operator. Now we want to estimate a high resolution (discrete) unknown image \mathbf{X} from all the measured data \mathbf{Y}_n 's, where we define \mathbf{Y}_n and \mathbf{X} as

$$\mathbf{Y}_n = \begin{bmatrix} Y_n[1,1] & Y_n[1,2] & \cdots & Y_n[1,M] \\ Y_n[2,1] & Y_n[2,2] & \cdots & Y_n[2,M] \\ \vdots & \vdots & \ddots & \vdots \\ Y_n[L,1] & Y_n[L,2] & \cdots & Y_n[L,M] \end{bmatrix}, \quad (1.2)$$

$$\mathbf{X} = \begin{bmatrix} X(1,1) & X(1,2) & \cdots & X(1,rM) \\ X(2,1) & X(2,2) & \cdots & X(2,rM) \\ \vdots & \vdots & \ddots & \vdots \\ X(rL,1) & X(rL,2) & \cdots & X(rL,rM) \end{bmatrix}. \quad (1.3)$$

We call r the resolution enhancement factor. Using the notations, we can rewrite the model (1.1) into the matrix form:

$$\underline{\mathbf{Y}}_n = \mathbf{D}\mathbf{B}_n^{\text{cam}}\mathbf{F}_n\mathbf{B}_n^{\text{atm}}\underline{\mathbf{X}} + \underline{\boldsymbol{\varepsilon}}_n, \quad n = 1, \dots, N, \quad (1.4)$$

where the underline is the operator which makes a matrix a column stack vector, $\underline{\mathbf{X}}$ is a $r^2LM \times 1$ vector, $\mathbf{B}_n^{\text{atm}}$, $\mathbf{B}_n^{\text{cam}}$ and \mathbf{F}_n are $r^2LM \times r^2LM$ matrices, \mathbf{D} is a $LM \times r^2LM$ matrix, and $\underline{\mathbf{Y}}_n$ and $\underline{\boldsymbol{\varepsilon}}_n$ are $LM \times 1$ vectors. The model (1.4) can be simplified as follows. With the two assumptions [6]: (1)spatially and temporally shift invariant point spread functions, (2)translational motion, both $\mathbf{B}_n^{\text{cam}}$ and $\mathbf{B}_n^{\text{atm}}$ become symmetric constant matrices, and \mathbf{F}_n becomes a symmetric matrix. Since the symmetric matrices are commutable, we can rewrite (1.4) as

$$\underline{\mathbf{Y}}_n = \mathbf{D}\mathbf{B}^{\text{cam}}\mathbf{F}_n\mathbf{B}^{\text{atm}}\underline{\mathbf{X}} + \underline{\boldsymbol{\varepsilon}}_n, \quad (1.5)$$

$$= \mathbf{D}\mathbf{B}^{\text{cam}}\mathbf{B}^{\text{atm}}\mathbf{F}_n\underline{\mathbf{X}} + \underline{\boldsymbol{\varepsilon}}_n. \quad (1.6)$$

Moreover, by defining $\mathbf{B} = \mathbf{B}^{\text{cam}}\mathbf{B}^{\text{atm}}$, we finally have a convenient model:

$$\underline{\mathbf{Y}}_n = \mathbf{D}\mathbf{B}\mathbf{F}_n\underline{\mathbf{X}} + \underline{\boldsymbol{\varepsilon}}_n, \quad n = 1, \dots, N. \quad (1.7)$$

This is a prevalent model of super-resolution. Based on the model, an appropriate way to estimate $\underline{\mathbf{X}}$ is *regularized least squares estimator* [16], which takes the form of

$$\hat{\underline{\mathbf{X}}}_{\text{RLS}} = \arg \min_{\underline{\mathbf{X}}} \left[\sum_{n=1}^N \left\| \mathbf{D}\mathbf{B}\mathbf{F}_n\underline{\mathbf{X}} - \underline{\mathbf{Y}}_n \right\|_2^2 + \lambda \Upsilon(\underline{\mathbf{X}}) \right], \quad \lambda \geq 0, \quad (1.8)$$

where $\Upsilon(\cdot)$ is the regularization function (see Table **A.1** in Appendix A), and λ is a regularization parameter (a positive number) which enables us to control how strongly we consider the regularization term. Using the estimator, an example is demonstrated in the following. Figure **1.4** shows Tank sequence (64×64 , 8 frames) which is a real sequence taken by an

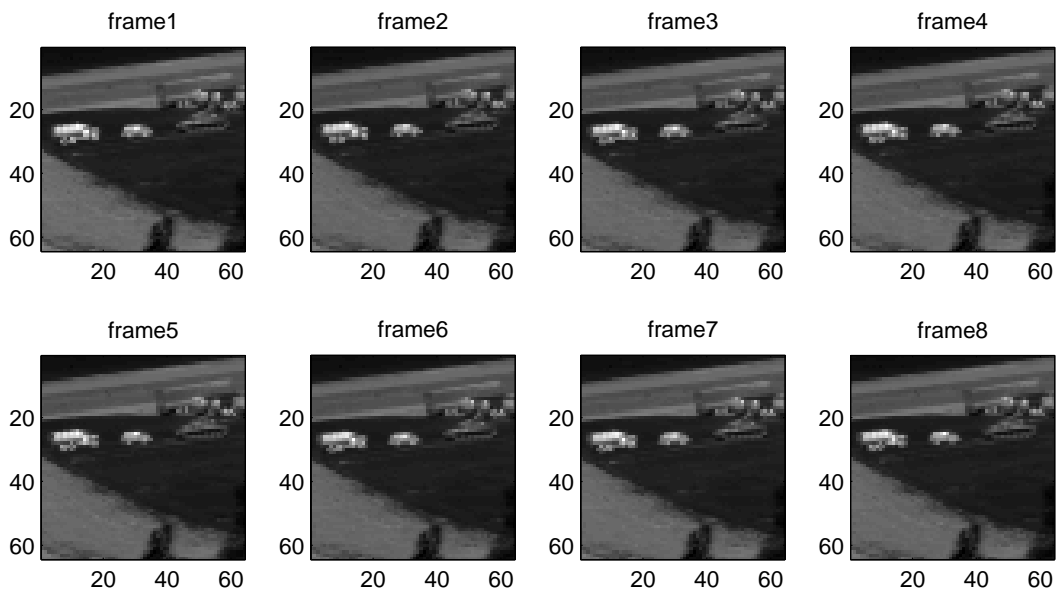


Figure 1.4: Tank sequence.

infrared camera, courtesy of B. Yasuda and the FLIR research group in the Sensors Technology Branch, Wright Laboratory, WPAFB, OH. A reconstructed high resolution image² is shown in Figure 1.5. We can see the more details with the estimated image such as the wheels of the truck which are impossible for us to realize in each low resolution frame.

This section showed that a prevalent super-resolution method. In Chapter 2, we will present a different super-resolution approach, and show an example on Tank sequence. In Chapter 5, we will demonstrate further real super-resolution examples with the different super-resolution approach by combining motion estimation in Chapter 4, image fusion in Chapter 2 and its extension in Chapter 3, and image deblurring in Appendix A.

²This image provided by a software coded by S. Farsiu [6], which is available online at www.cse.ucsc.edu/~milanfar/SR-Software.htm



Figure 1.5: An example of the estimated image from Tank sequence.

1.4 Summary

We briefly reviewed image reconstruction from irregularly sampled data sets with existing algorithms in this introductory chapter. However, most of these algorithms are designed for a specific model, and consequently they cannot be applicable for other problems. If only one method can do denoising and interpolation simultaneously with a superior performance, we will be relieved from choosing the best algorithm for a specific problem. The main purpose of this thesis is to present such a *universal* algorithm.

Contributions of this thesis are the following: (1) we describe and propose *kernel*

regression as an effective tool for both denoising and interpolating images, and establish its relation with some popular existing techniques, (2) we propose a novel adaptive generalization of kernel regression with superior results in both denoising and interpolation (for single or multi-frame) applications. This thesis is structured as follows. In Chapter 2, the kernel regression framework will be described as an effective tool for image processing with its fundamental property, the relationships with some other famous methods, and a simple example on Tank sequence. In Chapter 3, the data-adapted (non-linear) version of kernel regression will be presented. In Chapter 4, we sum up the accurate motion estimation algorithm in order to fuse images. In Chapter 5, many demonstrations on a wide class of problems will be shown, and conclude this thesis. In Chapter 6, the installation and manuals of the program codes, which produce the results shown in Chapter 5, will be explained. Finally, in Chapter 7, we indicate some of our future directions on this research.

Chapter 2

Kernel Regression

2.1 Introduction

In this chapter, we make contact with the field of non-parametric statistics and present a development and generalization of tools and results for use in image processing and reconstruction. Furthermore, we establish key relationships with some popular existing methods and show how several of these algorithms are special cases of the framework.

2.2 Kernel Regression for Univariate Data

Classical parametric denoising methods rely on a specific model of the signal of interest, and seek to compute the parameters of this model in the presence of noise. Examples of this approach are represented in diverse problems ranging from denoising to upscaling and interpolation. A generative model based upon the estimated parameters is then produced as the best estimate of the underlying signal. Some representative examples of the

parametrization are quadratic, periodic, and monotone models [17],

$$y_i = \beta_0 + \beta_1 x_i + \beta_2 x_i^2 + \varepsilon_i, \quad y_i = \beta_0 \sin(\beta_1 x_i) + \varepsilon_i, \quad y_i = \frac{\beta_0}{\beta_1 + x_i} + \varepsilon_i, \quad i = 1, 2, \dots, P, \quad (2.1)$$

where y_i 's are the measurements, x_i 's are the coordinates (positions), P is the number of the measured samples, ε_i 's are independent and identically distributed zero mean noise value, and $\{\beta_n\}$ are the model parameters to be estimated. Least square approach¹ [16] is usually employed to estimate the unknown model parameters. For example, in the quadratic case, the unknown parameters are estimated as

$$\min_{\{\beta_n\}} \sum_{i=1}^P [y_i - \beta_0 - \beta_1 x_i - \beta_2 x_i^2]^2. \quad (2.2)$$

Unfortunately, as natural images rarely follow such fixed models, the quality of reconstructed images is often not satisfactory.

In contrast to the parametric methods, non-parametric methods rely on the data itself to dictate the structure of the model, in which case this implicit model is referred to as *a regression function* [17]. With the relatively recent emergence of machine learning methods, kernel methods have become well-known and used frequently for pattern detection and discrimination problems [19], and estimation of real-valued functions by the *support vector method* in Chapter 11 and 13 of [20]. Surprisingly, it appears that the corresponding ideas in estimation - what we call here *kernel regression*, are not widely known or used in the image and video processing literature. Indeed, in the last decade, several concepts related to the general theory this thesis promotes here have been rediscovered in different guises, and presented under different names such as *normalized convolution* [21, 22], the *bilateral filter* [23] (the latter having been carefully investigated mathematically in [24]), *mean-shift*

¹Total least square approach [18] is a more appropriate choice when the coordinates x_i 's are also noisy. A super-resolution algorithm using kernel regression, which we will present later in this chapter, is the case.

[25], *edge directed interpolation* [26], and *moving least squares* [27]. Later in this thesis, some of these concepts and their relation to the general regression theory will be discussed. To simplify the presentation, let us first treat the univariate data case where the measured data are given by

$$y_i = z(x_i) + \varepsilon_i, \quad i = 1, 2, \dots, P, \quad (2.3)$$

where $z(\cdot)$ is the (hitherto unspecified) regression function and ε_i 's are the independent and identically distributed zero mean noise values (with otherwise no particular statistical distribution assumed). As such, kernel regression provides a rich mechanism for computing point-wise estimates of the function with minimal assumptions on the signal model.

While the particular form of $z(\cdot)$ may remain unspecified, if we assume that it is locally smooth to some order N , then to estimate the value of the function at any point x given the data, we can rely on a generic local expansion of the function about this point. Specifically, if x is near the sample at x_i , we have the N -term Taylor series²

$$z(x_i) \approx z(x) + z'(x)(x_i - x) + \frac{1}{2!}z''(x)(x_i - x)^2 + \dots + \frac{1}{N!}z^{(N)}(x)(x_i - x)^N \quad (2.4)$$

$$= \beta_0 + \beta_1(x_i - x) + \beta_2(x_i - x)^2 + \dots + \beta_N(x_i - x)^N. \quad (2.5)$$

The above suggests that if we now think of the Taylor series as a local representation of the regression function, estimating the parameter β_0 yields the desired (local) estimate of the regression function based on the data. Indeed, the other parameters $\{\beta_n\}_{n=1}^N$ will provide localized information on the n -th *derivatives* of the regression function. Naturally, since this approach is based on *local* approximations, a logical step to take is to estimate the parameters $\{\beta_n\}_{n=0}^N$ from the data while giving the nearby samples higher weight than samples farther away. A weighted least-square formulation [16] capturing this idea is to

²Other expansions are also possible, e.g. orthogonal series.

solve the following optimization problem:

$$\min_{\{\beta_n\}_{n=0}^N} \sum_{i=1}^P [y_i - \beta_0 - \beta_1(x_i - x) - \beta_2(x_i - x)^2 - \dots - \beta_N(x_i - x)^N]^2 \frac{1}{h} K\left(\frac{x_i - x}{h}\right), \quad (2.6)$$

where $K(\cdot)$ is the *kernel function* (weight function) [17] which penalizes distance away from the local position where the approximation is centered, and the *smoothing parameter* h (also called the *bandwidth*) controls the strength of this penalty. In particular, the function $K(\cdot)$ is a symmetric function which attains its maximum at zero, satisfying

$$\int_{R^1} tK(t)dt = 0, \quad \int_{R^1} t^2K(t)dt = c, \quad (2.7)$$

where c is a some constant value. The choice of the particular form of the function $K(\cdot)$ is open, and may be selected as a Gaussian, exponential, or other forms which comply with the above constraints (some popular choice of $K(\cdot)$ are shown in Table **2.1**). Experimental studies such as in [28] show that the choice of the kernel has an insignificant effect on the accuracy of estimation and therefore the preference is given to the differentiable kernels with low computational complexity such as the Gaussian kernel.

Several important point are worth making here. First, the above structure allows for tailoring the estimation problem to the *local* characteristics of the data, whereas the standard parametric model is intended as a more global fit. Second, in the estimation of the local structure, higher weight is given to the nearby data as compared to samples that are farther away from the center of the analysis window. Meanwhile, this approach does not specifically require that the data follow a regular or periodic sampling structure. More specifically, so long as the samples are near the point x , the non-parametric framework (2.6) is valid. Again this is in contrast to the general parametric approach (e.g. (2.2)) which generally either does not directly take the location of the data samples into account, or

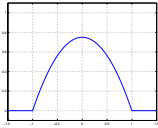
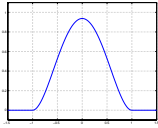
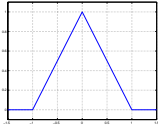
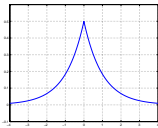
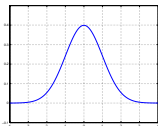
Epanechnikov:		$K(t) = \begin{cases} \frac{3}{4}(1-t^2) & \text{for } t < 1 \\ 0 & \text{otherwise} \end{cases}$
Biweight:		$K(t) = \begin{cases} \frac{15}{16}(1-t^2)^2 & \text{for } t < 1 \\ 0 & \text{otherwise} \end{cases}$
Triangle:		$K(t) = \begin{cases} 1- t & \text{for } t < 1 \\ 0 & \text{otherwise} \end{cases}$
Laplacian:		$K(t) = \frac{1}{2} \exp(- t)$
Gaussian:		$K(t) = \frac{1}{\sqrt{2\pi}} \exp\left(-\frac{1}{2}t^2\right)$

Table 2.1: Popular choices for the kernel function.

relies on regular sampling over a grid. Third, and no less important, the proposed approach is useful for both *denoising*, and equally viable for *interpolation* of sampled data at points where no actual samples exist. Given the above observations, the kernel-based methods appear to be well-studied for a wide class of image processing problems of practical interest.

Returning to the estimation problem based upon (2.6), one can choose the order N to effect an increasingly more complex local approximation of the signal. In the non-parametric statistics literature, locally constant, locally linear, and locally quadratic approximations (corresponding to $N = 0, 1, 2$) have been considered most widely [17, 29, 30, 31]. In particular, choosing $N = 0$, a locally adaptive *linear* filter is obtained, which is known

as the *Nadaraya-Watson Estimator* (NWE) [13]. Specifically, this estimator has the form

$$\hat{z}(x) = \frac{\sum_{i=1}^P K_h(x_i - x) y_i}{\sum_{i=1}^P K_h(x_i - x)}, \quad K_h(t) = \frac{1}{h} K\left(\frac{t}{h}\right). \quad (2.8)$$

When all the data y_i 's are uniformly distributed as shown in Figure 1.1(c), the NWE is nothing but a simple convolution that has been practiced for 100 years in signal processing.

As described earlier, the NWE is the simplest manifestation of an adaptive filter resulting from the kernel regression framework. As we shall see later in Section 3.2.1, the *bilateral filter* [23, 24] can be interpreted as a generalization of the NWE with a modified kernel definition.

Of course, higher order approximations ($N > 0$) are also possible. Note that the choice of the order in parallel with the smoothness h affect the bias and variance of estimation. Mathematical expression for bias and variance can be found in [32, 33], and therefore here we briefly review their properties. In general, lower order approximates such as NWE ($N = 0$), result in smoother images (large bias and small variance) as there are not enough degree of freedom. On the contrary, over-fitting happens in regression using higher orders of approximation, resulting in small bias and large estimation variance. We also note that smaller values for h result in small bias and consequently large variance in estimates. Optimal order and smoothing parameter selection procedures are studied in [27].

The performance of kernel regressors of different orders is compared in the illustrative examples of Figure 2.1. In the first experiment, illustrated in the first row, a set of moderately noisy (variance of the additive Gaussian noise is 0.1) equally-spaced samples of a function are used to estimate the underlying function. As expected, the computationally more complex high order interpolation ($N = 2$) results in a better estimate than the lower

ordered interpolators ($N = 0$ or 1). The presented quantitative comparison of RMSE³ supports this claim. The second experiment, illustrated in the second row, shows that for the heavily noisy data sets (variance of the additive Gaussian noise is 0.5), the performance of lower ordered regressors is better. Note that the performance of the $N = 0$ and $N = 1$ ordered estimators for these equally-spaced sampled experiments are identical. In Section 2.3.2, we study this property in more detail.

2.2.1 Related Regression Methods

In addition to kernel regression methods, which this thesis is advocating, there are several other effective regression methods such as B-spline interpolation [11], orthogonal series [34, 30], cubic spline interpolation [12] and spline smoother [30, 11, 35]. We briefly review these methods and see how they are related in this section.

Following the notation used in the previous subsection, the B-spline interpolation is expressed as the linear combination of shifted spline functions

$$z(x) = \sum_k \beta_k B^q(x - k), \quad (2.9)$$

where the q^{th} order B-spline function is defined as a $q + 1$ times convolution of the zero-th order B-spline function [11],

$$B^q(x) = \underbrace{B^0(x) * B^0(x) * \dots * B^0(x)}_{q+1}, \quad \text{where } B^0(x) = \begin{cases} 1, & -\frac{1}{2} < x < \frac{1}{2} \\ \frac{1}{2}, & |x| = \frac{1}{2} \\ 0, & \text{else} \end{cases} \quad (2.10)$$

The scalar k in (2.9), often referred to as the *knot*, defines the center of a spline. The least squares formulation [16] is usually exploited to estimate the B-spline coefficients $\{\beta_k\}$.

³Root Mean Square Error of an estimate is defined as $\text{RMSE} = \sqrt{\text{E}\{(z(x) - \hat{z}(x))^2\}}$, where E is the *expected value* operator.

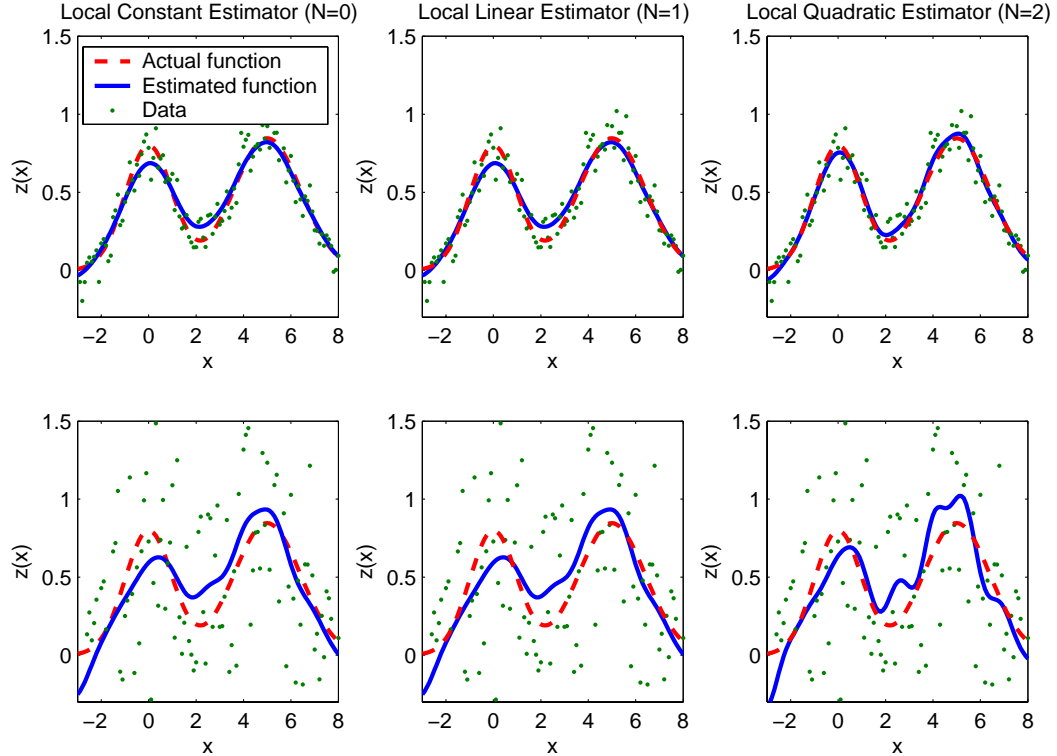


Figure 2.1: Examples of local polynomial regression of an equally-spaced data set. The signals in the first and second rows are contaminated with the Gaussian noise of $\text{var}(\varepsilon_i) = 0.1$ and 0.5 , respectively. The dashed, solid lines, and dots represent the actual function, estimated function, and the noisy data, respectively. The columns from left to right show the constant, linear, and quadratic interpolation results. Corresponding RMSE's for the first row experiments are 0.0025, 0.0025, 0.0009 and for the second row are as 0.0172, 0.0172, 0.0201.

The B-spline interpolation method bears some similarities to the kernel regression method. One major difference between these method is in the number and position of the knots as illustrated in Figure 2.2. While in the classical B-spline method the knots are located in equally spaced positions, in the case of kernel regression the knots are implicitly located on the sample positions. A related method, the *Non-Uniform Rational B-Spline* (NURBS) is also proposed in [36] to address this shortcoming of the classical B-spline method, by irregularly positioning the knots with respect to the underlying signal.

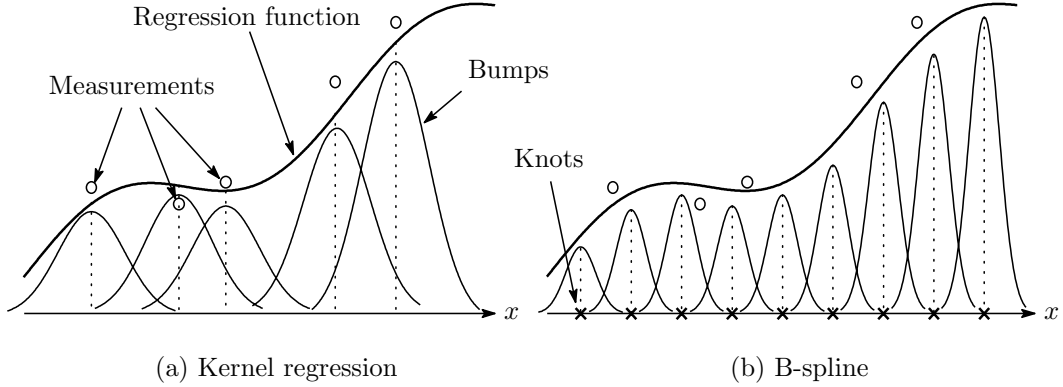


Figure 2.2: A comparison of the position of knots in (a) Kernel regression and (b) classical B-Spline methods.

Cubic spline interpolation technique is one of the most popular members of the spline interpolation family which is based on fitting a polynomial between any pair of consecutive data. Assuming that the second derivative of the regression function exists, cubic spline interpolation is defined as

$$z(x) = \beta_0(i) + \beta_1(i)(x_i - x) + \beta_2(i)(x_i - x)^2 + \beta_3(i)(x_i - x)^3, x \in [x_i, x_{i+1}], \quad (2.11)$$

where under the following boundary conditions

$$\begin{aligned} z(x)\Big|_{x_i^-} &= z(x)\Big|_{x_i^+}, & z'(x)\Big|_{x_i^-} &= z'(x)\Big|_{x_i^+}, & z''(x)\Big|_{x_i^-} &= z''(x)\Big|_{x_i^+}, \\ z''(x_1) &= z''(x_P) = 0, \end{aligned} \quad (2.12)$$

all the coefficients B_i 's can be uniquely defined [12].

Note that an estimated curve by cubic spline interpolation passes through all data points which is ideal for the noiseless data case. However, in most practical applications, data are contaminated with noise and therefore such perfect fits are no longer desirable. Consequently a related method called spline smoother is proposed. In spline smoother the above hard conditions are replaced with soft ones, by introducing them as Bayesian priors which penalize rather than constrain non-smoothness in the interpolated images. A popular

implementation of the spline smoother [11] is given by

$$\hat{z}(x) = \arg \min_{z(x)} \left[\sum_{i=1}^P \{y_i - z(x_i)\}^2 + \lambda \|z''\|_2^2 \right], \quad \|z''\|_2^2 = \int \{z''(x)\}^2 dx, \quad (2.13)$$

where $z(x_i)$ can be replaced by either (2.9) or any orthogonal series⁴, and λ is the regularization parameter. Note that assuming a continuous sample density function, the solution to this minimization problem is equivalent to the NWE (2.8) with the following kernel function and a variable smoothing parameter h

$$K(t) = \frac{1}{2} \exp\left(-\frac{|t|}{\sqrt{2}}\right) \sin\left(\frac{|t|}{\sqrt{2}} + \frac{\pi}{4}\right), \quad h(x_i) = \left(\frac{\lambda}{Pf(x_i)}\right)^{\frac{1}{4}}, \quad (2.14)$$

where $f(\cdot)$ is the density of samples [30, 38]. In Chapter 5, performance comparisons with data-adapted kernel regression (q.v. Chapter 3) will be presented.

2.3 Kernel Regression for Bivariate Data and its Properties

This section introduces the formulation of the classical kernel regression method for bivariate data and establishes its relation with the linear filtering idea. Some intuitions on computational efficiency will be also provided as well as weakness of this method, which motivate the development of more powerful regression tools in the next chapter.

2.3.1 Kernel Regression Formulation

Similar to the univariate data case in (2.3), the model of bivariate data (e.g. the samples in Figure 1.1(b)) is given by

$$y_i = z(\mathbf{x}_i) + \varepsilon_i, \quad \mathbf{x}_i = [x_{1i}, x_{2i}]^T, \quad i = 1, 2, \dots, P, \quad (2.15)$$

⁴A successful implementation based on this method for image reconstruction has done by Arigovindan et al. [37].

where the coordinates of the measured data y_i is now the 2×1 vector \mathbf{x}_i . Correspondingly, the local expansion of the regression function is given by

$$\begin{aligned} z(\mathbf{x}_i) &\approx z(\mathbf{x}) + \{\nabla z(\mathbf{x})\}^T (\mathbf{x}_i - \mathbf{x}) + \frac{1}{2!} (\mathbf{x}_i - \mathbf{x})^T \{\mathcal{H}z(\mathbf{x})\} (\mathbf{x}_i - \mathbf{x}) + \dots \\ &= z(\mathbf{x}) + \{\nabla z(\mathbf{x})\}^T (\mathbf{x}_i - \mathbf{x}) + \frac{1}{2} \text{vec}^T \{\mathcal{H}z(\mathbf{x})\} \text{vec} \{(\mathbf{x}_i - \mathbf{x})(\mathbf{x}_i - \mathbf{x})^T\} + \dots, \end{aligned} \quad (2.16)$$

where ∇ and \mathcal{H} are the gradient and Hessian operators, respectively and $\text{vec}(\cdot)$ is the vectorization operator [32], which lexicographically orders a matrix into a vector. Defining $\text{vech}(\cdot)$ as the half-vectorization operator [32] of the lower-triangular portion of the matrix, e.g.,

$$\text{vech} \left(\begin{bmatrix} a_{11} & a_{12} \\ a_{21} & a_{22} \end{bmatrix} \right) = [a_{11} \ a_{21} \ a_{22}]^T, \quad (2.17)$$

$$\text{vech} \left(\begin{bmatrix} a_{11} & a_{12} & a_{13} \\ a_{21} & a_{22} & a_{23} \\ a_{31} & a_{32} & a_{33} \end{bmatrix} \right) = [a_{11} \ a_{21} \ a_{31} \ a_{23} \ a_{32} \ a_{33}]^T, \quad (2.18)$$

and considering the symmetry of the Hessian matrix, (2.16) simplifies to

$$z(\mathbf{x}_i) = \beta_0 + \beta_1^T (\mathbf{x}_i - \mathbf{x}) + \beta_2^T \text{vech} \{(\mathbf{x}_i - \mathbf{x})(\mathbf{x}_i - \mathbf{x})^T\} + \dots. \quad (2.19)$$

Then, comparison between (2.16) and (2.19) suggests that $\beta_0 = z(\mathbf{x})$ is the pixel value of interest and the vectors β_1 and β_2 are

$$\beta_1 = \left[\left. \frac{\partial z(\mathbf{x})}{\partial x_1} \right|_{\mathbf{x}=\mathbf{x}_i} \quad \left. \frac{\partial z(\mathbf{x})}{\partial x_2} \right|_{\mathbf{x}=\mathbf{x}_i} \right]^T, \quad (2.20)$$

$$\beta_2 = \frac{1}{2} \left[\left. \frac{\partial^2 z(\mathbf{x})}{\partial x_1^2} \right|_{\mathbf{x}=\mathbf{x}_i} \quad 2 \left. \frac{\partial^2 z(\mathbf{x})}{\partial x_1 \partial x_2} \right|_{\mathbf{x}=\mathbf{x}_i} \quad \left. \frac{\partial^2 z(\mathbf{x})}{\partial x_2^2} \right|_{\mathbf{x}=\mathbf{x}_i} \right]^T. \quad (2.21)$$

As in the case of univariate data, the $\{\beta_n\}$ are computed from the following optimization problem:

$$\min_{\{\beta_n\}_{n=0}^N} \sum_{i=1}^P \left[y_i - \beta_0 - \beta_1^T (\mathbf{x}_i - \mathbf{x})^T - \beta_2^T \text{vech} \{ (\mathbf{x}_i - \mathbf{x})(\mathbf{x}_i - \mathbf{x})^T \} - \dots \right]^2 K_{\mathbf{H}}(\mathbf{x}_i - \mathbf{x}), \quad (2.22)$$

with

$$K_{\mathbf{H}}(\mathbf{t}) = \frac{1}{\det(\mathbf{H})} K(\mathbf{H}^{-1}\mathbf{t}), \quad (2.23)$$

where $K(\cdot)$ is the 2-D realization of the kernel function illustrated in Table 2.1, and \mathbf{H} is the 2×2 smoothing matrix, which will be studied more carefully later in this chapter. It is also possible to express (2.22) in a matrix form as a weighted least squares optimization problem [16, 27],

$$\arg \min_{\mathbf{b}} \|\mathbf{y} - \mathbf{X}_x \mathbf{b}\|_{\mathbf{W}_x}^2 = \arg \min_{\mathbf{b}} (\mathbf{y} - \mathbf{X}_x \mathbf{b})^T \mathbf{W}_x (\mathbf{y} - \mathbf{X}_x \mathbf{b}), \quad (2.24)$$

where

$$\mathbf{y} = [y_1 \ y_2 \ \dots \ y_P]^T, \quad \mathbf{b} = [\beta_0 \ \beta_1^T \ \beta_2^T \ \dots]^T, \quad (2.25)$$

$$\mathbf{W}_x = \text{diag} [K_{\mathbf{H}}(\mathbf{x}_1 - \mathbf{x}), K_{\mathbf{H}}(\mathbf{x}_2 - \mathbf{x}), \dots, K_{\mathbf{H}}(\mathbf{x}_P - \mathbf{x})], \quad (2.26)$$

$$\mathbf{X}_x = \begin{bmatrix} 1 & (\mathbf{x}_1 - \mathbf{x})^T & \text{vech}^T \{ (\mathbf{x}_1 - \mathbf{x})(\mathbf{x}_1 - \mathbf{x})^T \} & \dots \\ 1 & (\mathbf{x}_2 - \mathbf{x})^T & \text{vech}^T \{ (\mathbf{x}_2 - \mathbf{x})(\mathbf{x}_2 - \mathbf{x})^T \} & \dots \\ \vdots & \vdots & \vdots & \vdots \\ 1 & (\mathbf{x}_P - \mathbf{x})^T & \text{vech}^T \{ (\mathbf{x}_P - \mathbf{x})(\mathbf{x}_P - \mathbf{x})^T \} & \dots \end{bmatrix}, \quad (2.27)$$

with “diag” defining the diagonal elements of a diagonal matrix.

Regardless of the regression order (N), as our primary interest is to compute an estimate of the image (pixel values), the necessary computations are limited to the ones that estimate the parameter β_0 . Therefore the weighted least squares estimation is simplified to

$$\hat{z}(\mathbf{x}) = \hat{\beta}_0 = \mathbf{e}_1^T (\mathbf{X}_x^T \mathbf{W}_x \mathbf{X}_x)^{-1} \mathbf{X}_x^T \mathbf{W}_x \mathbf{y}, \quad (2.28)$$

where \mathbf{e}_1 is a column vector (the same size of \mathbf{b} in (2.25)) with the first element equal to 1, and the rest equal to zero. Of course, there is a fundamental difference between computing β_0 for the $N = 0$ case, and using a high order estimator ($N > 0$) and then effectively discarding direct calculation of all $\{\beta_n\}$ except β_0 . Unlike the former case, the latter method computes estimates of pixel values assuming a N^{th} order locally polynomial structure is present.

2.3.2 Equivalent Kernel

In this subsection we derive a computationally more efficient and intuitive solution to the classic kernel regression problem. Study of (2.28) shows that $\mathbf{X}_{\mathbf{x}}^T \mathbf{W}_{\mathbf{x}} \mathbf{X}_{\mathbf{x}}$ is a $(N + 1) \times (N + 1)$ block matrix, with the following structure:

$$\mathbf{X}_{\mathbf{x}}^T \mathbf{W}_{\mathbf{x}} \mathbf{X}_{\mathbf{x}} = \begin{bmatrix} \mathbf{s}_{11} & \mathbf{s}_{12} & \mathbf{s}_{13} & \cdots \\ \mathbf{s}_{21} & \mathbf{s}_{22} & \mathbf{s}_{23} & \cdots \\ \mathbf{s}_{31} & \mathbf{s}_{32} & \mathbf{s}_{33} & \cdots \\ \vdots & \vdots & \vdots & \ddots \end{bmatrix}, \quad (2.29)$$

where \mathbf{s}_{lm} is an $l \times m$ matrix (a block). The block elements of (2.29) for the orders of up to $N = 2$ are as follows:

$$\mathbf{s}_{11} = \sum_{i=1}^P K_{\mathbf{H}}(\mathbf{x}_i - \mathbf{x}) \quad (2.30)$$

$$\mathbf{s}_{12} = \mathbf{s}_{21}^T = \sum_{i=1}^P (\mathbf{x}_i - \mathbf{x})^T K_{\mathbf{H}}(\mathbf{x}_i - \mathbf{x}) \quad (2.31)$$

$$\mathbf{s}_{22} = \sum_{i=1}^P (\mathbf{x}_i - \mathbf{x})(\mathbf{x}_i - \mathbf{x})^T K_{\mathbf{H}}(\mathbf{x}_i - \mathbf{x}) \quad (2.32)$$

$$\mathbf{s}_{13} = \mathbf{s}_{31}^T = \sum_{i=1}^P \text{vech}^T\{(\mathbf{x}_i - \mathbf{x})(\mathbf{x}_i - \mathbf{x})^T\} K_{\mathbf{H}}(\mathbf{x}_i - \mathbf{x}) \quad (2.33)$$

$$\mathbf{s}_{23} = \mathbf{s}_{32}^T = \sum_{i=1}^P (\mathbf{x}_i - \mathbf{x}) \text{vech}^T\{(\mathbf{x}_i - \mathbf{x})(\mathbf{x}_i - \mathbf{x})^T\} K_{\mathbf{H}}(\mathbf{x}_i - \mathbf{x}) \quad (2.34)$$

$$\mathbf{s}_{33} = \sum_{i=1}^P \text{vech}\{(\mathbf{x}_i - \mathbf{x})(\mathbf{x}_i - \mathbf{x})^T\} \text{vech}^T\{(\mathbf{x}_i - \mathbf{x})(\mathbf{x}_i - \mathbf{x})^T\} K_{\mathbf{H}}(\mathbf{x}_i - \mathbf{x}). \quad (2.35)$$

Considering the above shorthand notation, (2.28) can be represented as a local *linear filtering process*:

$$\hat{z}(\mathbf{x}) = \sum_{i=1}^P W_i(\mathbf{x}; N, \mathbf{H}) y_i, \quad (2.36)$$

where

$$W_i(\mathbf{x}; 0, \mathbf{H}) = \frac{K_{\mathbf{H}}(\mathbf{x}_i - \mathbf{x})}{s_{11}} \quad (2.37)$$

$$W_i(\mathbf{x}; 1, \mathbf{H}) = \frac{\{1 - \mathbf{s}_{12} \mathbf{S}_{22}^{-1}(\mathbf{x}_i - \mathbf{x})\} K_{\mathbf{H}}(\mathbf{x}_i - \mathbf{x})}{s_{11} - \mathbf{s}_{12} \mathbf{S}_{22}^{-1} \mathbf{s}_{21}} \quad (2.38)$$

$$W_i(\mathbf{x}; 2, \mathbf{H}) = \frac{\left[1 - \mathbf{S}_{12} \mathbf{S}_{22}^{-1}(\mathbf{x}_i - \mathbf{x}) - \mathbf{S}_{13} \mathbf{S}_{33}^{-1} \text{vech}\{(\mathbf{x}_i - \mathbf{x})(\mathbf{x}_i - \mathbf{x})^T\}\right] K_{\mathbf{H}}(\mathbf{x}_i - \mathbf{x})}{s_{11} - \mathbf{S}_{12} \mathbf{S}_{22}^{-1} \mathbf{s}_{21} - \mathbf{S}_{13} \mathbf{S}_{33}^{-1} \mathbf{s}_{31}}. \quad (2.39)$$

and

$$\begin{aligned} \mathbf{S}_{12} &= \mathbf{s}_{12} - \mathbf{s}_{13} \mathbf{S}_{33}^{-1} \mathbf{s}_{32}, & \mathbf{S}_{22} &= \mathbf{s}_{22} - \mathbf{s}_{23} \mathbf{S}_{33}^{-1} \mathbf{s}_{32}, \\ \mathbf{S}_{13} &= \mathbf{s}_{13} - \mathbf{s}_{12} \mathbf{S}_{22}^{-1} \mathbf{s}_{23}, & \mathbf{S}_{33} &= \mathbf{s}_{33} - \mathbf{s}_{32} \mathbf{S}_{22}^{-1} \mathbf{s}_{23}. \end{aligned} \quad (2.40)$$

Therefore, regardless of the order, the classical kernel regression is nothing but local weighted averaging of data (linear filtering), where the order determines the type and complexity of the weighting scheme. This also suggest that the high order regressions ($N > 0$) are equivalent of the zero-th order regression ($N = 0$) with a more complex kernel function. In other words, to effect the higher order regressions, the original kernel $K_{\mathbf{H}}(\mathbf{x}_i - \mathbf{x})$ is modified to yield a newly adapted *equivalent* kernel [33].

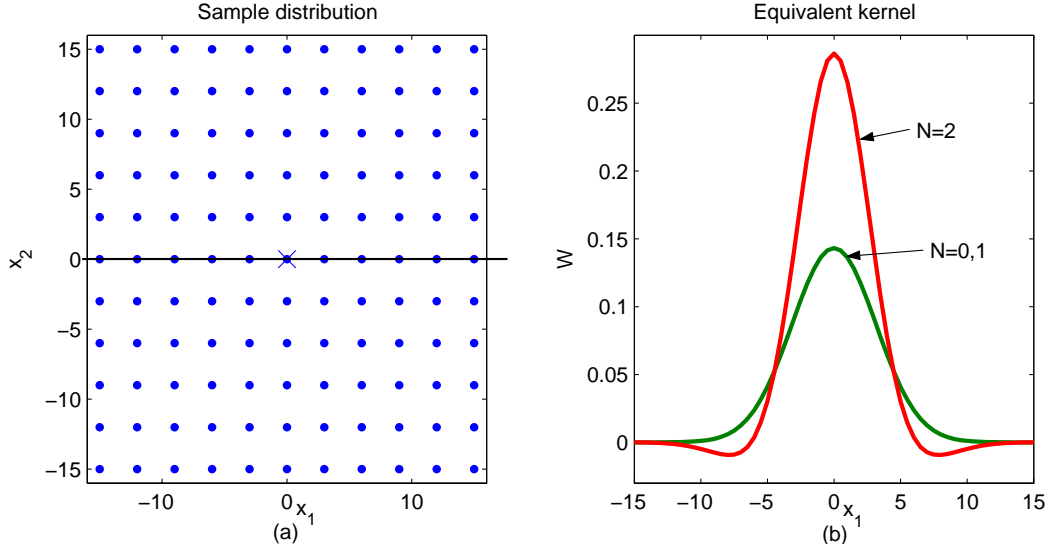


Figure 2.3: (a) A uniformly sampled data set. (b) A horizontal slice of the equivalent kernels of orders $N = 0, 1$, and 2 for the regularly sampled data in (a). The kernel $K_{\mathbf{H}}$ in (2.22) is modeled as a Gaussian, with the smoothing matrix $\mathbf{H} = \text{Diag}[10, 10]$.

To have a better intuition of equivalent kernels, we study the example in Figure 2.3, which illustrates a uniformly sampled data set and the horizontal slices of its corresponding equivalent kernels for the regression orders $N = 0, 1$ and 2. The direct result of the symmetry condition (2.7) on $K_{\mathbf{H}}(\mathbf{x}_i - \mathbf{x})$ with uniformly sampled data is that all odd-order moments ($\mathbf{s}_{2j, 2k+1}$ and $\mathbf{s}_{2k+1, 2j}$)'s consist of elements with values very close to zero. As this observation holds for all regression orders, for *the regularly sampled data*, the $N = 2q - 1$ order regression is preferred to the computationally more complex $N = 2q$ order regression, as they produce almost identical results. This property manifests itself in Figure 2.3, where the $N = 0$ or 1 ordered equivalent kernels are identical.

This example also shows that unlike the $N = 0, 1$ cases in which the equivalent kernel only consists of positive values, the second order equivalent kernel has both positive and negative elements. Therefore, when we look at the response of equivalent kernel in the

frequency domain, the second order equivalent kernel has a clearer cutoff between passed and filtered frequencies than the zero-th or first order equivalent kernel. The response of the second order one is very similar to the second order Butterworth low-pass filter.

In the next experiment, we compare the equivalent kernels for an irregularly sampled data set shown in Figure 2.4(a). The second order equivalent kernel for the sample marked with “×”, is shown in Figure 2.4(b). Figure 2.4(c) and Figure 2.4(d) show the horizontal and vertical slices of this kernel, respectively. This figure demonstrates the fact that the equivalent kernels tend to adapt themselves to the density of available samples. Also, unlike the regularly sampled data case, since the odd-order moments are not equal to zero, the $N = 0$ and $N = 1$ equivalent kernels are no longer identical.

2.3.3 The Selection of Smoothing Matrices

The spread of the kernel as defined in (2.23), and consequently the performance of the estimator, depend on the choice of the smoothing matrix \mathbf{H} [32]. For the bivariate data cases, the smoothing matrix is a 2×2 positive definite matrix which is generally defined for each measured sample as

$$\mathbf{H}_i = \begin{bmatrix} h_{1i} & h_{2i} \\ h_{3i} & h_{4i} \end{bmatrix}, \quad (2.41)$$

where \mathbf{H}_i extends the kernel⁵ to contain a *sufficient* number of samples. As illustrated in Figure 2.5, it is reasonable to use smaller kernels in the areas with more available samples, and likewise larger footprint is more suitable for the more sparsely sampled regions of the image.

The cross validation (leave-one-out) method [17, 30] is a popular method for es-

⁵The kernel is often called the *mercer kernel*, which measures similarity between data, in vast literature on kernel based regression in multidimensional machine learning, and the way to define the smoothing matrix \mathbf{H}_i by (2.41) is a more general version of the mercer kernels.

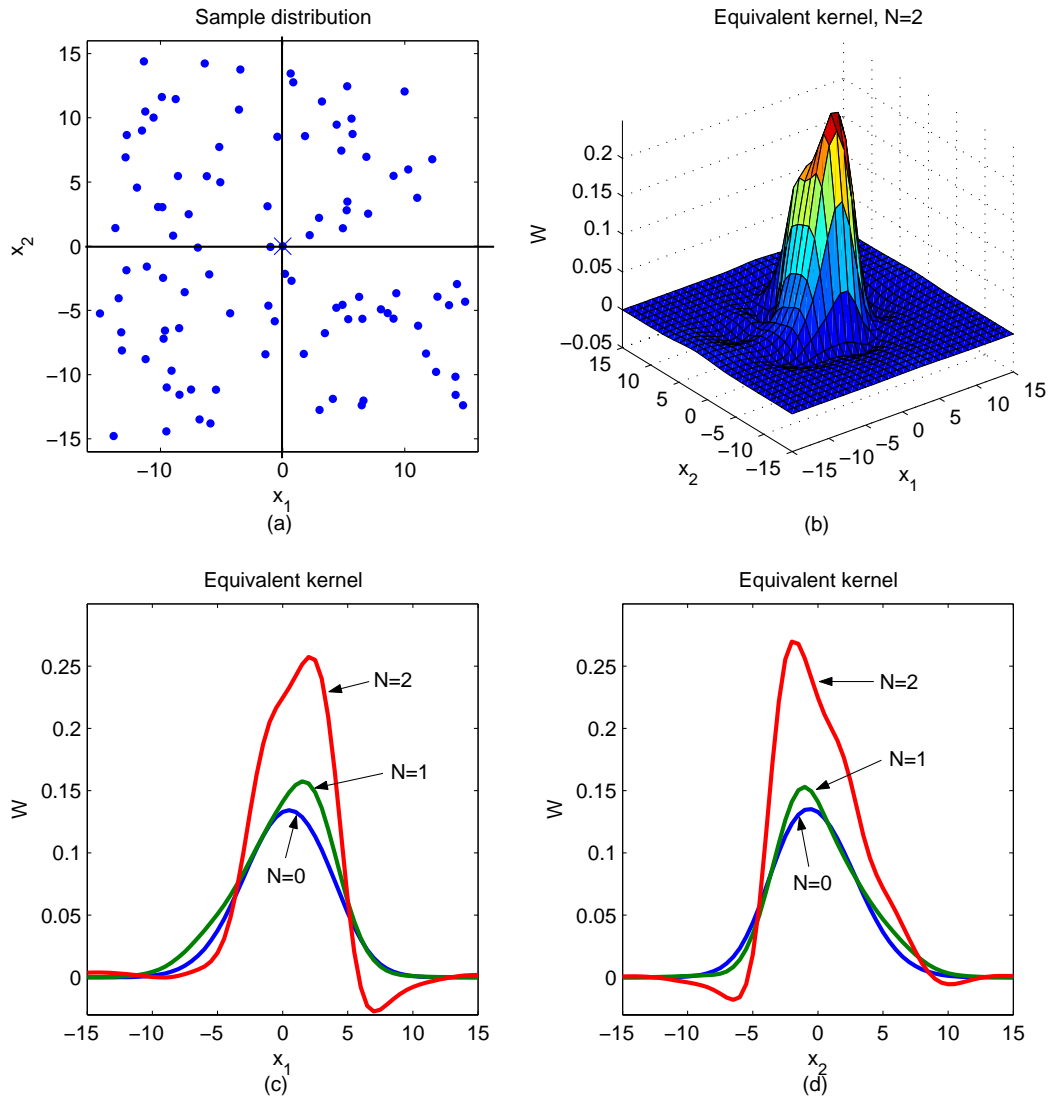


Figure 2.4: Equivalent kernels for an irregularly sampled data set are shown in (a). (b) is the second order ($N = 2$) equivalent kernel. The horizontal and vertical slices of the equivalent kernels of different orders ($N = 0, 1, 2$) are compared in (c) and (d), respectively. In this example, the kernel $K_{\mathbf{H}}$ in (2.22) was modeled as a Gaussian, with the smoothing matrix $\mathbf{H} = \text{Diag}[10, 10]$.

estimating the elements of the local \mathbf{H}_i 's. However, as the cross validation method is computationally very expensive, we usually use a simplified and computationally more efficient

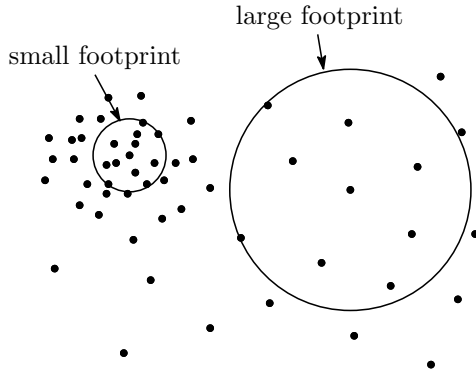


Figure 2.5: Smoothing (kernel size) selection by sample density.

model of the smoothing matrices as

$$\mathbf{H}_i = h\mu_i\mathbf{I}, \quad (2.42)$$

where μ_i is a scalar that captures the local density of the data samples and h is the *global smoothing parameter*.

The global smoothing parameter is directly computed from the cross validation method, by minimizing the following cost function

$$\zeta_{\text{cv}}(h) = \sum_{i=1}^P \{\hat{z}_{h,\ddagger}(\mathbf{x}_i) - y_i\}^2, \quad (2.43)$$

where $\hat{z}_{h,\ddagger}(\mathbf{x}_i)$ is the estimated pixel values without the i^{th} sample with the global smoothing parameter h . As ζ_{cv} might not be differentiable, we use the Nelder-Mead optimization algorithm [39] to estimate h . To further reduce the computations, rather than leaving a single sample out, it is possible to leave out a set of samples (a hole row and column).

Following [28], the *local density parameter* μ_i is estimated as follows

$$\mu_i = \left(\frac{f(\mathbf{x}_i)}{g} \right)^{-\alpha}, \quad (2.44)$$

where $f(\cdot)$ is the density function measured by the *kernel density estimator* [28] as

$$f(\mathbf{x}) = \frac{1}{P} \sum_{i=1}^P K_{\mathbf{H}}(\mathbf{x}_i - \mathbf{x}), \quad (2.45)$$

g is the geometric mean of the density function $f(\cdot)$ given by

$$g = \exp \left\{ \frac{1}{P} \sum_{i=1}^P \log f(\mathbf{x}_i) \right\}. \quad (2.46)$$

and α is the *density sensitivity parameter* which is a scalar satisfying⁶ $0 < \alpha < 1.0$. μ_i obtained by this method has the property of $E\{\mu_i\} = 1$, that is to say that the parameter makes the footprint slightly larger at a sparse region and slightly smaller at a dense region.

As h and μ_i are interdependent, we estimate them iteratively. That is, in one iteration by fixing h , the μ_i is estimated. In the next iteration μ_i is fixed and h is estimated. This process is repeated a few times until more reliable estimates of \mathbf{H}_i 's are obtained. However, we cannot guarantee the convergence of this iterative method. Constructing an algorithm for this is an ongoing work.

2.4 Super-Resolution by Kernel Regression

This section presents a super-resolution algorithm using the kernel regression technique. The block diagram of the algorithm is illustrated in Figure 2.6. Suppose we have N frames. First, we estimate motion between every pair of frames (q.v. Chapter 4). Once the motion is available, the image fusion method (Shift-and-Add method) shown in Figure 1.2 gives a data set $\{y_i, \mathbf{x}_i\}_{i=1}^P$. This data set is irregularly sampled data in all the time unless we have perfect motion estimation. Second, using the kernel regression method (2.36), we

⁶In this thesis, we choose $\alpha = 0.5$, which is proved in [40] to be an appropriate choice for the density sensitivity parameter.

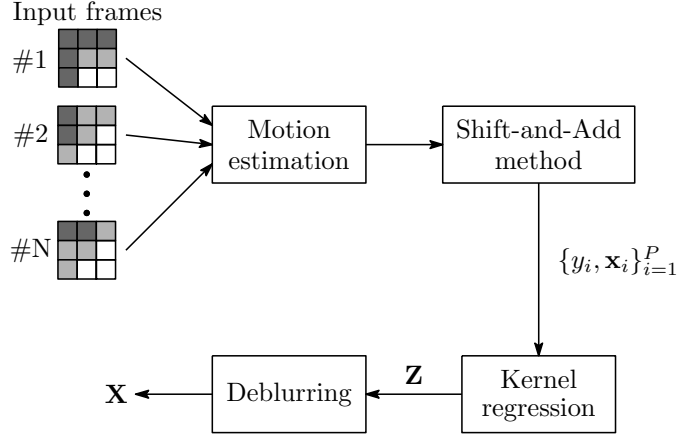


Figure 2.6: The block diagram of the super-resolution algorithm using kernel regression.

estimate the high resolution image \mathbf{Z} , which is defined as

$$\mathbf{Z} = \begin{bmatrix} z(1,1) & z(1,2) & \cdots & z(1,rM) \\ z(2,1) & z(2,2) & \cdots & z(2,rM) \\ \vdots & \vdots & \ddots & \vdots \\ z(rL,1) & z(rL,2) & \cdots & z(rL,rM) \end{bmatrix}. \quad (2.47)$$

However the estimated image \mathbf{Z} is often blurry due to the blur effects caused by atmospheric turbulence and camera aperture. Hence, third, we need to deblur it by using (A.2) in Appendix A in order to obtain the sharper image \mathbf{X} .

In Figure 2.7, an simple example on Tank sequence shown in Figure 1.4 is illustrated with the algorithm just stated above. Figures 2.7(a), (b), and (c) are showing the estimated images by (2.36) with the regression order $N = 0, 1$, and 2 , respectively. The same global smoothing parameter, $h = 0.8$, was used for each case. We can see the significant improvements between the regression order 0 and 1, since equivalent kernels are different in the case of irregularly sampled data (see Figure 2.4). With the second order ($N = 2$),

we have an even better image (Figure 2.7(c)). Using the deblurring technique described in Appendix A (5×5 Gaussian blur kernel with variance 1.0, the regularization term of 5×5 bilateral total variation, the regularization parameter $\lambda = 0.2$ and $\alpha = 0.5$ are used with 50 iterations), the final output is shown in Figure 2.7(d), as applied on the image in Figure 2.7(c).

2.5 Summary

In this chapter we reviewed the classical kernel regression framework, and showed that it can be regarded as a locally adaptive linear filtering process and an example of image reconstruction on the tank sequence. The tank sequence has relatively little noise and no compression artifacts, hence the reconstructed image are quite good. However a real video sequence could have more noise and compression artifacts. In order to produce a superior quality output from such a severe case, in the next chapter, we propose and study the *adaptive kernel regression* methods with locally non-linear filtering properties.



Figure 2.7: A super-resolution example on the tank sequence.

Chapter 3

Data-Adapted Kernel Regression

3.1 Introduction

In the previous chapter, we studied the kernel regression method, its properties, and showed its usefulness for image restoration and reconstruction purpose. One fundamental improvement on the above method can be realized by noting that, the local polynomial kernel regression estimates, independent of the order (N), are always local *linear* combinations (weighted averages) of the data. As such, though elegant, relatively easy to analyze, and with attractive asymptotic properties [32], they suffer from an inherent limitation due to this local linear action on the data. In what follows, we discuss extensions of the kernel regression method that enable this structure to have nonlinear, more effective, action on the data.

A strong denoising effect and interpolating all the pixels from a very sparse data set can be realized by making the global smoothing parameter (h) larger. However, with such a larger h , the estimated image will be more blurred so that we have sacrificed details.

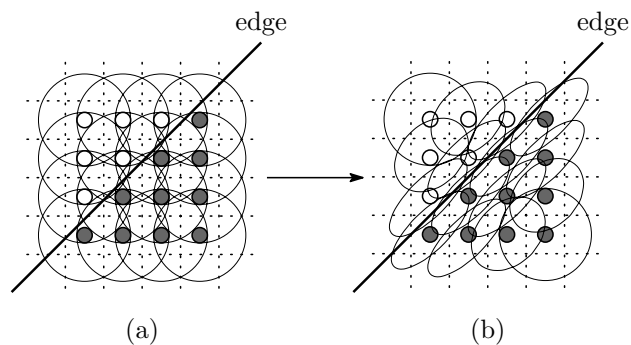


Figure 3.1: Kernel spread in a uniformly sampled data set. (a) Kernels in the classic method depend only on the sample density. (b) Data-adapted kernels elongate with respect to the edge.

In order to have both a strong denoising/interpolating effect and a sharper image, one can consider an alternative approach that will adapt the local effect of the filter using not only the position of the nearby samples, but also their gray values. That is to say, the proposed kernels will take into account two factors: spatial distances and radiometric (gray value) distances. With this idea, this chapter presents a novel non-linear filter algorithm called *data-adapted (or steered) kernel regression*.

3.2 Data-Adapted Kernel Regression

Data-adapted kernel regression methods rely not only on the sample density, but also on the benefits of edge artifacts from the radiometric properties of these samples. Therefore, the effective size and spread of the kernel is locally adapted to the structure of objects on an image. This property is illustrated in Figure 3.1, where the classical kernel spreads and the adaptive kernel spreads in presence of an edge are compared.

On the data-adapted kernel regression approach, in order to take into account the structure information of a data set, we can simply add one more concept to the kernel

function as a parameter. The optimization problem arises here as follows:

$$\min_{\{\beta_n\}_{n=0}^N} \sum_{i=1}^P \left[y_i - \beta_0 - \beta_1^T (\mathbf{x}_i - \mathbf{x})^T - \beta_2^T \text{vech} \{ (\mathbf{x}_i - \mathbf{x})(\mathbf{x}_i - \mathbf{x})^T \} - \dots \right]^2 \mathcal{K}(\mathbf{x}_i - \mathbf{x}, y_i - y), \quad (3.1)$$

where the data-adapted kernel function \mathcal{K} now depends on the spatial differences $(\mathbf{x}_i - \mathbf{x})$ as well as the local radiometric differences $(y_i - y)$. The rest of this chapter presents the selections of the adapted kernel (\mathcal{K}).

3.2.1 Bilateral Kernel Regression

A simple and intuitive choice of the \mathcal{K} is to use separate terms for penalizing the spatial differences between the position of interest \mathbf{x} and its nearby position $\{\mathbf{x}_i\}$, and the radiometric differences between the corresponding pixel value y and $\{y_i\}$:

$$\mathcal{K}(\mathbf{x}_i - \mathbf{x}, y_i - y) \equiv K_{\mathbf{H}_s}(\mathbf{x}_i - \mathbf{x}) K_{h_r}(y_i - y), \quad (3.2)$$

where \mathbf{H}_s is the spatial smoothing matrix defined as $\mathbf{H}_s = h_s \mathbf{I}$, and h_s and h_r are the spatial and radiometric smoothing parameters. We call this the *bilateral kernel*. However, the kernel has a weakness in that the radiometric value y at an arbitrary position \mathbf{x} is not available occasionally as is the case for interpolation problems. Hence we cannot compute the radiometric weight $K_{h_r}(y_i - y)$ directly. We may still use the radiometric kernel, but in such cases a *pilot* estimate will be needed first to estimate the y . When, in general, y at a arbitrary position \mathbf{x} does exist, the optimization problem with the kernel can be rewritten as:

$$\min_{\{\beta_n\}_{n=0}^N} \sum_{i=1}^P \left[y_i - \beta_0 - \beta_1^T (\mathbf{x}_i - \mathbf{x}_j)^T - \beta_2^T \text{vech} \{ (\mathbf{x}_i - \mathbf{x}_j)(\mathbf{x}_i - \mathbf{x}_j)^T \} - \dots \right]^2 \cdot K_{\mathbf{H}_s}(\mathbf{x}_i - \mathbf{x}_j) K_{h_r}(y_i - y_j), \quad (3.3)$$

which we call *Bilateral Kernel Regression*. Note that the regression now lost the interpolation ability. This can be better understood by studying the spacial case of $N = 0$, which results in a data-adapted version of the Nadaraya-Watson [13] estimator:

$$\hat{z}(\mathbf{x}_i) = \frac{\sum_{i=1}^P K_{\mathbf{H}_s}(\mathbf{x}_i - \mathbf{x}_j) K_{h_r}(y_i - y_j) y_i}{\sum_{i=1}^P K_{\mathbf{H}_s}(\mathbf{x}_i - \mathbf{x}_j) K_{h_r}(y_i - y_j)}. \quad (3.4)$$

Interestingly, this is nothing but the recently well-studied and popular *bilateral filter* [23, 24], both of whose kernels were chosen as Gaussian. In our framework, it is not required for us to pick the same kernel for both spatial and radiometric kernels. Of course, the higher order regressions ($N > 0$) are also available and they can have better performance than the bilateral filter (the zero-th order bilateral kernel regression (3.4)). As described above, we cannot apply this regression directly to interpolation problems, and the direct solution of (3.3) is limited to the denoising problem. Later in this chapter, this limitation can be overcome by using an initial estimate of y in an iterative set-up.

In any event, breaking \mathbf{K} into the spatial and radiometric kernels as utilized in the bilateral case weakens the estimation performance. A simple justification for this claim comes from studying the very noisy data sets, where the radiometric differences $(y_i - y_j)$'s tend to be large and as a result all radiometric weights are very close to zero, and effectively useless. Buades et al. gave this discussion in [41], and they proposed the *non-local means* algorithm to enhance denoising effect. However, the algorithm has also a limited scope of use: image denoising. The following subsection provides a solution to overcome this drawback of the bilateral kernel approach and the limited scope of use.

3.2.2 Steering Kernel Regression

The filtering procedure we proposed above takes the idea of the bilateral kernel one step further, based upon the earlier kernel regression framework. In particular, we observe that the effect of computing $K_{h_r}(y_i - y)$ in (3.2) is to implicitly measure a function of the local gradient estimated between neighboring pixel values, and to use this estimate to weigh the respective measurements. As an example, if a pixel is located near an edge, then pixels on the same side of the edge will have much stronger influence in the filtering. With this intuition in mind, we propose a two-step approach where first an initial analysis of the image local structure is carried out. In a second stage, this structure information is then used to adaptively “steer” the local kernel, resulting in elongated, elliptical contours spread along the directions of the local edge structure. With these locally adapted kernels, the image restoration and reconstruction are effected most strongly along the edges, rather than across them, resulting in strong preservation of detail in the final output. To be specific, we study an alternative choice of K with a joint spatial and radiometric kernel function

$$K(\mathbf{x}_i - \mathbf{x}, y_i - y) \equiv K_{\mathbf{H}_i^s}(\mathbf{x}_i - \mathbf{x}), \quad (3.5)$$

where, unlike the classic smoothing matrices (2.42), the smoothing matrices $\{\mathbf{H}_i^s\}_{i=1}^P$ are the data-adapted full matrices defined as

$$\mathbf{H}_i^s = h\mu_i \mathbf{C}_i^{-\frac{1}{2}}, \quad (3.6)$$

where $\{\mathbf{C}_i\}_{i=1}^P$ are (symmetric) covariance matrices based on the local gray values (and estimated from the image structure analysis as described below), in other words, all the \mathbf{C}_i ’s are implicitly the function of the given data set $\{y_i\}_{i=1}^P$. We call $K_{\mathbf{H}_i^s}(\cdot)$ the *steering kernel* and \mathbf{H}_i^s the *steering matrix* from now on. With such steering matrices, for example,

if we choose a Gaussian kernel, the steering kernel is mathematically represented as

$$K_{\mathbf{H}_i^s}(\mathbf{x}_i - \mathbf{x}) = \frac{\sqrt{\det(\mathbf{C}_i)}}{2\pi h^2 \mu_i^2} \exp \left\{ -\frac{(\mathbf{x}_i - \mathbf{x})^T \mathbf{C}_i (\mathbf{x}_i - \mathbf{x})}{2h^2 \mu_i^2} \right\}. \quad (3.7)$$

A good choice for \mathbf{C}_i will effectively spread the kernel function along the local edges as shown in Figure 3.1(b). It is worth noting that if we choose a large h in order to have a strong denoising effect, the undesirable blurring effect which would have resulted, is tempered around edges with an appropriate choice of $\{\mathbf{C}_i\}_{i=1}^P$. The method bears some resemblances to the *pre-whitened kernel density estimator* in [42, 28].

In the following subsections, two methods to analyze image structure and obtain the covariance matrices $\{\mathbf{C}_i\}_{i=1}^P$ are presented. One method is based on *pattern classification* [43], and the other is based on *local orientation estimate* [44].

3.2.2.1 Pattern Classification

One intuitive way of obtaining steering matrices $\{\mathbf{C}_i\}_{i=1}^P$ is to cluster measured data by their radiometric values. Suppose we have a clustering result as illustrated in Figure 3.2, and the i^{th} sample is now belonging to the cluster c_i , in which case the covariance matrix for the data is simply given by

$$\hat{\mathbf{C}}_i = \begin{bmatrix} \text{cov}(\chi_1, \chi_1) & \text{cov}(\chi_1, \chi_2) \\ \text{cov}(\chi_1, \chi_2) & \text{cov}(\chi_2, \chi_2) \end{bmatrix}^{-1}, \quad (3.8)$$

where

$$\chi_1 = [\cdots, x_{1j}, \cdots]^T, \quad \chi_2 = [\cdots, x_{2j}, \cdots]^T, \quad \mathbf{x}_j = [x_{1j}, x_{2j}]^T, \quad \mathbf{x}_j \in c_i. \quad (3.9)$$

The matrix tells us how the samples having similar radiometric values are distributed in the local region. In the following a classification method called the *agglomerative algorithm* [43] is reviewed and redesigned for obtaining the covariance matrices.

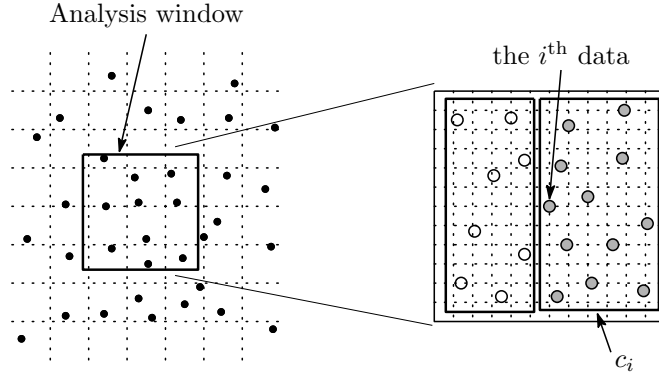


Figure 3.2: Schematic representation of an example of clustering.

Agglomerative algorithm is a well-known bottom-up clustering methods. In the beginning of the clustering process, each single sample is regarded as a cluster. Then we compute dissimilarities (distances) between every possible pair of the clusters, find a pair of clusters which has the smallest dissimilarity, and combine them into a new cluster. We repeat this procedure several times until the number of clusters reaches a predetermined value. The dissimilarities between pairs of clusters are measured with a *distance measure* and a *linkage method* [43]. The distance measure computes a dissimilarity between a sample from a cluster and a sample from another cluster, and linkage method is the way of which data in a cluster is used for computing the dissimilarity against another cluster.

The common distance measures for agglomerative algorithm are listed below,

$$\text{L1 distance} : d_{l_1}(\mathbf{v}_j, \mathbf{v}_k) = \|\mathbf{v}_j - \mathbf{v}_k\|_1 \quad (3.10)$$

$$\text{L2 distance} : d_{l_2}(\mathbf{v}_j, \mathbf{v}_k) = \|\mathbf{v}_j - \mathbf{v}_k\|_2 \quad (3.11)$$

$$\text{Euclidean distance} : d_{\text{eu}}(\mathbf{v}_j, \mathbf{v}_k) = \|\mathbf{v}_j - \mathbf{v}_k\|_2^2. \quad (3.12)$$

The vectors \mathbf{v} 's we have here are three dimensional vectors, since we want cluster measured

data with considering both spatial and radiometric values, defined as

$$\mathbf{v}_i = [x_{1i} \ x_{2i} \ y_i]^T, \quad (3.13)$$

where x_{1i} and x_{2i} are the coordinates of the i^{th} sample, and y_i is the radiometric value of the sample. Since, in certain cases, we would prefer to consider the spatial differences more strongly than radiometric differences, or vice versa, we may place some weights on them with a 3×3 weight matrix as

$$\mathbf{\Omega} = \begin{bmatrix} \sigma_s^2 & 0 & 0 \\ 0 & \sigma_s^2 & 0 \\ 0 & 0 & \sigma_r^2 \end{bmatrix}, \quad (3.14)$$

where σ_s and σ_r are spatial and radiometric weight coefficients, respectively. We define the weighted distance measures as follows:

$$\text{Weighted } l_1 \quad : \quad d_{WL1}(\mathbf{v}_j, \mathbf{v}_k) = \sigma_s^{-1}|x_{1j} - x_{1k}| + \sigma_s^{-1}|x_{2j} - x_{2k}| + \sigma_r^{-1}|y_j - y_k| \quad (3.15)$$

$$\text{Weighted } l_2 \quad : \quad d_{WL2}(\mathbf{v}_j, \mathbf{v}_k) = \sqrt{(\mathbf{v}_j - \mathbf{v}_k)^T \mathbf{\Omega}^{-1} (\mathbf{v}_j - \mathbf{v}_k)} \quad (3.16)$$

$$\text{Weighted Euclidean} \quad : \quad d_{WL2}(\mathbf{v}_j, \mathbf{v}_k) = (\mathbf{v}_j - \mathbf{v}_k)^T \mathbf{\Omega}^{-1} (\mathbf{v}_j - \mathbf{v}_k). \quad (3.17)$$

Using one of the above distance measures, a dissimilarity between a pair of clusters is calculated with the linkage methods, whose typical choices are

$$\text{single linkage} \quad : \quad D(c_1, c_2) = \min_{\mathbf{v}_j \in c_1, \mathbf{v}_k \in c_2} d(\mathbf{v}_j, \mathbf{v}_k) \quad (3.18)$$

$$\text{complete linkage} \quad : \quad D(c_1, c_2) = \max_{\mathbf{v}_j \in c_1, \mathbf{v}_k \in c_2} d(\mathbf{v}_j, \mathbf{v}_k) \quad (3.19)$$

$$\text{average linkage} \quad : \quad D(c_1, c_2) = \frac{1}{N_1 N_2} \sum_{\mathbf{v}_j \in c_1} \sum_{\mathbf{v}_k \in c_2} d(\mathbf{v}_j, \mathbf{v}_k) \quad (3.20)$$

$$\text{mean linkage} \quad : \quad D(c_1, c_2) = d \left(\frac{1}{N_1} \sum_{\mathbf{v}_j \in c_1}, \frac{1}{N_2} \sum_{\mathbf{v}_k \in c_2} \right), \quad (3.21)$$

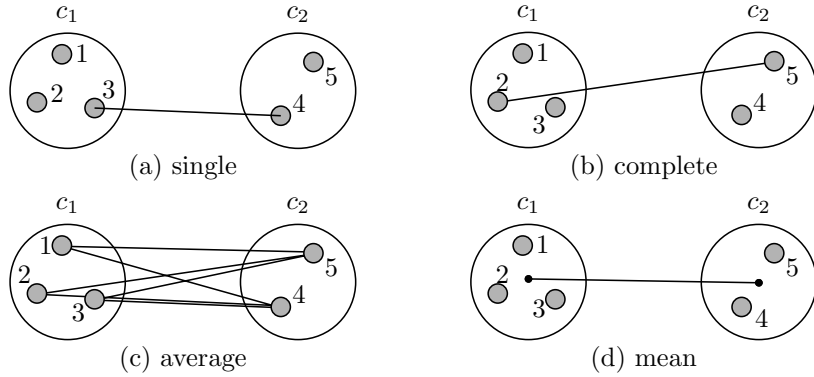


Figure 3.3: Schematic representation of typical linkage methods.

where N_1 and N_2 are the number of the data in the cluster c_1 and c_2 , respectively. Figure 3.3 is illustrating schematic representations of each linkage method.

3.2.2.2 Local Orientation Estimate

The local edge structure is related to the gradient covariance (or equivalently, the locally dominant orientation), where a naive estimate of this covariance matrix may be obtained as follows:

$$\hat{\mathbf{C}}_i \approx \begin{bmatrix} \sum_{\mathbf{x}_j \in w_i} z_{x_1}(\mathbf{x}_j) z_{x_1}(\mathbf{x}_j) & \sum_{\mathbf{x}_j \in w_i} z_{x_1}(\mathbf{x}_j) z_{x_2}(\mathbf{x}_j) \\ \sum_{\mathbf{x}_j \in w_i} z_{x_1}(\mathbf{x}_j) z_{x_2}(\mathbf{x}_j) & \sum_{\mathbf{x}_j \in w_i} z_{x_2}(\mathbf{x}_j) z_{x_2}(\mathbf{x}_j) \end{bmatrix} \quad (3.22)$$

where $z_{x_1}(\cdot)$ and $z_{x_2}(\cdot)$ are the first derivatives along x_1 and x_2 directions and w_i is a local analysis window around the position of interest. The dominant local orientation of the gradients is then related to the eigenvectors of this estimated matrix. While this approach (which is essentially a local principal components method) is simple and has nice tolerance to noise, the resulting estimate of the covariance may in general be rank deficient or unstable, and therefore care must be taken not to take the inverse of the estimate directly in this

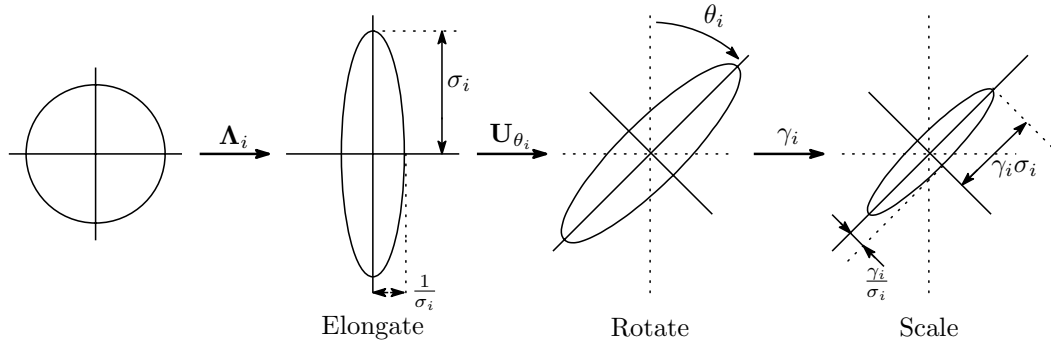


Figure 3.4: Schematic representation illustrating the effects of the steering matrix and its component ($\mathbf{C}_i = \gamma_i \mathbf{U}_{\theta_i} \mathbf{\Lambda}_{\sigma_i} \mathbf{U}_{\theta_i}^T$) on the size and shape of the regression kernel .

case. In such case, a diagonal loading or regularization methods can be used to obtain stable estimates of the covariance matrix. In [44], Feng *et al* proposed an effective *multiscale* technique for estimating local orientations, which fits the requirements of this problem nicely. Informed by the above, this thesis takes a parametric approach to the design of the steering matrix.

In order to have a more convenient form of the covariance matrix, we decompose the covariance matrix into three components as follows:

$$\mathbf{C}_i = \gamma_i \mathbf{U}_{\theta_i} \mathbf{\Lambda}_i \mathbf{U}_{\theta_i}^T, \quad \mathbf{U}_{\theta_i} = \begin{bmatrix} \cos \theta_i & \sin \theta_i \\ -\sin \theta_i & \cos \theta_i \end{bmatrix}, \quad \mathbf{\Lambda}_i = \begin{bmatrix} \rho_i & 0 \\ 0 & \rho_i^{-1} \end{bmatrix}, \quad (3.23)$$

where \mathbf{U}_{θ_i} is a rotation matrix and $\mathbf{\Lambda}_i$ is the elongation matrix. Now the covariance matrix is given by the three parameters γ_i , θ_i , and ρ_i , which are the scaling, rotation, and elongation parameters, respectively. Figure 3.4 schematically explains how these parameters affect the spreading of kernels. First, the circular kernel is elongated by the elongation matrix $\mathbf{\Lambda}_i$, and its semi-minor axis and semi-major axis are given by ρ_i . Second, the elongated kernel is rotated by the rotation matrix \mathbf{U}_{θ_i} . Finally, the kernel is scaled by the scaling parameter γ_i .

This thesis defines the scaling, elongation, and rotation parameters as follows. Following the orientation estimation method in [44], the dominant orientation of the local gradient field is the singular vector corresponding to the smallest (non-zero) singular value of the local gradient matrix arranged in the following form

$$\mathbf{G}_i = \begin{bmatrix} \vdots & \vdots \\ z_{x_1}(\mathbf{x}_j) & z_{x_2}(\mathbf{x}_j) \\ \vdots & \vdots \end{bmatrix} = \mathbf{U}_i \mathbf{S}_i \mathbf{V}_i^T, \quad \mathbf{x} \in w_i, \quad (3.24)$$

where $\mathbf{U}_i \mathbf{S}_i \mathbf{V}_i^T$ is the truncated singular value decomposition of \mathbf{G}_i . \mathbf{S}_i is a diagonal 2×2 matrix representing the energy in the dominant directions. Then, the second column of the orthogonal 2×2 matrix \mathbf{V}_i , $\mathbf{v}_2 = [\nu_1, \nu_2]^T$, gives the dominant orientation angle θ_i :

$$\theta_i = \arctan\left(\frac{\nu_1}{\nu_2}\right). \quad (3.25)$$

That is, the singular vector corresponding to the smallest non-zero singular value of \mathbf{G}_i represents the dominant orientation of the local gradient field. The elongation parameter ρ_i can be selected corresponding to the energy of the dominant gradient direction:

$$\rho_i = \frac{s_1 + \lambda'}{s_2 + \lambda'}, \quad \lambda' \geq 0, \quad (3.26)$$

where λ' is a regularization parameter for the kernel elongation, which dampens the effect of the noise, and restricts the denominator away from becoming zero. The intuition behind (3.26) is to keep the shape of the kernel circular in flat area ($s_1 \approx s_2 \approx 0$), and elongate it near edge areas ($s_1 \gg s_2$). Finally, the scaling parameter γ_i is defined by

$$\gamma_i = \left(\frac{s_1 s_2 + \lambda''}{M}\right)^{\frac{1}{2}}, \quad (3.27)$$

where λ'' is again a regularization parameter, which dampens the effect of the noise and keeps γ_i from becoming zero; and M is the number of samples in the local analysis window.

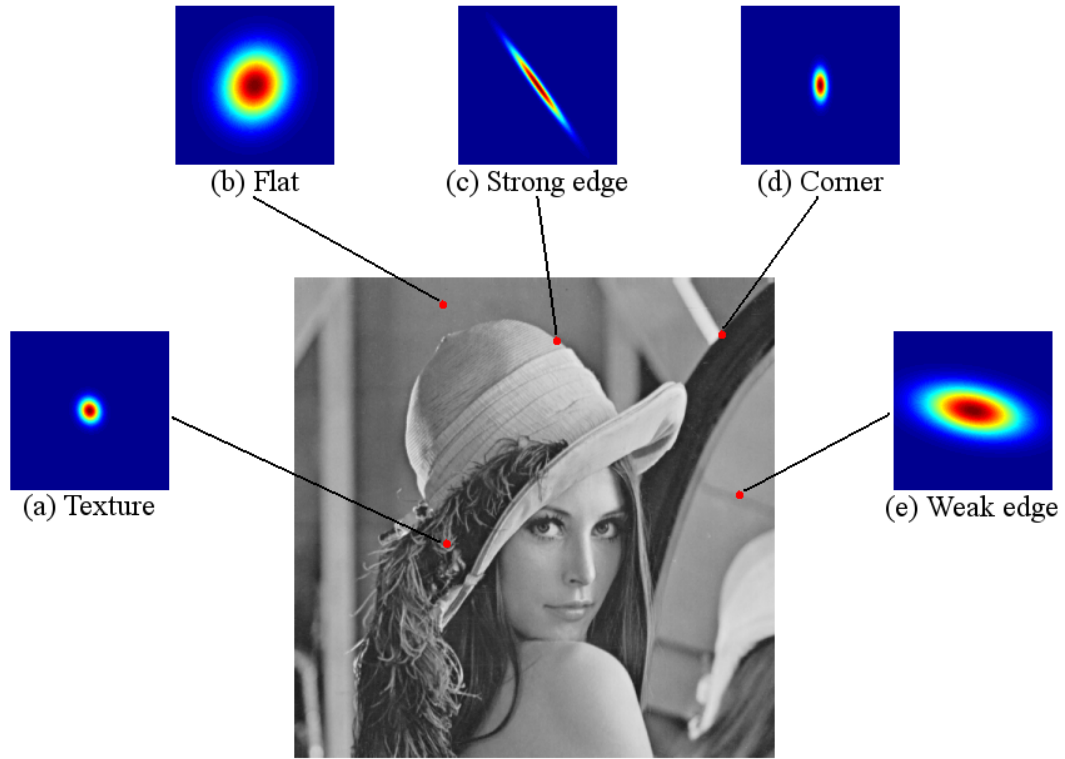


Figure 3.5: Footprint examples of steering kernels with covariance matrices $\{\mathbf{C}_i\}$ given by the local orientation estimate (3.23) at a variety of image structures.

The intuition behind (3.27) is that, to reduce noise effects while producing sharp images, large footprints are preferred in the flat (smooth) areas and smaller ones in the textured areas. Note that the local gradients, as well as the eigenvalues (or singular values) of the covariance matrix \mathbf{C}_i , are smaller in the flat (low-frequency) areas than the textured (high-frequency) areas. As the scaling parameter γ_i is given by the geometric mean of the singular values of $\hat{\mathbf{C}}_i$ in (3.27), γ_i makes the steering kernel area large in the flat areas, and small in the textured areas. Figure 3.5 illustrates such behaviors of steering kernels at a variety of image structures of Lena.

While it appears that the choice of three parameters in the above discussion is

purely ad-hoc, we direct the interested reader to a more careful statistical analysis of the distributional properties of the singular values (s_j) in [44, 45, 46]. The particular selections for these parameters are directly motivated by this earlier work. However, to maintain focus and conserve space, we elected not to include such details.

3.3 Iterative Steering Kernel Regression

3.3.1 Filtering Algorithm

The estimated smoothing matrices of the steering kernel regression method are data dependent, and consequently sensitive to the noise in the input image. As we experimentally demonstrate in the next section, steering kernel regression is most effective when an iterative regression/denoising procedure is used to exploit the output (less noisy) image of each iteration to estimate the radiometric terms of the kernel in the next iteration. A block diagram representation of this method is shown in Figure 3.6. In this diagram, the data set is used to create the initial (dense) estimate of the interpolated output image (Figure 3.6(a)). In the next iteration, the reconstructed (less noisy) image is used to recalculate a more reliable estimate of the gradient (Figure 3.6(b)), and this process continues for a few more iterations. While we do not provide an analysis of the convergence properties of this proposed iterative procedure, we note that while increasing the number of iterations reduced the variance of the estimate, it also leads to increased bias (which manifests as blurriness). Therefore, in a few (typically around 5) iterations, a minimum mean-squared estimate is obtained (an example will be shown below). A future line of work will analyze the derivation of an effective stopping criterion and a careful study of convergence properties from first principles.

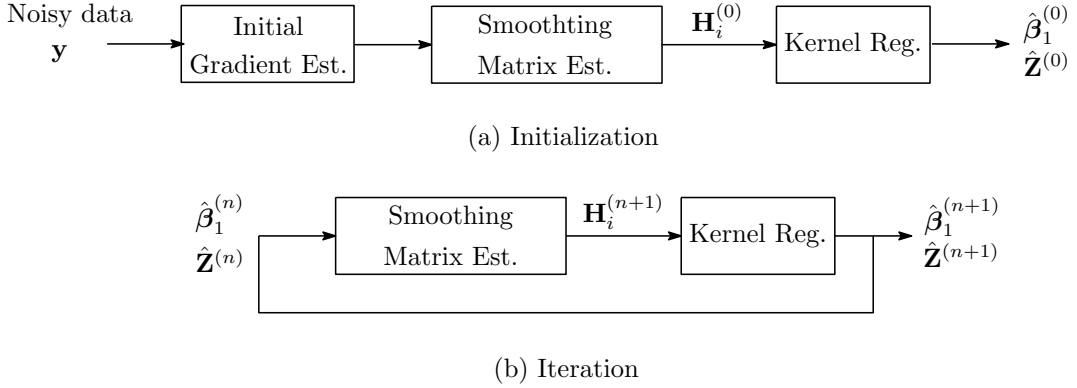


Figure 3.6: Block diagram representation of the iterative adaptive regression.

It is worth pointing out that the iterative regression method has the luxury of using directly estimated gradients. Note that the discrete gradients used in (3.24) are usually approximated by convolving a bandpass filter with the image. However, comparison of (2.16) and (2.19) shows that the vector β_1 is the direct estimate of the image gradients. Indeed, the direct estimation of the gradient vector is more reliable but at the same time computationally more expensive. In Appendix B, computation of β_1 , directly in the regression context, is presented.

3.3.2 Performance Analysis

In this section, we illustrate some properties and performance of iterative steering kernel regression with a simple image denoising example. Adding white Gaussian noise with standard deviation 25 to Figure 3.7(a) generates the noisy image shown in Figure 3.7(b). The denoising results by the iterative steering kernel regression method with $h = 2.75$ are illustrated in Figures 3.7(c)-(f). As seen in these results, the mean square error (MSE) is minimized after 3 iterations. However, too many iterations result in the blurry image. As we will illustrate shortly, this blur is caused by increasing bias in the estimate. On the other

hand, the variance is reduced with each iteration. It is known (q.v. [16]) that the mean square error is expressed as

$$\text{MSE} [\hat{z}(\mathbf{x}, h)] = \text{Bias}^2[\hat{z}(\mathbf{x}, h)] + \text{Var} [\hat{z}(\mathbf{x}, h)], \quad (3.28)$$

and the graph in Figure 3.8 illustrates the behavior of MSE, bias, and variance, which are yielded by Monte Carlo simulations (100 denoising experiments per pixel by adding white Gaussian noise with variance 25 and different noise seeds).

While in this case, choosing $h = 2.75$, with 3 iterations yielded the best estimate, the necessary number of iterations is different for different h . Figure 3.10, Figure 3.11, and Figure 3.12 illustrate the behavior of MSE, bias, and variance, respectively, and Table 3.1 shows the best estimates with for four different global smoothing parameters. Interestingly, the best MSE's are nearly the same even though the smoothing parameters are not. However the ratio of bias and variance is different in each case. The larger the smoothing parameter (h), the fewer iterations are necessary to reach the minimum MSE. With a larger h , however, the estimated image has larger bias, which means the resulting image is more blurry. Figure 3.9 shows that two denoised results with a smaller $h(= 2.25)$ and a larger $h(= 3.0)$. As Table 3.1 tells us, with the larger h , the estimated image (Figure 3.9(b)) is more blurry than Figure 3.9(a), nonetheless their MSE are quite close. In general, a smaller h and more iterations give us a visually superior result.

3.4 Summary

This chapter presented data-adapted (non-linear) kernel regression with two new approaches: the bilateral kernel and the steering kernel, for image processing and reconstruction based on kernel regression. Moreover, a novel iterative filtering algorithm (Figure 3.6)

h	2.25	2.50	2.75	3.00
it #	9	5	3	2
MSE	101.35	98.87	98.33	98.93
Bias ²	46.70	49.22	51.29	54.82
Variance	54.65	49.65	47.04	44.11

Table 3.1: The best estimation in mean square error by iterative steering kernel regression with different global smoothing parameters.

and its performance are also presented. Using the data-adapted kernel regression method with the iterative filtering algorithm, estimated images will have superior quality, which will be demonstrated with real data sets in Chapter 5.

In the next chapter, we will discuss the application of ideas presented so far to motion estimation. As reviewed in Section 1.2, to reconstruct a high quality image, we need to have motions as accurately as possible. Surprisingly, the kernel regression method has a power to improve the estimation performance of the current state of the art motion estimation methods which use optical flow in a multi-resolution context.

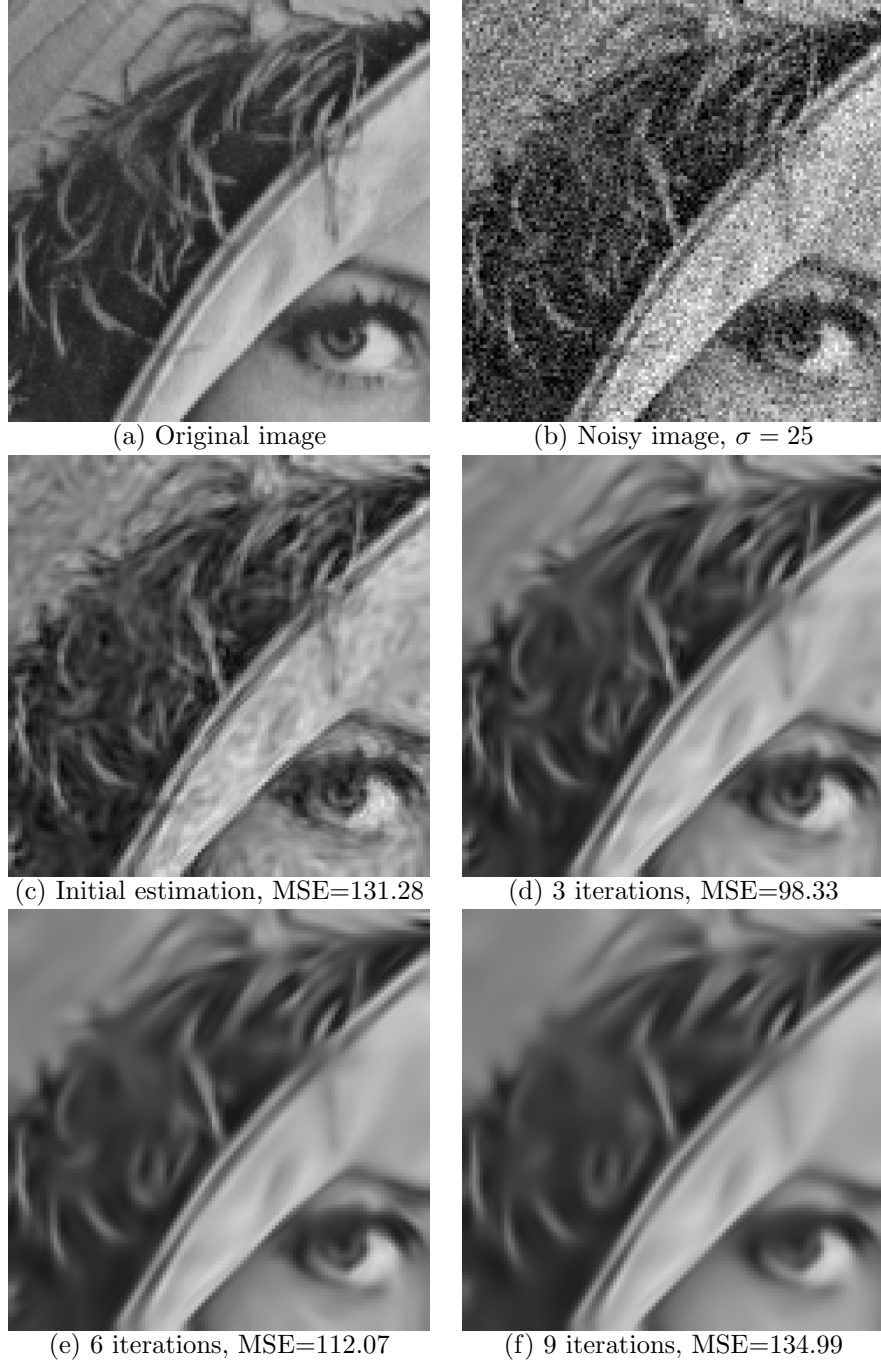


Figure 3.7: A denoising experiment by iterative steering kernel regression.

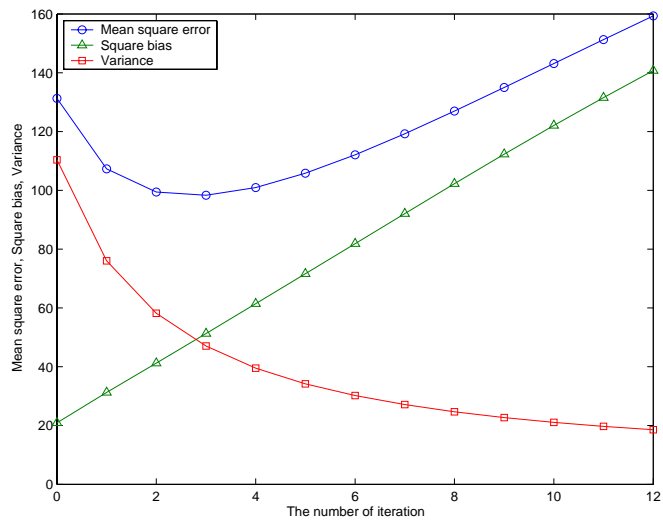


Figure 3.8: The analysis of mean square error, bias, and variance.

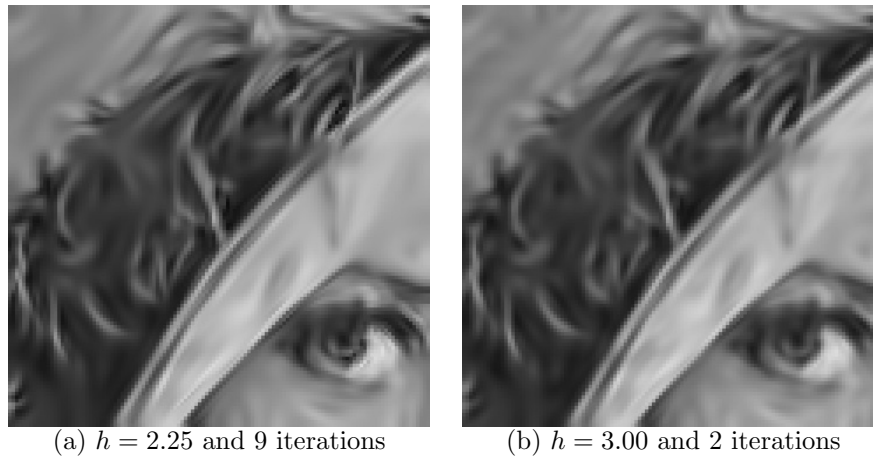


Figure 3.9: The best estimation in mean square error with two different global smoothing parameters.

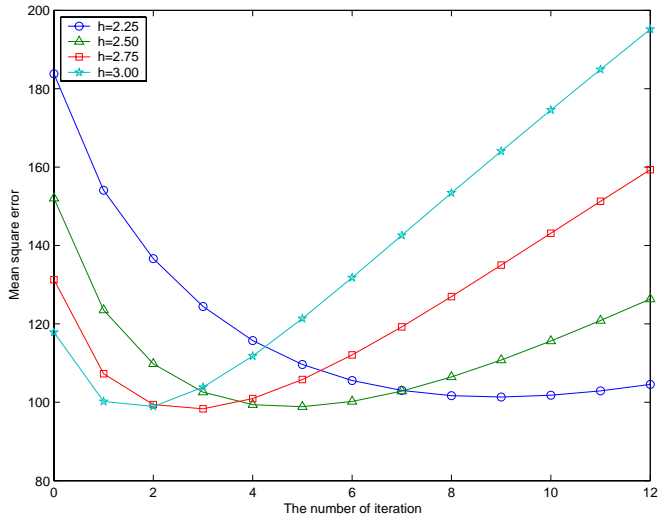


Figure 3.10: Mean square error with different global smoothing parameters.

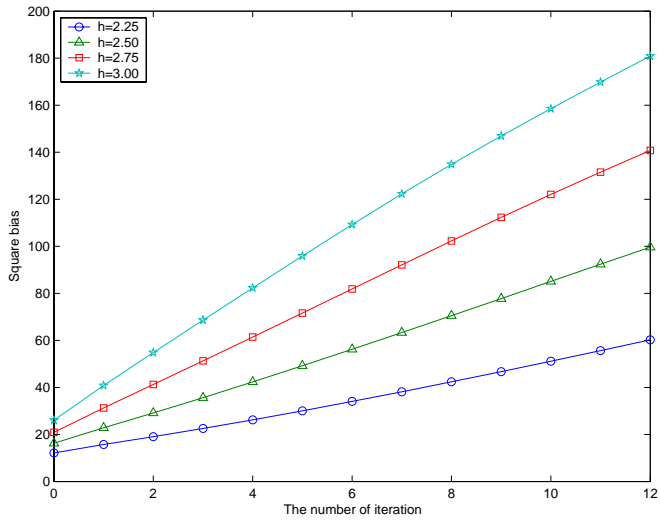


Figure 3.11: Bias with different global smoothing parameters.

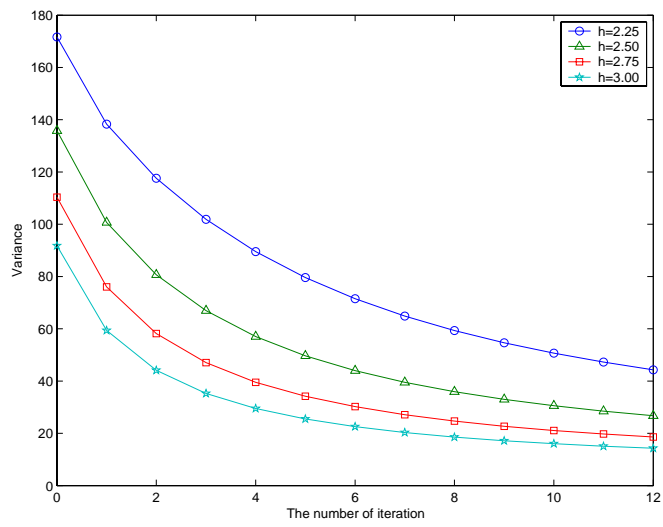


Figure 3.12: Variance with different global smoothing parameters.

Chapter 4

Motion Estimation

4.1 Introduction

Motion estimation is one of the most important issues in image reconstruction, or super-resolution. Once the motions are available, we know where measured data must be located. After that we place all data onto a finer resolution grid, and interpolate them to have a high quality image; a concept we reviewed in Section 1.2. In this chapter, we review a widely-used motion estimation algorithm first (optical flow + multiscale) and then will see how kernel regression makes the performance better.

Before going through the review of motion estimation, let's remark on what factors affect the performance. Motion estimation based on optical flow equations [8] is severely influenced by measurement noise since the equations are built up on image gradients. And when computing the gradients, we tend to amplify the noise. Moreover, computing correct gradients is not so easy. Using *sobel gradient operator* [10], the estimated gradients have errors [47], and such errors cause motion estimation errors. Hence, estimating gradients

itself is an important problem, and fortunately we can use higher order kernel regression as a gradient estimator. The second order regression is a preferable choice to estimate the first derivatives since the second derivative term β_2 implicitly regularizes the first derivative term β_1 . There is another problem that makes motion estimation difficult. Using multiscale algorithm to cope with large motions, we propagate a motion estimated in coarse resolution fields to fine resolution fields. This propagation requires that we warp images by some method, such as cubic spline interpolation. This image warping is, therefore, also affecting the performance of motion estimation due to the distortion introduced by the image warping methods. To summarize, there are three factors which complicate motion estimation. Namely: *measurement noise*, *gradient errors*, and *image warping*. Kernel regression is an excellent tool to deal with these problems and will give us denoised and warped gradients with a high quality.

We will deal with only *translational motion* [7] in this thesis. However the algorithm is, of course, applicable to more complex parametric motion estimation. Translation is the simplest motion model, in which we assume that all motions at every pixel are same, and consequently there are two unknown motion parameters in the vertical and horizontal directions.

4.2 Accurate Motion Estimation

4.2.1 Motion Estimator Based on Optical Flow Equations

In the first instance, we review briefly the motion estimation based on optical flow equations. Suppose $y(\mathbf{x}, t)$ is the pixel value at $\mathbf{x} = [x_1, x_2]^T$ and time t . A point in a frame at \mathbf{x} moves to $\mathbf{x} + \mathbf{d}$ at the time $t + d_t$, where $\mathbf{d} = [d_{x_1}, d_{x_2}]^T$. Assuming constancy in the

pixel's brightness, we can write the following equation:

$$y(\mathbf{x} + \mathbf{d}, t + d_t) = y(\mathbf{x}, t), \quad (4.1)$$

where d_{x_1} , d_{x_2} and d_t are assumed small. If these differential values are small enough to neglect the higher order terms of a Taylor expansion, we have:

$$y(\mathbf{x} + \mathbf{d}, t + d_t) \approx y(\mathbf{x}, t) + \frac{\partial y}{\partial x_1} d_{x_1} + \frac{\partial y}{\partial x_2} d_{x_2} + \frac{\partial y}{\partial t} d_t. \quad (4.2)$$

By comparing (4.1) with (4.2), we obtain

$$\frac{\partial y}{\partial x_1} d_{x_1} + \frac{\partial y}{\partial x_2} d_{x_2} + \frac{\partial y}{\partial t} d_t = 0. \quad (4.3)$$

Dividing both sides by d_t , we arrive at

$$\frac{\partial y}{\partial x_1} v_{x_1} + \frac{\partial y}{\partial x_2} v_{x_2} + \frac{\partial y}{\partial t} = 0. \quad (4.4)$$

This is the optical flow equation for a point \mathbf{x} . Assuming constant v_{x_1} , v_{x_2} , We have as many optical flow equations as the number of pixels of a frame, while the number of unknown parameters is only two; namely v_{x_1} and v_{x_2} . Therefore, motion estimation in this case is always an overdetermined problem. While this is encouraging, due to measurement noise and gradient errors, motion estimation can still be unstable.

Suppose we have a pair of frames $\#n$ and $\#n + 1$. The motion from the frame $\#n$ to $\#n + 1$ we call the *forward motion*. Analogously, from $\#n + 1$ to $\#n$, we have the *backward motion* in the opposite direction. Figure 4.1 indicates the forward and backward motion schematically. The magnitude of the (estimated) forward and backward motions should be the same, but the directions are opposite. Using this property, we construct the optical flow constraint. The optical flow equations of the forward motion between the n^{th} and $(n + 1)^{\text{th}}$ frames can be expressed in the vector form as

$$\underline{\mathbf{Y}}_{x_1}^{(n)} v_{x_1} + \underline{\mathbf{Y}}_{x_2}^{(n)} v_{x_2} + \underline{\mathbf{Y}}_t^{(n)} = \mathbf{0}, \quad (4.5)$$

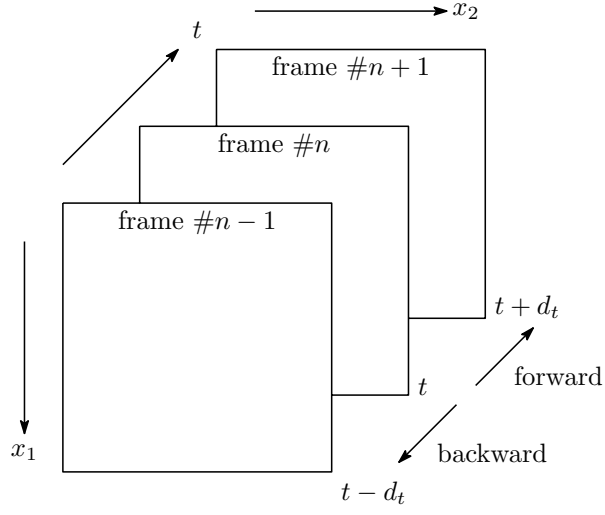


Figure 4.1: The forward and backward motion.

where the underline is the operator lexicographically ordering the elements of a matrix, and

$$\mathbf{Y}_{x_1}^{(n)} = \frac{\partial \mathbf{Y}_n}{\partial x_1}, \quad \mathbf{Y}_{x_2}^{(n)} = \frac{\partial \mathbf{Y}_n}{\partial x_2}, \quad \mathbf{Y}_t^{(n)} = \frac{\partial \mathbf{Y}_n}{\partial t} \approx \mathbf{Y}_n - \mathbf{Y}_{n+1}. \quad (4.6)$$

For the backward motion, we have

$$\underline{\mathbf{Y}}_{x_1}^{(n+1)} v_{x_1} + \underline{\mathbf{Y}}_{x_2}^{(n+1)} v_{x_2} - \underline{\mathbf{Y}}_t^{(n)} = \mathbf{0}. \quad (4.7)$$

By combining (4.5) and (4.7)

$$\begin{bmatrix} \underline{\mathbf{Y}}_{x_1}^{(n)} \\ \underline{\mathbf{Y}}_{x_1}^{(n+1)} \end{bmatrix} v_{x_1} + \begin{bmatrix} \underline{\mathbf{Y}}_{x_2}^{(n)} \\ \underline{\mathbf{Y}}_{x_2}^{(n+1)} \end{bmatrix} v_{x_2} + \begin{bmatrix} \underline{\mathbf{Y}}_t^{(n)} \\ -\underline{\mathbf{Y}}_t^{(n)} \end{bmatrix} = \mathbf{0}. \quad (4.8)$$

Thus by incorporating this symmetry constraint, the number of optical flow equation is doubled now. This idea can be applicable in any motion models based on optical flow equations, and the result is more stable. For convenience let us rewrite (4.8) as

$$\underline{\mathbf{J}}_{x_1} v_{x_1} + \underline{\mathbf{J}}_{x_2} v_{x_2} + \underline{\mathbf{J}}_t = \mathbf{0}, \quad (4.9)$$

$$\Rightarrow C(\mathbf{v}) \equiv \mathbb{J}\mathbf{v} + \underline{\mathbf{J}}_t = \mathbf{0}, \quad (4.10)$$

where $\mathbb{J} = [\mathbf{J}_{x_1} \ \mathbf{J}_{x_2}]$ and $\mathbf{v} = [v_{x_1} \ v_{x_2}]^T$ is the motion vector. We call $C(\mathbf{v})$ the *symmetric optical flow constraint* from now on.

Now we derive our translational motion estimator based on the optical flow constraint (4.10). Least squares estimator is a widely-used choice and the estimator is written as

$$\hat{\mathbf{v}} = \arg \min_{\mathbf{v}} \left\| \mathbb{J}\mathbf{v} + \mathbf{J}_t \right\|_2^2 = \arg \min_{\mathbf{v}} \left(\mathbb{J}\mathbf{v} + \mathbf{J}_t \right)^T \left(\mathbb{J}\mathbf{v} + \mathbf{J}_t \right), \quad (4.11)$$

$$= -(\mathbb{J}^T \mathbb{J})^{-1} \mathbb{J}^T \mathbf{J}_t. \quad (4.12)$$

However this estimator does not work well if the motion is large, we derived it under the assumption that motions are small. To overcome this drawback of the estimator, multiscale motion estimation are currently widely used (q.v. [48]). In the next section, we review it.

4.2.2 Multiscale Motion Estimation

For large motions, the approximation of (4.2) becomes inaccurate and inconsistent. In order to overcome this difficulty, we construct pyramids as illustrated in Figure 4.2, each scale of which is obtained by blurring with a low-pass filter (preferably Gaussian) and downsampling with the factor of 2 for both vertical and horizontal directions. First, we estimate the motion between the anchor and target frame in the top scale since the motion is diminished in that scale, and hence the approximation of (4.2) works well. Now we have a rough motion vector. After that we go down to one-lower scale and propagate the rough motion to the scale. In other words, we warp (shift) the anchor or target image at that scale, so that the motion between the two frames becomes small. Then we perform motion estimation (4.12) again on that scale. We repeat this until arriving at the bottom scale. In

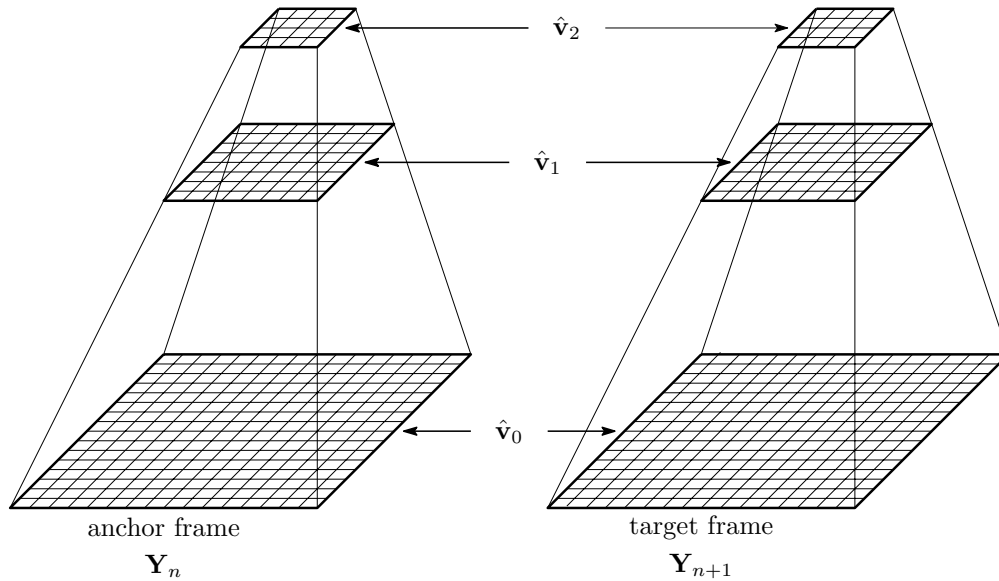


Figure 4.2: Multiscale motion estimation

this way, the final motion vector is given by

$$\hat{\mathbf{v}} = \sum_{l=0}^L 2^l \hat{\mathbf{v}}_l, \quad (4.13)$$

where L is the number of scales.

Using the multiscale motion estimation as mentioned above, we can deal with large motions. However, in order to estimate motions more accurately in each scale, we perform motion estimate iteratively several times in the same scale. The algorithm is simple; repeating motion estimation and image warping at the same scale. In that way, the motion to be estimated between anchor and target frames are small, and consequently the approximation (4.2) becomes more precise. Figure 4.3 illustrates the block diagram of the accurate motion estimation in a scale. As the number of iterations increases, the estimated motion $\hat{\mathbf{v}}$ between anchor and warped target are smaller. We put μ (in Figure 4.3) as a damping factor to make the estimation process stable, and it takes a value of $0 < \mu \leq 1.0$. We do the iteration

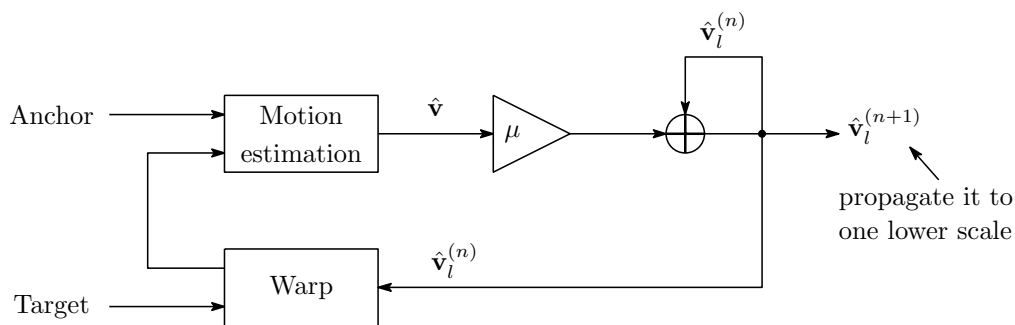


Figure 4.3: The block diagram of accurate motion estimation on a scale.

until the motion vector converges¹, put it differently, until \hat{v} becomes close to $\mathbf{0}$.

4.3 Image Warping

If the elements of the motions were integer number, it would be very easy for us to warp images, since we could just shift the pixel to be neighboring pixels. However we need a motion with sub-pixel accuracy, and this demands precise image warping. Well-known image warping techniques are *bilinear* and *cubic spline interpolation*. As an attractive alternative, we present a new warping technique, based on kernel regression. Interestingly, kernel regression can be an image warping tool, and it has great possibility, since the regression estimates denoised, less inconsistent, warped derivatives directly. In the next section, the performance analysis with different warping techniques are demonstrated.

¹It hopefully will converge. There is no guarantee. This issue must be investigated in the future work.

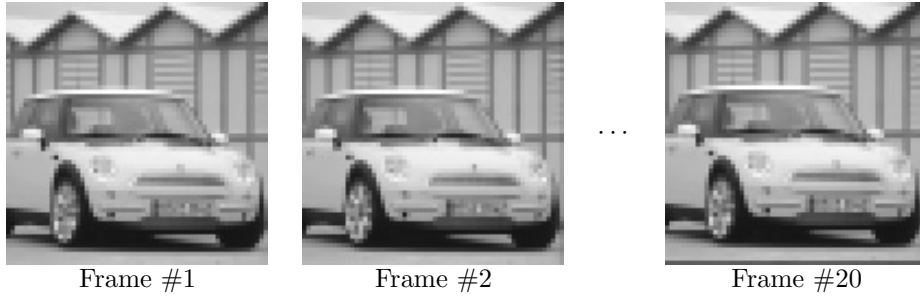


Figure 4.4: A simulated sequence.

4.4 Simulations

This section examines the performance of motion estimation. Using the motion estimation algorithm of Figure 4.3 with some different warping methods: (1)linear interpolation², (2)cubic interpolation³, (3)classic kernel regression ($N = 2$ and $h = 0.7$ with Gaussian kernel), we illustrate which method is better using noisy sequences. The noisy sequence⁴ is generated by adding white Gaussian noise with a variety of standard deviations to the simulated sequence shown in Figure 4.4. We generated the simulated sequence by the following procedures: (1) take the convolution the original high resolution image (1200×1200) with a 5×5 Gaussian kernel with variance 1.5, (2) randomly shift (integer shift) the blurry image to the vertical and horizontal directions (translational motion), (3) downsample the shifted image with factor 20 for both the vertical and horizontal directions (4) do the procedure (1)-(3) 20 times. The experimental result (100 times Monte Carlo simulations) is shown in Figure 4.5. The performance of the multiscale optical flow motion estimations with linear and cubic warping are very close to each other. On the other hand, the motion estimation with classic kernel regression yields us more accurate results.

²MATLAB's function "interp2" with the 'linear' option.

³MATLAB's function "interp2" with the 'cubic' option.

⁴The corresponding signal to noise ratio is 9[dB] when the standard deviation is 20.

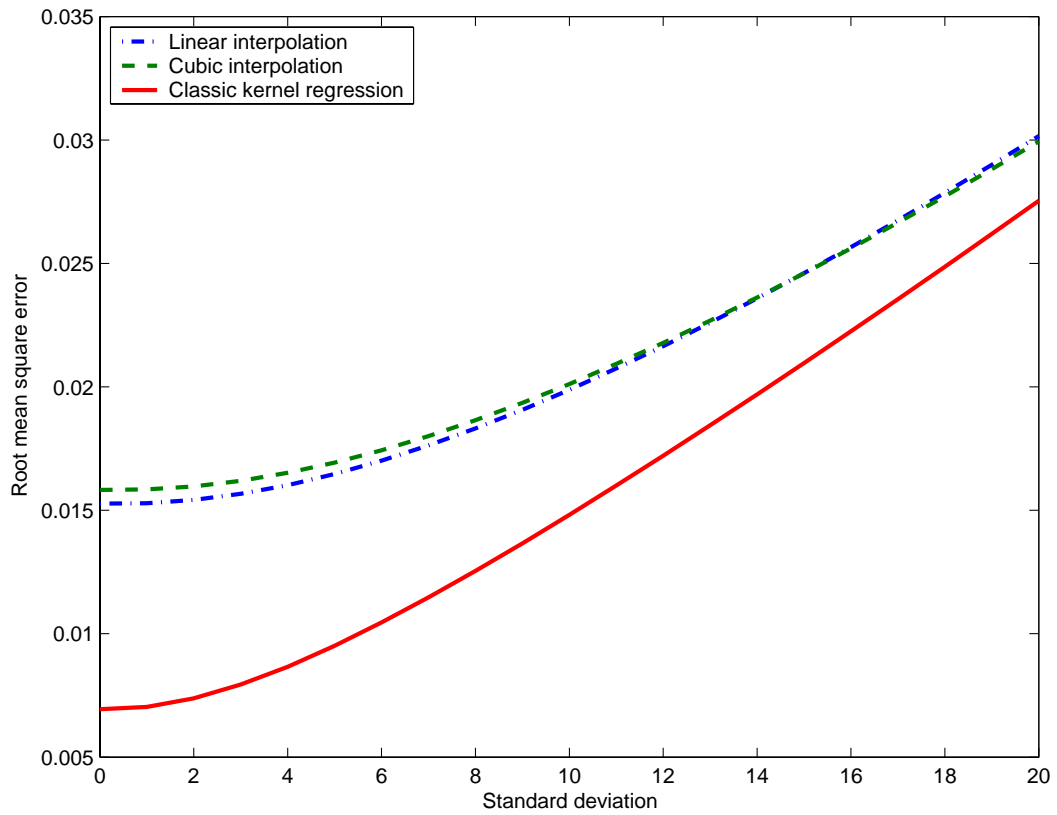


Figure 4.5: The performance analysis of motion estimations with different warping methods.

4.5 Summary

In this chapter, we investigated accurate motion estimation, and showed that kernel regression has great potential for use as image warping for motion estimation. The simulations demonstrated the performance improvements.

Chapter 5

Demonstration and Conclusion

5.1 Introduction

In this chapter, we demonstrate how suitable the kernel regression technique is for image processing and reconstruction. To show the ability of the proposed algorithm in Chapter 3, we present three different applications: denoising, interpolation, and super-resolution.

5.2 Image Denoising

In the first set of experiments, we compare the performance of several denoising techniques. We set up a controlled simulated experiment by adding white Gaussian noise with standard deviation (STD) of $\sigma = 25$ to the Lena image shown in Figure 5.1(a). The resulting noisy image with PSNR¹ of 20.17[dB], is shown in Figure 5.1(b). This noisy image

¹Peak Signal to Noisy Ratio is defined as $20 \log_{10}\left(\frac{255}{\text{RMSE}}\right)$.

is then denoised by the spline smoother² of (2.13) with³ $\lambda = 0.43$, result of which is shown in Figure 5.1(c) (zoomed in Figure 5.2(a)). The result of applying the bilateral filter (3.4) with $h_s = 1.5$ and $h_r = 7.4$ is shown in Figure 5.1(d) (zoomed in Figure 5.2(b)). For the sake of comparison, we have included the result of applying the recent wavelet based denoising method⁴ of [49] in Figure 5.1(e) (zoomed in Figure 5.2(c)). Finally, Figure 5.1(f) (zoomed in Figure 5.2(d)) shows the result of applying the iterative steering kernel regression of Section 3.2.2 ($N = 2$, $h = 2.4$, and 7 iterations). The RMSE values of the reconstructed images of Figure 5.1(b)-(f) are 25.0, 8.91, 8.65, 6.64, and 6.66, respectively.

We set up a second controlled simulated experiment by adding JPEG compression artifacts to the uncompressed image of Figure 5.3(a). The JPEG image was constructed by using MATLAB JPEG compression routine with a quality parameter equal to 10. This compressed image with a RMSE value equal to 9.76 is illustrated in Figure 5.3(b). We applied several denoising methods (similar to the ones used in the previous experiment) to acquire higher quality estimates. The results of applying the spline smoother with $\lambda = 0.11$, bilateral filter (3.4) with $h_s = 2.0$ and $h_r = 4.1$, wavelet [49], and the iterative steering kernel regression ($N = 2$, $h = 2.0$ and 3 iterations) are given in Figure 5.3(c)-(f), respectively. The RMSE values of the reconstructed images of Figure 5.3(c)-(f) are 9.05, 8.52, 8.80, and 8.48, respectively.

In the third denoising experiment, we applied several denoising techniques on the color image shown in Figure 5.4(a), which is corrupted by real film grain noise and scanning process noise. To produce better color estimates, following [50], first we transferred this RGB image to the **YCrCb** representation. Then we applied several denoising techniques (similar

²We used MATLAB's spline smoother function "*csaps*", for this and other spline smoother experiments.

³The criteria for parameter selection in this example (and other examples discussed in this thesis) was to choose parameters which produce visually most appealing results.

⁴In this experiment, we used the code (with parameters suggested for this experiment) provided by the author of [49] available at <http://decsai.ugr.es/~javier/denoise/index.html>.

to the ones in the previous two experiments) on each channel (the luminance component \mathbf{Y} , and the chrominance components \mathbf{Cr} and \mathbf{Cb}), separately. The results of applying Wavelet [49], and bilateral filter (3.4) ($h_s = 2.0$ and $h_r = 3.5$ for all the channels), and the iterative steering kernel regression ($N = 2$, $h = 2.0$, and 3 iterations) are given in Figures 5.4(b)-(d), respectively. Figures 5.4(e)-(g) show the absolute values of the residuals in the \mathbf{Y} channel. It can be seen that the proposed steering kernel method produces the most noise-like residuals.

5.3 Image Interpolation

In the forth experiment, we downsampled the Lena image of Figure 5.1(a) (zoomed in Figure 5.6(a)) by a factor of 3 in each direction. The resulting aliased image is shown in Figure 5.5(a). We compare the performance of different techniques, for upscaling this (regularly sampled) image back to its original size (with the resolution enhancement factor of 3 in each direction). Figure 5.5(b) (zoomed in Figure 5.6(b)) shows the result of applying the spline smoother with $\lambda = 0.0006$. Figure 5.5(c) (zoomed in Figure 5.6(c)) is the result of using the classic kernel regression ($h = 1.75$). Figure 5.5(d) (zoomed in Figure 5.6(d)) shows the result of implementing the bilateral kernel regression of Section 3.2.1 ($N = 0$, $h_s = 1.75$ and $h_r = 3.0$). Figures 5.5(e) and (f) (zoomed in Figures 5.6(e) and (f), respectively) are the results of the iterative steering kernel regression ($N = 0$, $h = 1.0$ and no iterations) and ($N = 2$, $h = 1.25$ and no iterations) of Section 3.2.2. The RMSE values of the reconstructed images of Figures 5.5(b)-(f) are 7.92, 7.96, 8.07, 8.03, and 7.42, respectively.

The fifth experiment is a controlled simulated regression of an irregularly sampled image. We randomly deleted 85% of the pixels in the Lena image of Figure 5.1(a), creating the sparse image of Figure 5.7(a). To fill the missing values, first we implemented the

Delaunay-spline smoother⁵ with $\lambda = 0.087$ to fill the missing values, the result of which is shown in Figure 5.7(b), with some clear artifacts on the edges. Figure 5.7(c) shows the result of using the classic kernel regression (2.36) ($N = 2$ and $h = 2.25$). The result of the bilateral kernel regression ($N = 0$, $h_s = 2.25$, and $h_r = 3.0$) is shown in Figure 5.7(d). Figures 5.7(e)-(f) show the results of implementing iterative steering kernel regression ($N = 0$, $h = 0.8$, and no iterations), and ($N = 2$, $h = 1.6$, and 1 iteration), respectively. The RMSE values for images in Figures 5.7(b)-(f) are 9.15, 9.69, 9.72, 8.91, and 8.21, respectively.

5.4 Super-Resolution

The sixth experiment is a multi-frame resolution enhancement (see Figure 2.6) of a real compressed gray-scale video sequence captured with a commercial webcam (3COM, Model no.3718). A total of 53 frames were captured with the camera, where the underlying motion was assumed to follow the translational model, and motions are estimated by the algorithm introduced in Chapter 4. The first frame of the sequence is shown in Figure 5.9(a) We used the spline smoother with $\lambda = 0.01$ to interpolate this image by the resolution enhancement factor of 5 in each direction, as shown in Figure 5.9(b). To produce better estimates, first we fused these frame on a high-resolution grid with 5 times more pixels in each direction (shift-and-add method of Figure 1.2) and then interpolated the missing pixel values. The result of interpolating the shift-and-add image by the Delaunay-spline smoother with $\lambda = 0.01$, and the proposed steering kernel regression method of Section 3.2.2 with the order of 2 and $h = 1.0$, are shown in Figure 5.9(c)-(d), respectively.

The last experiment is a multi-frame super-resolution of a real compressed color

⁵To implement the Delaunay-spline smoother we used MATLAB's "griddata" function with "cubic" parameter to transform the irregularly sampled data set to a dense regularly sampled one (Delaunay triangulation). The quality of the resulting image was further enhanced by applying MATLAB's spline smoother routine "csaps".

image sequence captured with a commercial video surveillance camera; courtesy of Adyoron Intelligent Systems, Ltd., Tel Aviv, Israel. A total of 10 frames were used for this experiment, where the underlying motion was assumed to follow the translational model. One of these frames is shown in Figure 5.10(a). To produce better color estimates, following [50], first we transferred the RGB frames to the **YCrCb** representation, and treated each channel separately, as we did in the third experiment of Section 5.2. We used the method described in Chapter 4 to estimate the motion vectors. Then, we fused each channel of these frames on a high-resolution grid with 5 times more pixels as illustrated in Figure 1.2, interpolated the missing values, and then deblurred the interpolated image using Bilateral Total Variation regularization⁶ [6]. The result of interpolating the irregularly sampled image by the Delaunay-spline smoother (implementation similar to the previous experiment with $\lambda = 0.5$ for the luminance and $\lambda = 1.0$ for the chrominance channels) followed by deblurring is shown in Figure 5.10(b). The results of applying the classic kernel regression ($N = 2$ and $h = 2.0$ for the luminance channel and $h = 3.5$ for the chrominance channels) followed by deblurring and the iterative steering kernel regression ($N = 2$, $h = 4.0$ for the luminance channel and $h = 8.0$ for the chrominance channels, and 1 iteration) followed by deblurring are shown in Figures 5.10(c)-(d), respectively. Comparison of these diverse experiments demonstrate that the proposed iterative steering kernel method not only performs best in a quantitative sense but also results in sharper images with fewer artifacts.

5.5 Conclusion

In this thesis, we studied a non-parametric class of regression methods. We rein-

⁶For this experiment the camera point spread function (PSF) was assumed to be a 5×5 Disk kernel (obtained by the MATLAB command “`fspecial('disk', 2)`”). The deblurring regularization coefficient for the luminance channel was chosen to be 0.2 and for the chrominance channels was chosen to be 0.5.

troduced kernel regression, as a general framework for studying several efficient denoising and interpolation algorithms. We compared the similarities of the classic kernel regression and another popular family of regressors, namely, spline smoother. We showed that the classic kernel regression in essence simplifies to a computationally efficient local linear filtering process, the properties of which were studied under the topic of equivalent kernels.

To overcome the inherent limitations dictated by the linear filtering properties of the classic kernel regression, we introduced the non-linear data-adapted class of kernel regressors. We showed that the popular bilateral filtering technique is a special case of data-adapted kernel regression. Later, we introduced and justified a novel adaptive kernel regression method, called steering kernel regression, with superior performance as compared to other regression method studied in this thesis. Experiments on simulated and real data attested to our claim.

The superior performance of the data-adapted kernel regression can be explained by noting that the spline smoother (2.13) in effect exploit the Tikhonov regularizers. However, the data-adapted kernel regression in its simplest form (bilateral filter) exploits the Total Variation (TV) regularization [51, 52]. The relation between the bilateral filtering and TV regularization is established in [6]. The study in [6] also shows the superior performance of the TV based regularization compared to the Tikhonov based regularization. More details on the adaptive bilateral filters and their relation with the TV regularization can be found in [6].

Finally, in Section 3.3, we proposed an iterative scheme to further improve the performance of data-adapted kernel regression methods. Seeking an automatic method for picking the optimal number of iterations or a stopping criterion for the iterations as well as the optimal regression order is a part of our ongoing work.



Figure 5.1: The performance of different denoising methods are compared in this experiment. The RMSE of the images (b)-(f) are 25, 8.91, 8.65, 6.64, and 6.66, respectively.

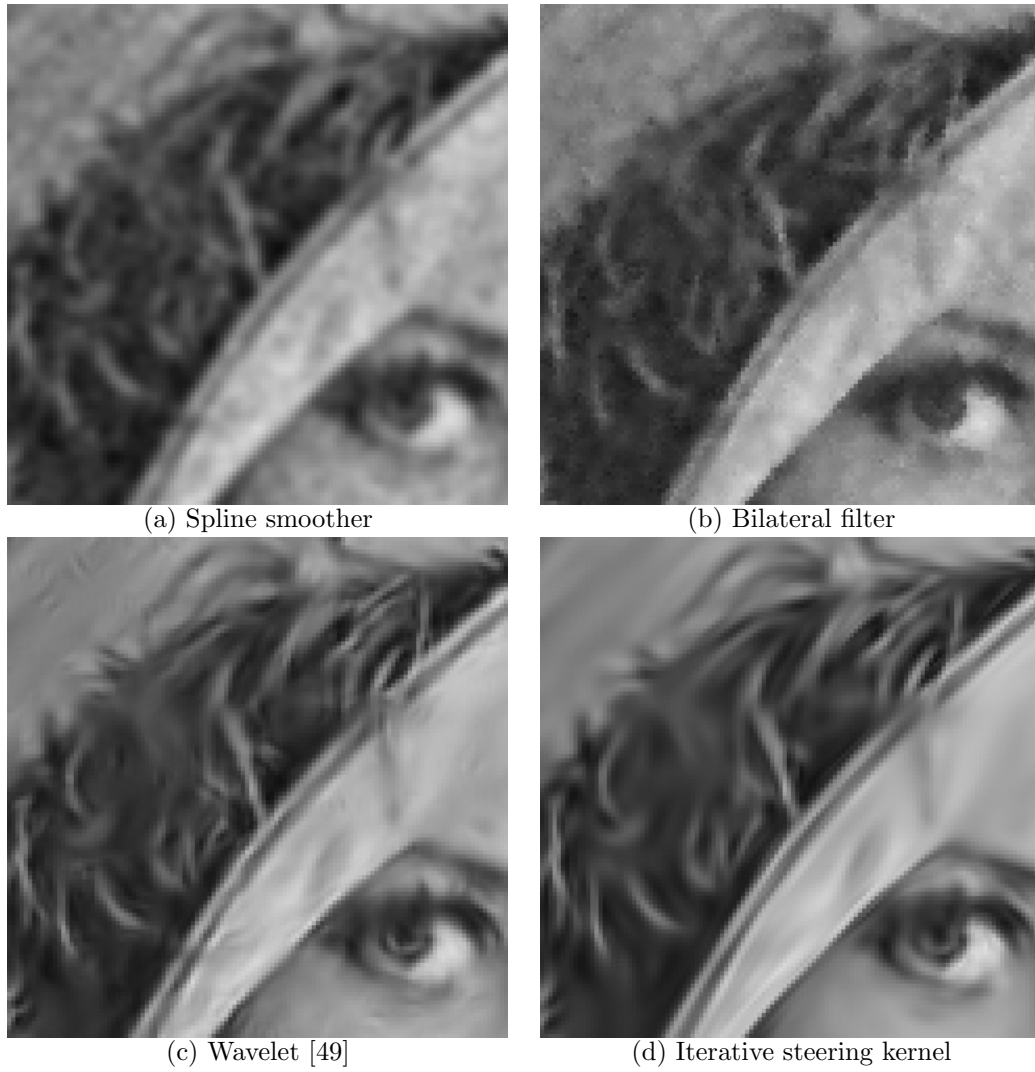


Figure 5.2: Figures 5.1(c)-(f) are enlarged to give (a),(b),(c), and (d), respectively.

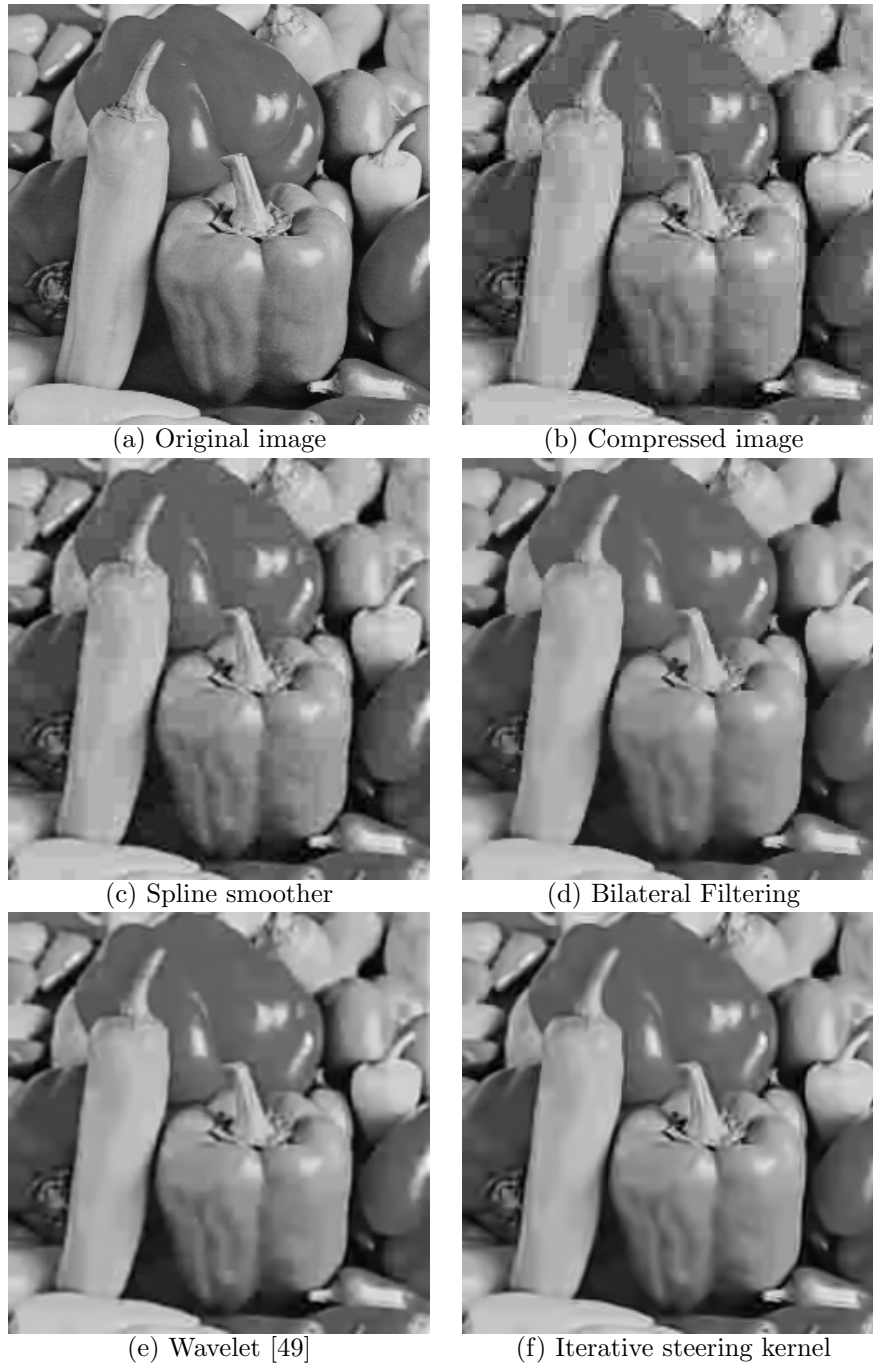


Figure 5.3: The performance of different denoising methods are compared in this experiment on a compressed image by JPEG format with the quality of 10. The RMSE of the images (b)-(f) are 9.76, 9.05, 8.52, 8.80, and 8.48, respectively.

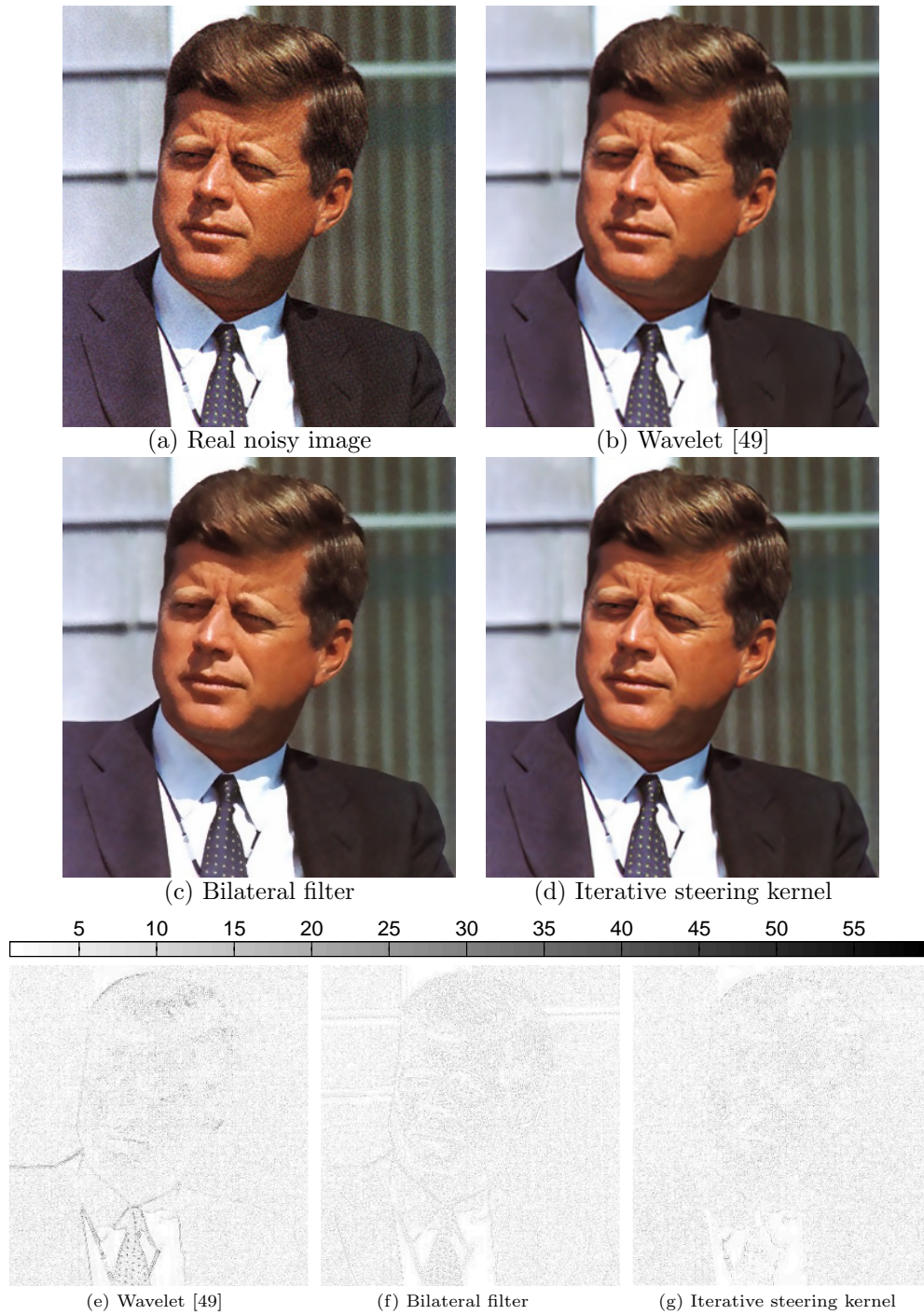


Figure 5.4: The performance of different denoising methods are compared in this experiment on a color image with real noise. Gaussian kernel was used for all experiments.



Figure 5.5: Upscaling experiment. The image of Lena is downsampled by the factor of 3 in (a). The factor of 3 up-sampled images of different methods are shown in (b)-(f). The RMSE values for images (b)-(f) are 7.92, 7.96, 8.07, 7.93, and 7.43 respectively.

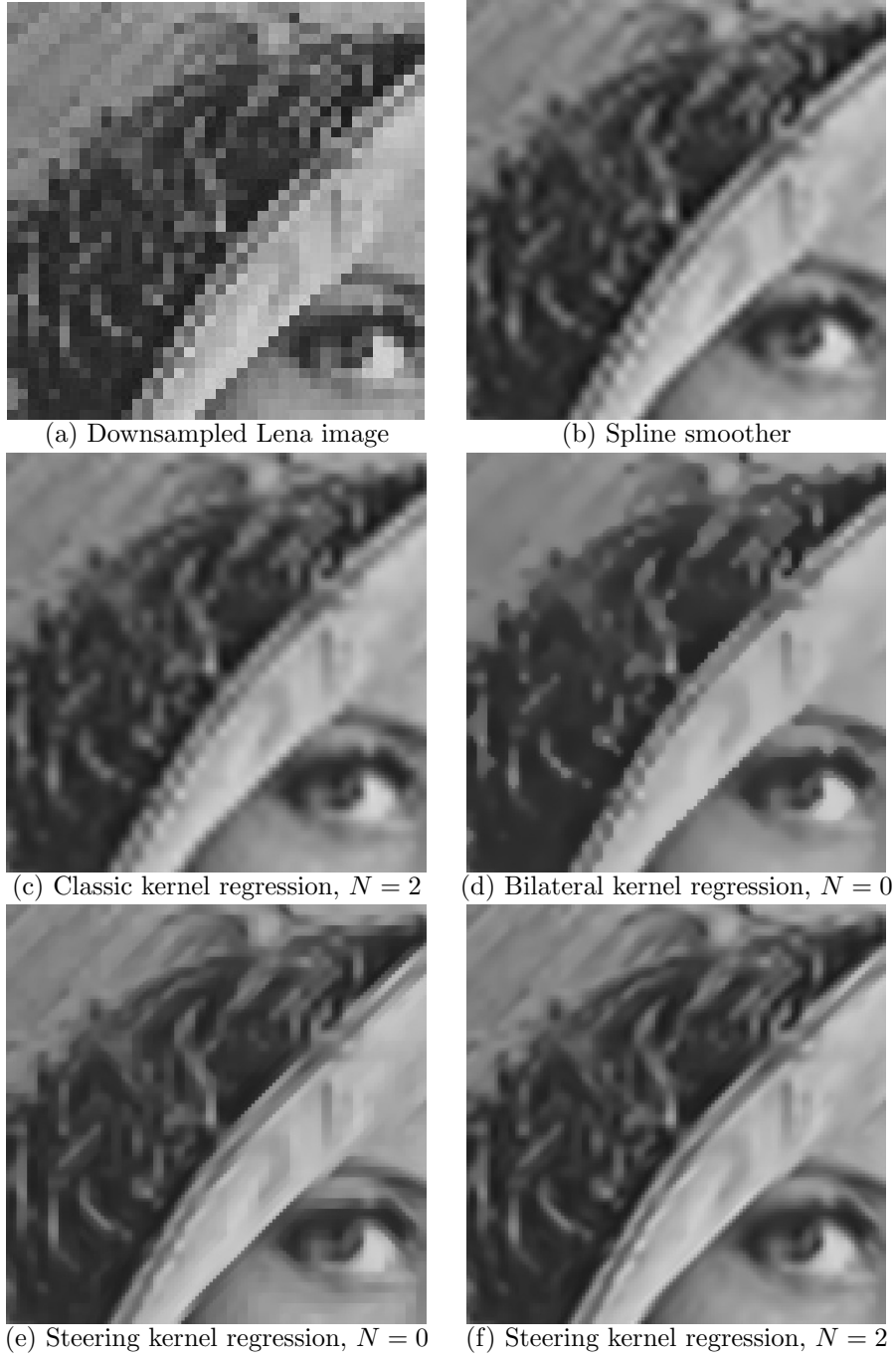


Figure 5.6: Figures 5.5(a)-(f) are enlarged to give (a)-(f), respectively.



Figure 5.7: Irregularly sampled data interpolation experiment, where 85% of the pixels in the Lena image are omitted in (a). The interpolated images using different methods are shown in (b)-(f). RMSE values for (b)-(f) are 9.15, 9.69, 9.72, 8.91, and 8.21, respectively.

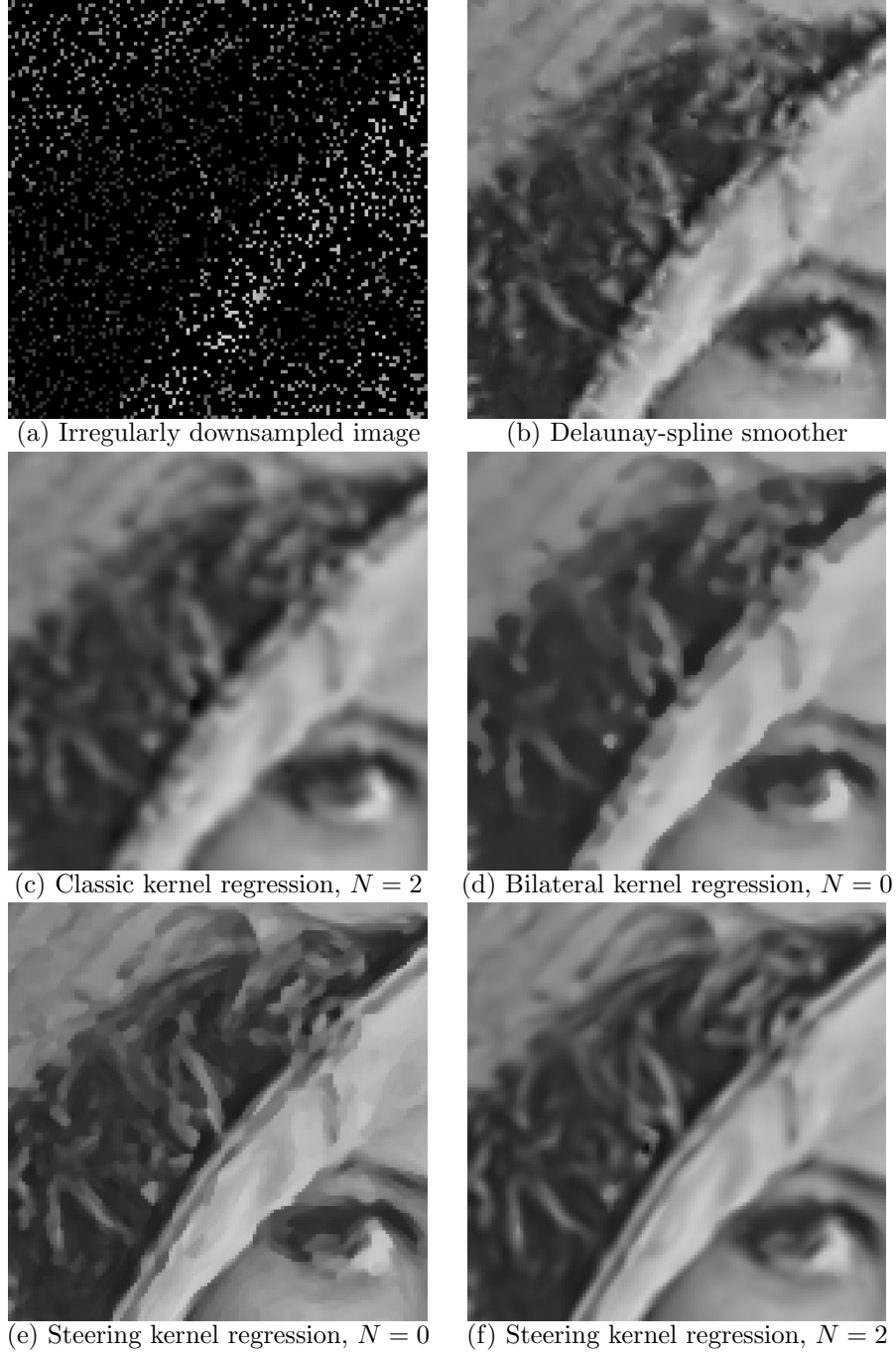


Figure 5.8: Figures 5.7(a)-(f) are enlarged to give (a)-(f), respectively.



Figure 5.9: Image fusion (Super-Resolution) experiment of a real data set consisting of 10 compressed grayscale images. One input image is shown in (a) which is up-scaled in (b) by the spline smoother interpolation. (c)-(d) show the multi-frame Shift-And-Add images after interpolation by the Delaunay-spline smoother and the steering kernel methods. The resolution enhancement factor in this experiment was 5 in each direction.



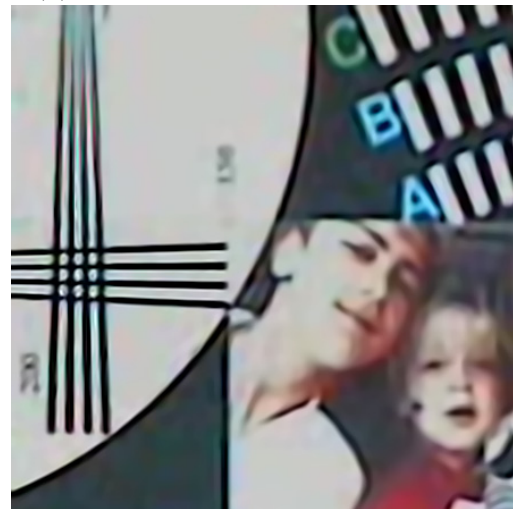
(a) The first input frame



(b) Multi-frame Delaunay-spline smoother



(c) Multi-frame classic kernel regression



(d) Multi-frame steering kernel regression

Figure 5.10: Image fusion (Super-Resolution) experiment of a real data set consisting of 10 compressed color frames. One input image is shown in (a). (b)-(d) show the multi-frame Shift-And-Add images after interpolating by the Delaunay-spline smoother, classical kernel, and steering kernel regression methods, respectively. The resolution enhancement factor in this experiment was 5 in each direction.

Chapter 6

Super Resolution Toolbox

6.1 Introduction

This chapter explains the usage of the super resolution toolbox, which is the implementation of the kernel regression technique described in this thesis. As we have seen in Chapter 5, the technique can be applied for a wide class problems. Here, we explain functions, which deal with denoising, interpolation, and fusion. Note that the function will properly operate on MATLAB (version 6.5).

6.2 Installation

1. Extract the archive file “SuperResolutionToolBox.zip”, and copy the folder “SuperResolutionToolBox” to a folder (e.g. “C:/MATLAB6p5/work/”).
2. Start MATLAB, and set the path to the folder of “SuperResolutionToolBox” with subfolders. As shown in Figure 6.1, first, pull down the file menu and click the “Set Path...” illustrated in Figure 6.1(a). Second, following the circled number, set the

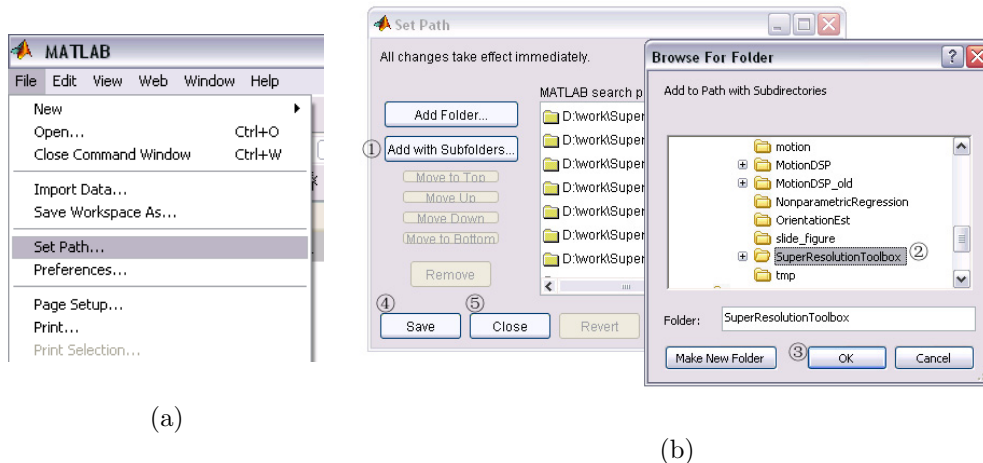


Figure 6.1: Setting path.

path as illustrated in Figure 6.1(b).

6.3 The Kernel Regression Function

This section explains the function “KernelReg”. In the command line of MATLAB, we run the function as follows:

```
[z, zx, zy] = KernelReg(frames, r, mvs, ref, Q, h, ktype, kfunc, ksize, it, wsize);
```

where **z**, **zx**, and **zy** are the output values: estimated images, estimated vertical gradient images, and estimated horizontal gradient images, respectively. Table 6.1 explains the parameters of the function. With this function, we can do denoising, interpolation, and fusion. If the **frames** contain the color data in RGB, we must use the “KernelReg_color” function instead of calling the “KernelReg” function. Example usages are introduced in the next section.

Params	Descriptions	Dimensions
frames	Input frames (low resolution and noisy images)	$L \times M \times N$
r	Resolution enhancement factor	scalar
mvs	Motion vectors (translational) Please set $\mathbf{mvs} = [0, 0]^T$, when the number of frames is 1.	$2 \times (N - 1)$
ref	The reference frame number	scalar
Q	Regression order: 0 = constant, 1 = linear, or 2 = quadratic	scalar
h	Global smoothing parameter Classic kernel case, h Bilateral kernel case, $h = [h_s, h_r]^T$ Steering kernel case, h	scalar 2×1 scalar
ktype	Kernel type: 'ga' = Gaussian, or 'exp' = exponential (Laplacian)	string
kfunc	Kernel function: 'classic', 'bilateral', or 'steering'	string
ksize	Kernel window size (The window will be $\mathbf{ksize} \times \mathbf{ksize}$.)	scalar
it	The number of iteration for iterative steering kernel regression	scalar
wsize	The size of image analysis window for steering kernel regression	scalar

Table 6.1: The parameter descriptions of “KernelReg” function.

6.4 Examples

There are several sample codes using the “KernelReg” function, which are located in the folder named “examples”, under the folder of “SuperResolutionToolBox”. The codes demonstrate the function with practical image processing examples. The details of the example codes are written in the m-files, which are listed below.

- **Gaussian noise removal** (“Lena_denoise.m”)

This example demonstrates Gaussian noise removal with the kernel regression techniques discussed in this thesis: classic, bilateral and iterative steering kernel regression.

This produces the denoising results in Figure 5.1

- **Compression artifact reduction** (“Pepper_deblock.m”)

This example demonstrates the compression artifact reduction. This program reads an image and adds compression artifacts by saving the image in the JPEG format, and reduces the artifacts using kernel regression. This produces the deblocking results

in Figure 5.3

- **Film grain removal** (“JFK_denoise.m”)

This example demonstrates the denoising effect on a real noisy image (film grain noise).

Besides, the image is a color image so that this tells how to use the “KernelReg_color” function. This produces the denoising results shown in Figure 5.4

- **Image upscale** (“Lena_upscale.m”)

This example demonstrates the image upscale on the Lena image in Figure 5.1(a).

The program first downsamples the Lena image with a downsampling factor, and then upscales the given image with the same factor. This produces the upscaling results shown in Figure 5.5.

- **Image fusion** (“tank8_fusion.m”)

This example demonstrates the simple image fusion and super-resolution on the tank sequence in Figure 1.4. This produces the image fusion results shown in Figure 2.7.

- **Color super-resolution** (“ady10_superresolution.m”)

This example demonstrates color super-resolution on a real noisy and severely compressed video sequence. This produces the color super-resolution results shown in Figure 5.10.

6.5 Troubleshooting

In the interpolation case, a reconstructed image with the function might have some missing pixels. The problem can be solved by choosing appropriate parameter values. Typically, the problem is caused by wrong choices of the resolution enhancement factor and

the global smoothing parameter. Either a smaller resolution enhancement factor or a larger global smoothing parameter can overcome the trouble.

6.6 Summary

This chapter explained how to use the “KernelReg” function, and it is a convenient tool for image processing and reconstruction. Only one function can do many things: denoising, deblocking, upscaling, super-resolution, and so on.

Chapter 7

Future Work

7.1 Robust Kernel Regression

The classic kernel regression framework can be regarded as a weighted least square estimator (q.v. Chapter 2). However, in the case that there are some outliers in a measured data set, the estimator will strongly stick to those outliers due to the square error norm. In order to overcome this problem, it is possible for us to modify the framework with the idea of robust estimation. A more general, the robust framework for kernel regression may be expressed as

$$\min_{\{\beta_n\}_{n=0}^N} \sum_{i=1}^P \Omega \left(y_i - \beta_0 - \beta_1^T (\mathbf{x}_i - \mathbf{x}) - \beta_2^T \text{vech} \left\{ (\mathbf{x}_i - \mathbf{x})(\mathbf{x}_i - \mathbf{x})^T \right\} \right) \mathcal{K}(\mathbf{x}_i - \mathbf{x}, y_i - y), \quad (7.1)$$

where $\Omega(\cdot)$ is the *error norm function*. The common selections of the function are illustrated in Table 7.1. As an example of the usefulness of this more general framework, salt & pepper noise reduction is illustrated in Figure 7.1. In this example, we added 20% salt and pepper noise (outliers) to the original image of Figure 7.1(a), resulting in the noisy image of Figure 7.1(b). The denoised image using a 3×3 median filter, wavelet method of [49], l_2 classic

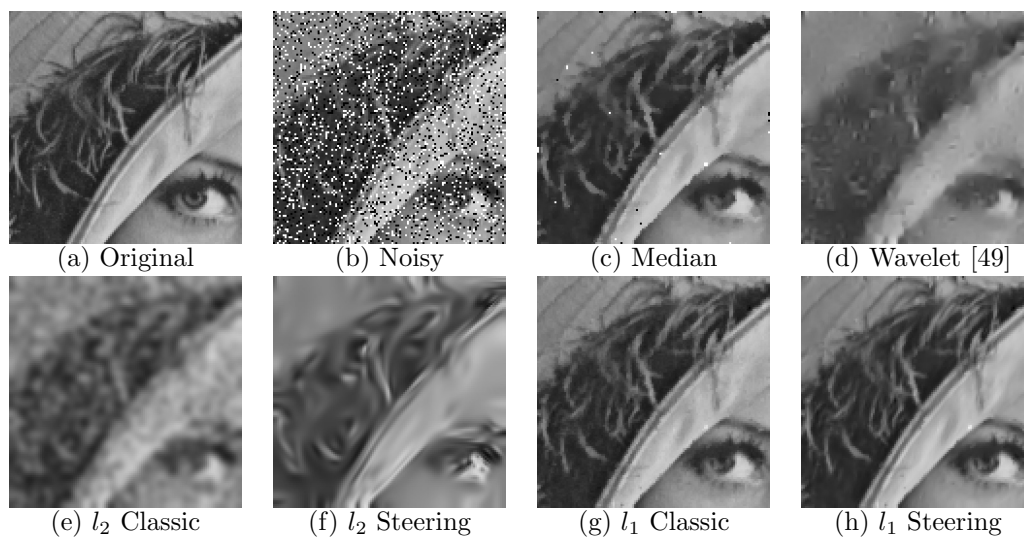


Figure 7.1: An example of the salt & pepper noise reduction. Corresponding RMSE for (b)-(h) are 63.84, 11.05, 22.47, 21.81, 21.06, 7.65, and 7.14.

kernel regression ($N = 2$ and $h = 2.46$), l_2 iterative steering kernel regression ($N = 2$, $h = 2.25$ and 20 iterations), l_1 classic kernel regression ($N = 2$ and $h = 0.65$), and l_1 iterative steering kernel regression ($N = 2$, $h = 2.25$, and no iterations) are shown in Figures 7.1(b)-(h), respectively. The performance difference is quite clear. By using the l_1 norm instead of the l_2 norm, the kernel regression now successfully reduced the salt & pepper noise. Besides, with the steering kernel, we have an even better estimated image.

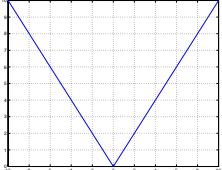
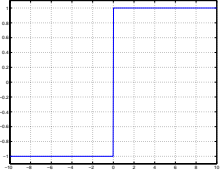
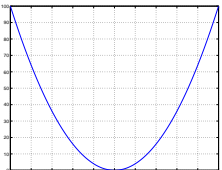
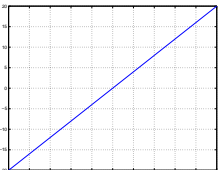
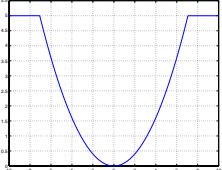
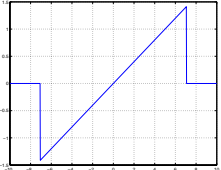
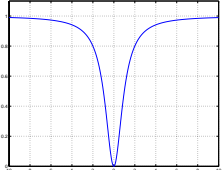
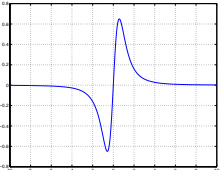

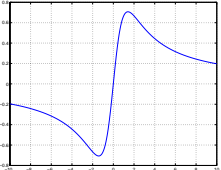
Absolute (l_1 Norm)	
$\Omega(x) = x $ 	$\Omega'(x) = \text{sign}(x)$ 
Quadratic (l_2 Norm)	
$\Omega(x) = x^2$ 	$\Omega'(x) = 2x$ 
Truncated Quadratic	
$\Omega(x, \alpha, \lambda) = \begin{cases} \lambda x^2 & x < \sqrt{\frac{\alpha}{\lambda}} \\ \alpha & \text{else} \end{cases}$ 	$\Omega'(x, \alpha, \lambda) = \begin{cases} 2\lambda x & x < \sqrt{\frac{\alpha}{\lambda}} \\ 0 & \text{else} \end{cases}$ 
Geman & McClure	
$\Omega(x, \alpha) = \frac{x^2}{x^2 + \alpha}$ 	$\Omega'(x, \alpha) = \frac{2x\alpha}{(x^2 + \alpha)^2}$ 
Lorentzian	
$\Omega(x, \alpha) = \log \left\{ 1 + \frac{1}{2} \left(\frac{x}{\alpha} \right)^2 \right\}$ 	$\Omega'(x, \alpha) = \frac{2x}{x^2 + 2\alpha^2}$ 

Table 7.1: Error norm functions and their derivatives [1].

7.2 Segment Motion Estimation

7.2.1 Motivation

Motion estimation enables us to fuse images so that we can reconstruct a high resolution image by using the kernel regression technique. However the larger the images to fuse, the more difficult to estimate motions with a simple motion model. In this thesis, we dealt with the simplest motion model, translational motion. It is obviously impossible for this model to be assumed always valid. Even using the parametric (e.g. affine motion model), camera lens distortion on the images depart from this simple model. Moreover, it is definitely necessary for us to consider the motion flow occlusions. In this section, an idea of the motion estimation for large images which may have occlusions will be discussed.

7.2.2 Image Segmentation

Since the motion estimation on large images is difficult, the intuitive way to overcome this difficulty is to segment the images into small pieces, and then estimate motions for each piece. There are several types of segmentation methods we must consider. The list below is a sampling of these methods.

1. **Fixed block base**

This is the simplest segmentation method. With this method, we blindly segment two images (reference and target images) into a collection of fixed-size blocks in the same way, and estimate motions between every pair of corresponding blocks of the reference image and the target image. Theoretically, the smaller the block size, the more accurate the overall motion will be estimated; however, the local estimation becomes more difficult and unstable.

2. Object or texture base

Motion flow occlusions often happen around the border areas of objects or textures. Hence it is a good way for us to segment the images based on objects or textures, and estimate the corresponding segments between the reference and the target image.

3. Motion base

The motion flow occlusions do not happen at all the objects' borders. As we know already, the larger the segment, the more stable the motion estimate will be. The motion based segmentation method detects the occlusions and segment the image accordingly. Although this is the most difficult method, once we implement and have the motions, the reconstructed images will give superior results.

7.2.3 Motion Models

Motion models are also significantly important for successful motion estimation. Since the translational model is often not flexible enough to fit unknown motions, with this model, the only thing we can do to have a better parametric fit is to reduce the size of the segment. However, again, the estimation becomes unstable due to the small number of optical flow equations. Another way to proceed is to use more general parametric motion models: affine, projective linear, and so on. Most likely, with a proper image segmentation algorithm, the affine motion model is the most appropriate one. In the next section, one simple demonstration is shown.

7.3 Example

In this section, we present a simple example of the image reconstruction from large size frames. Figure 7.2 shows the three frames from a video sequence. The size of all the frames is 350×600 . Using the classic kernel regression (order $N = 2$, global smoothing parameter $h = 1.0$, and resolution enhancement factor $r = 2$), we try to reconstruct a high quality image from them. First, we reconstruct an image under the assumption that all the pixels have the same linear motion (i.e. translational motion model). The result is given in Figure 7.3. Since the global motion model is inaccurate, the upper and bottom part of the reconstruction look blurry. Alternatively, we segment all the frames into fixed-size blocks (50×50) and estimate motions for these blocks. The result is illustrated in Figure 7.4. While this result too is not perfect, the quality is much better (sharper) than Figure 7.3.

7.4 Summary

This chapter showed another possibility of the kernel regression technique. In the future, it is obvious that video to video super-resolution and dynamic super-resolution will be focused.



(a) The first frame



(b) The second frame



(c) The thrid frame

Figure 7.2: Three large frames from a video sequence. The size of each frame is 350×600 .

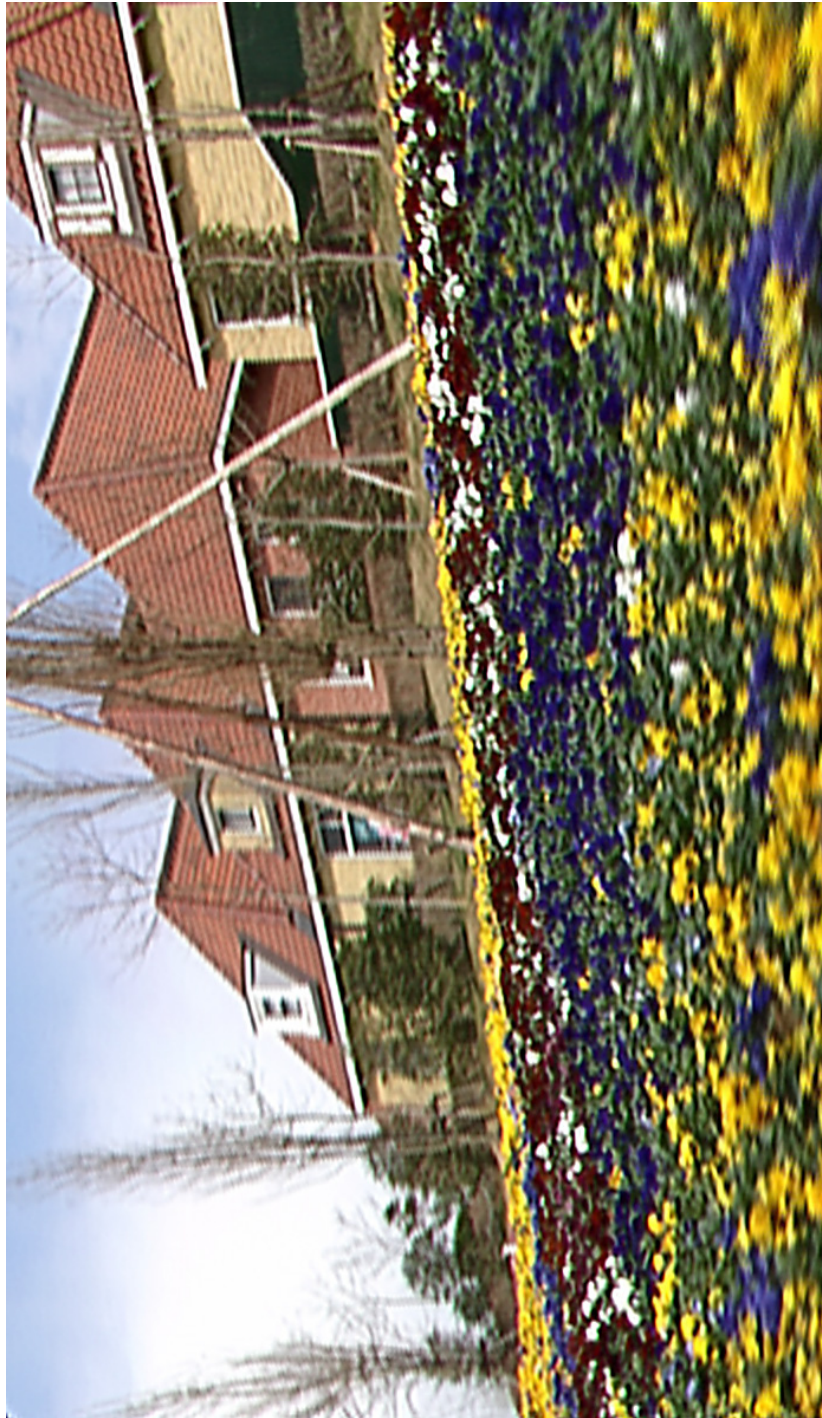


Figure 7.3: The reconstructed image using the translational motion model.

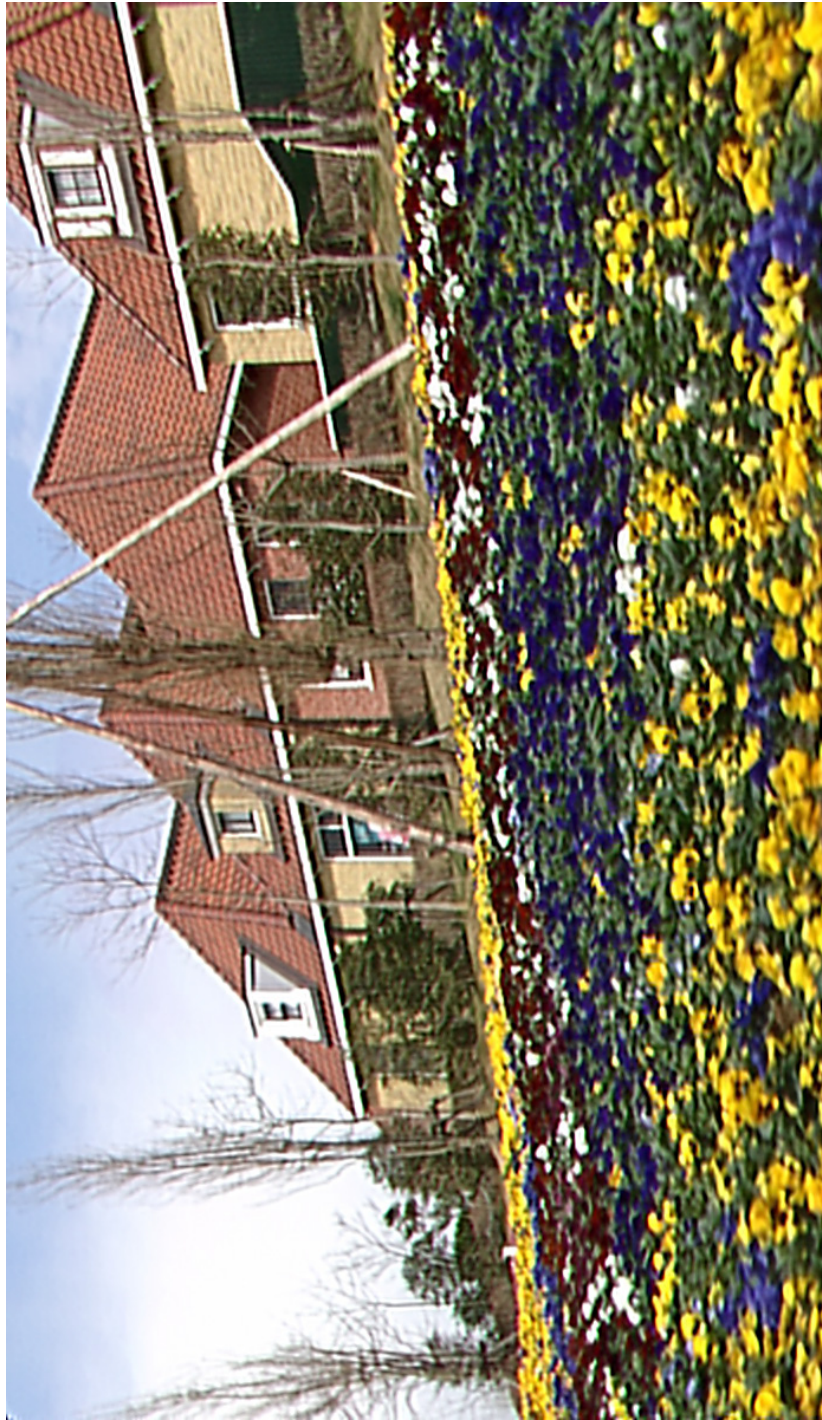


Figure 7.4: The reconstructed image using the translational motion model with the block segmentation.

Appendix A

Image Deblurring

Image deblurring is the last phase of super-resolution, and it is necessary to recover some high frequency components of fused images in most cases, since the images are usually blurred by atmosphere and camera. Moreover, unfortunately, kernel regression¹ also gives some blurring effects to the images, particularly when we choose a wrong parameter (e.g. unnecessarily large smoothness). Therefore image deblurring is necessary, and, in this section, a simple deblurring method in the spatial domain is introduced. We leave the method to remove spatial invariant blurring effects by adapted kernel regression as a future work.

Suppose we have a blurred image $\underline{\mathbf{Z}}$, which is given by a blurred version of a real scene \mathbf{X} , is expressed as

$$\underline{\mathbf{Z}} = \underline{\mathbf{B}}\mathbf{X} + \underline{\boldsymbol{\varepsilon}}, \quad (\text{A.1})$$

where the matrix (image) with an underline is the column-stack vector of the matrix, \mathbf{B} is the blur operator, and $\boldsymbol{\varepsilon}$ is noise. Note that the estimated blurred image by kernel regression has already removed much of the noise. Regularized least-squares estimator is a

¹Data-adapted kernel regression will give spatially variant blurring effects to estimated images

	Tikhonov	Total variation	Bilateral total variation [6]
$\Upsilon(\underline{\mathbf{X}})$	$\ \Gamma\underline{\mathbf{X}}\ _2^2$	$\ \Gamma\underline{\mathbf{X}}\ _1$	$\sum_{l=-q}^q \sum_{m=-q}^q \alpha^{ l + m } \ \underline{\mathbf{X}} - \mathbf{S}_{x_1}^l \mathbf{S}_{x_2}^m \underline{\mathbf{X}}\ _1$
$\Upsilon'(\underline{\mathbf{X}})$	$2\Gamma^T \Gamma \underline{\mathbf{X}}$	$\Gamma^T \text{sign}(\Gamma \underline{\mathbf{X}})$	$\sum_{l=-q}^q \sum_{m=-q}^q \alpha^{ l + m } (\mathbf{I} - \mathbf{S}_{x_1}^{-l} \mathbf{S}_{x_2}^{-m}) \text{sign}(\underline{\mathbf{X}} - \mathbf{S}_{x_1}^l \mathbf{S}_{x_2}^m \underline{\mathbf{X}})$

Table A.1: Regularization functions and their first derivatives.

typical choice for the real scene \mathbf{X} , which takes the form

$$\hat{\underline{\mathbf{X}}}_{\text{RLS}} = \arg \min_{\underline{\mathbf{X}}} \left[\|\mathbf{B}\underline{\mathbf{X}} - \underline{\mathbf{Z}}\|_2^2 + \lambda \Upsilon(\underline{\mathbf{X}}) \right] = \arg \min_{\underline{\mathbf{X}}} C(\underline{\mathbf{X}}), \quad \lambda \geq 0, \quad (\text{A.2})$$

where $\Upsilon(\underline{\mathbf{X}})$ is a regularization function. We minimize the cost function $C(\underline{\mathbf{X}})$ to find $\underline{\mathbf{X}}$ by the steepest descent method,

$$\hat{\underline{\mathbf{X}}}^{(n+1)} = \hat{\underline{\mathbf{X}}}^{(n)} - \mu \left[\mathbf{B}^T (\mathbf{B}\hat{\underline{\mathbf{X}}}^{(n)} - \underline{\mathbf{Z}}) + \lambda \Upsilon'(\hat{\underline{\mathbf{X}}}^{(n)}) \right]. \quad (\text{A.3})$$

The choices of $\Upsilon(\underline{\mathbf{X}})$ and their derivatives are listed up in Table A.1, in which Γ is a highpass filter, (e.g. Laplacian), and \mathbf{S} is the shift operator, and α is a parameter controlling the decay of weights.

Appendix B

Local Gradient Estimation

As we mentioned several times, the higher order ($N > 0$) kernel regression used for gradient estimation, which is very useful for image processing and reconstruction. As we know already, gradient estimates can be used for orientation estimation and motion estimation. In this section, local gradient estimators with the order of $N = 1$ and 2 are derived. In the optimization problem (2.24), the term we wish to estimate is β_1 . Hence, the gradient estimator is

$$\nabla \hat{z}(\mathbf{x}) = \hat{\beta}_1 = \begin{bmatrix} \mathbf{e}_2^T \\ \mathbf{e}_3^T \end{bmatrix} (\mathbf{X}_x^T \mathbf{W}_x \mathbf{X}_x)^{-1} \mathbf{X}_x^T \mathbf{W}_x \mathbf{Y}, \quad (\text{B.1})$$

where \mathbf{e}_2 and \mathbf{e}_3 are column vectors (the same size of \mathbf{b} in (2.25)) whose second and third elements are 1 respectively, and the rest are zero. Following the notation of (2.29), the local linear ($N = 1$) and local quadratic ($N = 2$) gradient estimators are given by

$$\nabla \hat{z}(\mathbf{x}) = \sum_{i=1}^P [\mathbf{s}_{22} - \mathbf{s}_{21} \mathbf{s}_{11}^{-1} \mathbf{s}_{12}]^{-1} [-\mathbf{s}_{21} \mathbf{s}_{11}^{-1} + (\mathbf{x}_i - \mathbf{x})] K_{\mathbf{H}}(\mathbf{x}_i - \mathbf{x}) y_i \quad (\text{B.2})$$

$$\nabla \hat{z}(\mathbf{x}) = \sum_{i=1}^P \mathbf{S}^{-1} [-\mathbf{S}_{21} \mathbf{S}_{11}^{-1} + (\mathbf{x}_i - \mathbf{x}) - \mathbf{S}_{23} \mathbf{S}_{33}^{-1} \text{vech} \{(\mathbf{x}_i - \mathbf{x})(\mathbf{x}_i - \mathbf{x})^T\}] K_{\mathbf{H}}(\mathbf{x}_i - \mathbf{x}) y_i, \quad (\text{B.3})$$

respectively, where

$$\begin{aligned} \mathbf{S}_{11} &= \mathbf{s}_{11} - \mathbf{s}_{13}\mathbf{s}_{33}^{-1}\mathbf{s}_{31}, & \mathbf{S}_{21} &= \mathbf{s}_{21} - \mathbf{s}_{23}\mathbf{s}_{33}^{-1}\mathbf{s}_{31} \\ \mathbf{S}_{23} &= \mathbf{s}_{23} - \mathbf{s}_{21}\mathbf{s}_{11}^{-1}\mathbf{s}_{13}, & \mathbf{S}_{33} &= \mathbf{s}_{33} - \mathbf{s}_{31}\mathbf{s}_{11}^{-1}\mathbf{s}_{13}, \end{aligned} \quad (\text{B.4})$$

$$\mathbf{S} = \mathbf{s}_{22} - \mathbf{S}_{21}\mathbf{S}_{11}^{-1}\mathbf{s}_{12} - \mathbf{S}_{23}\mathbf{S}_{33}^{-1}\mathbf{s}_{32}. \quad (\text{B.5})$$

Of course it is absolutely possible for us to use adapted kernels (bilateral and steering kernels) for the gradient estimators as well. Amazingly, this estimator also has great denoising effect and can interpolate gradient images, consequently image warping is also possible with it, therefore it is a suitable tool for motion estimation, too. For the super-resolution experiments in Chapter 5, these estimators are used for motion estimation.

Bibliography

- [1] M. J. Black and P. Anandan, “The robust estimation of multiple motions: Parametric and piecewise-smooth flow fields,” *Computer Vision and Image Understanding*, vol. 63, no. 1, pp. 75–104, January 1996.
- [2] H. Takeda, S. Farsiu, and P. Milanfar, “Image denoising by adaptive kernel regression,” *Proceedings of the 39th Asilomar Conference on Signals, Systems, and Computers, Pacific Grove, CA*, pp. 1660–1665, November 2005.
- [3] —, “Kernel regression for image processing and reconstruction,” submitted to *IEEE Transactions on Image Processing*.
- [4] —, “Robust kernel regression for restoration and reconstruction of images from sparse noisy data,” *Invited paper, 2006 International Conference on Image Processing, Atlanta, GA*.
- [5] T. F. Chan, “Nontexture inpainting by curvature-driven diffusions,” *Journal of Visual Communication and Image Representation*, vol. 12, no. 10, pp. 436–449, May 2001.
- [6] S. Farsiu, D. Robinson, M. Elad, and P. Milanfar, “Fast and robust multi-frame super-resolution,” *IEEE Transactions on Image Processing*, vol. 13, no. 10, pp. 1327–1344, October 2004.

- [7] C. Stiller and J. Konrad, “Estimating motion in image sequences - a tutorial on modeling and computation of 2d motion,” *IEEE Signal Processing Magazine*, vol. 16, no. 4, pp. 70–91, July 1999.
- [8] J. R. Bergen, P. Anandan, K. J. Hanna, and R. Hingorani, “Hierarchical model-based motion estimation,” *Proceedings of the European Conf. on Computer Vision*, pp. 237–252, May 1992.
- [9] S. Farsiu, M. D. Robinson, M. Elad, and P. Milanfar, “Robust shift-and-add approach to super-resolution,” *Proceeding of the SPIE Annual Meeting, San Diego, CA*, vol. 5203, August 2003.
- [10] R. C. Gonzalez and R. E. Woods, *Digital Image Processing*. Upper Saddle River, N.J.: Prentice Hall, 2002.
- [11] M. Unser, “Splines: A perfect fit for signal and image processing,” *IEEE Signal Processing Magazine*, vol. 16, no. 6, pp. 22–38, November 1999.
- [12] C. de Boor, *A Practical Guide to Splines*. New York: Springer-Verlag, 1978.
- [13] E. A. Nadaraya, “On estimating regression,” *Theory of Probability and its Applications*, vol. 9, pp. 141–142, September 1964.
- [14] M. Elad and Y. Hel-Or, “A fast super-resolution reconstruction algorithm for pure translational motion and common space-invariant blur,” *IEEE Transactions on Image Processing*, vol. 10, no. 8, pp. 1187–1193, August 2001.
- [15] A. Zomet, A. Rav-Acha, and S. Peleg, “Robust super-resolution,” *Proceedings of the International Conference on Computer Vision and Pattern Recognition (CVPR)*, 2001, Hawaii.

- [16] S. M. Kay, *Fundamentals of Statistical Signal Processing - Estimation Theory* -, ser. Signal Processing Series. Englewood Cliffs, N.J.: PTR Prentice-Hall, 1993.
- [17] M. P. Wand and M. C. Jones, *Kernel Smoothing*, ser. Monographs on Statistics and Applied Probability. London; New York: Chapman and Hall, 1995.
- [18] S. V. Huffel and J. Vandewalle, *The Total Least Squares Problem: Computational Aspects and Analysis*, ser. Frontiers in applied mathematics. Philadelphia: Society for Industrial and Applied Mathematics, 1991, vol. 9.
- [19] P. Yee and S. Haykin, "Pattern classification as an ill-posed, inverse problem: a regularization approach," *Proceeding of the IEEE International Conference on Acoustics, Speech, and Signal Processing, ICASSP*, vol. 1, pp. 597–600, April 1993.
- [20] V. N. Vapnik, *Statistical Learning Theory*, ser. Adaptive and learning systems for signal processing, communications, and control. New York: Wiley, 1998.
- [21] H. Knutsson and C.-F. Westin, "Normalized and differential convolution: Methods for interpolation and filtering of incomplete and uncertain data," *Proceedings of IEEE Computer Society Conference on Computer Vision and Pattern Recognition*, pp. 515–523, June 16-19 1993.
- [22] T. Q. Pham, L. J. van Vliet, and K. Schutte, "Robust fusion of irregularly sampled data using adaptive normalized convolution," *EURASIP Journal on Applied Signal Processing*, 2005.
- [23] C. Tomasi and R. Manduchi, "Bilateral filtering for gray and color images," *Proceeding of the 1998 IEEE International Conference of Compute Vision, Bombay, India*, pp. 836–846, January 1998.

- [24] M. Elad, “On the origin of the bilateral filter and ways to improve it,” *IEEE Transactions on Image Processing*, vol. 11, no. 10, pp. 1141–1150, October 2002.
- [25] D. Comaniciu and P. Meer, “Mean shift: A robust approach toward feature space analysis,” *IEEE Transactions on Pattern Analysis and Machine Intelligence*, vol. 24, no. 5, pp. 603–619, May 2002.
- [26] X. Li and M. T. Orchard, “New edge-directed interpolation,” *IEEE Transactions on Image Processing*, vol. 10, no. 10, pp. 1521–1527, October 2001.
- [27] N. K. Bose and N. Ahuja, “Superresolution and noise filtering using moving least squares,” submitted to *IEEE Transactions on Image Processing*, 2005.
- [28] B. W. Silverman, *Density Estimation for Statistics and Data Analysis*, ser. Monographs on Statistics and Applied Probability. London; New York: Chapman and Hall, 1986.
- [29] W. Hardle, *Applied Nonparametric Regression*. Cambridge [England] ; New York: Cambridge University Press, 1990.
- [30] W. Hardle, M. Muller, S. Sperlich, and A. Werwatz, *Nonparametric and Semiparametric Models*, ser. Springer Series in Statistics. Berlin ; New York: Springer, 2004.
- [31] W. Hardle, *Smoothing Technique with Implementation in S*, ser. Springer Series in Statistics. New York: Springer-Verlag, 1991.
- [32] D. Ruppert and M. P. Wand, “Multivariate locally weighted least squares regression,” *The Annals of Statistics*, vol. 22, no. 3, pp. 1346–1370, September 1994.
- [33] M. G. Schimek, *Smoothing and Regression -Approaches, Computation, and Application-*, ser. Wiley Series in Probability and Statistics. New York: Wiley-Interscience, 2000.

- [34] J. E. Gentle, W. Hardle, and Y. Mori, *Handbook of Computational Statistics: Concepts and Methods*. Berlin ; New York: Springer, 2004, pp. 539–564 (Smoothing: Local Regression Techniques).
- [35] R. L. Eubank, *Nonparametric Regression and Spline Smoothing*, ser. Statistics, textbooks and monographs. New York: Marcel Dekker, 1999, vol. 157.
- [36] L. Piegl and W. Tiller, *The NURBS Book*. New York: Springer, 1995.
- [37] M. Arigovindan, M. Suhling, P. Hunziker, and M. Unser, “Variational image reconstruction from arbitrarily spaced samples: A fast multiresolution spline solution,” *IEEE Transactions on Image Processing*, vol. 14, no. 4, pp. 450–460, April 2005.
- [38] B. W. Silverman, “Spline smoothing: The equivalent variable kernel method,” *The Annals of Statistics*, vol. 12, no. 3, pp. 898–916, September 1984.
- [39] J. A. Nelder and R. Mead, “A simplex method for function minimization,” *Computer Journal*, vol. 7, no. 4, pp. 308–313, 1965.
- [40] I. S. Abramson, “On bandwidth variation in kernel estimates - a square root law,” *The Annals of Statistics*, vol. 10, no. 4, pp. 1217–1223, December 1982.
- [41] A. Buades, B. Coll, and J. M. Morel, “On image denoising methods,” *Technical Note, CMLA (Centre de Mathematiques et de Leurs Applications)*, no. 5, 2004.
- [42] K. Fukunaga, *Introduction to Statistical Pattern Recognition*, 2nd ed., ser. Computer Science and Scientific Computing. Boston: Academic Press, 1990.
- [43] R. O. Duda, P. E. Hart, and D. G. Stork, *Pattern Classification*, 2nd ed. New York: Wiley-Interscience, 2001.

- [44] X. Feng and P. Milanfar, "Multiscale principal components analysis for image local orientation estimation," *Proceedings of the 36th Asilomar Conference on Signals, Systems and Computers, Pacific Grove, CA*, November 2002.
- [45] K. V. Mardia, J. T. Kent, and J. M. Bibby, *Multivariate Analysis*. London ; New York: Academic Press, 1979.
- [46] A. Edelman, "Eigenvalues and condition numbers of random matrices," *SIAM Journal on Matrix Analysis and Applications*, vol. 9, pp. 543–560, 1988.
- [47] S. Ando, "Consistent gradient operators," *IEEE Transactions on Pattern Analysis and Machine Intelligence*, vol. 22, no. 3, pp. 252–265, March 2000.
- [48] Y. Wang, J. Ostermann, and Y. Zhang, *Video Processing and Communications*. Upper Saddle River, NJ: Prentice Hall, 2002.
- [49] J. Portilla, V. Strela, M. Wainwright, and E. P. Simoncelli, "Image denoising using scale mixtures of Gaussians in the wavelet domain," *IEEE Transactions on Image Processing*, vol. 12, no. 11, pp. 1338–1351, November 2003.
- [50] S. Farsiu, M. Elad, and P. Milanfar, "Multiframe demosaicing and super-resolution of color images," *IEEE Transactions on Image Processing*, vol. 15, no. 1, pp. 141–159, January 2006.
- [51] L. Rudin, S. Osher, and E. Fatemi, "Nonlinear total variation based noise removal algorithms," *Physica D*, vol. 60, pp. 259–268, November 1992.
- [52] T. F. Chan, S. Osher, and J. Shen, "The digital TV filter and nonlinear denoising," *IEEE Transactions on Image Processing*, vol. 10, no. 2, pp. 231–241, February 2001.